

January 2012

# A Novel Ultrasonic Method to Quantify Bolt Tension

Jairo Andres Martinez Garcia

*University of South Florida, jairoandresmartinez@gmail.com*

Follow this and additional works at: <http://scholarcommons.usf.edu/etd>



Part of the [Acoustics, Dynamics, and Controls Commons](#), and the [American Studies Commons](#)

## Scholar Commons Citation

Martinez Garcia, Jairo Andres, "A Novel Ultrasonic Method to Quantify Bolt Tension" (2012). *Graduate Theses and Dissertations*.  
<http://scholarcommons.usf.edu/etd/4145>

This Thesis is brought to you for free and open access by the Graduate School at Scholar Commons. It has been accepted for inclusion in Graduate Theses and Dissertations by an authorized administrator of Scholar Commons. For more information, please contact [scholarcommons@usf.edu](mailto:scholarcommons@usf.edu).

A Novel Ultrasonic Method to Quantify Bolt Tension

by

Jairo A. Martinez Garcia

A thesis submitted in partial fulfillment  
of the requirements for the degree of  
Master of Science in Mechanical Engineering  
Department of Mechanical Engineering  
College of Engineering  
University of South Florida

Major Professor: Rasim Guldiken, Ph.D.  
Muhammad Rahman, Ph.D.  
Nathan Crane, Ph.D.

Date of Approval:  
March 7, 2012

Keywords: Surface Acoustic Waves, Bolt Preload, Synthetic Phased Array,  
Ultrasonic Imaging, Structural Health Monitoring

Copyright © 2012, Jairo A. Martinez Garcia

## **ACKNOWLEDGEMENTS**

I owe my deepest gratitude to Dr. Rasim Guldiken, whose encouragement, supervision and support have made this thesis possible. I would also like to thank Dr. Alper Sisman for his direction and insight that has helped me throughout this work. Lastly, I would like to show my gratitude to Dr. Muhammad Rahman and Dr. Nathan Crane for their valuable advice. I feel very lucky to have such wonderful mentors on my thesis committee.

## TABLE OF CONTENTS

LIST OF TABLES .....	iv
LIST OF FIGURES .....	v
ABSTRACT.....	viii
CHAPTER 1: INTRODUCTION.....	1
1.1 Review of Acoustic Waves.....	1
1.1.1 Elastic Waves in Solid Media.....	1
1.1.1.1 General Principles.....	1
1.1.1.2 Bulk Waves.....	4
1.1.1.3 Surfaces Acoustic Waves.....	5
1.1.2 Radiated Field of Ultrasonic Transducers.....	7
1.2 Real Area of Contact.....	10
1.3 Bolted Joints.....	12
1.3.1 Standards and Definitions of Bolted Joints.....	12
1.3.1.1 The Joint Clamping Force.....	12
1.3.1.2 Loosening Process in Bolts.....	13
1.3.1.3 Standard Bolts.....	13
1.3.1.4 The Bolt Tension.....	15
1.3.2 Measuring and Controlling the Bolt Tension.....	15
1.3.2.1 Control of Preload in Bolted Joints.....	15
1.3.2.1.1 Torque Control.....	16
1.3.2.1.2 Turn-of- Nut Control.....	16
1.3.2.1.3 Direct Preload Control.....	17
1.3.2.1.4 Stretch Control.....	17
1.3.2.2 Monitoring of Bolt Tension.....	18
CHAPTER 2: STRUCTURAL HEALTH MONITORING.....	20
2.1 Introduction to Structural Health Monitoring.....	20
2.1.1 Passive Structural Health Monitoring.....	21
2.1.2 Active Structural Health Monitoring.....	22

2.2 Structural Health Monitoring Methodologies using Piezoelectric Transducers .....	23
2.2.1. Electromechanical Impedance .....	23
2.2.2 Ultrasonic Methodologies: Piezoelectric Transducers.....	24
2.2.2.1 Pitch and Catch .....	24
2.2.2.2 Pulse-Echo .....	26
2.2.3 Ultrasonic Methodologies: Transducer Arrays .....	27
2.2.3.1 Linear Arrays .....	28
2.2.3.2 2-D Arrays .....	31
2.2.4 Ultrasonic Image Generation .....	32
2.2.4.1 Phased Array Imaging.....	34
2.2.4.2 Synthetic Phased Array Imaging .....	35
2.2.4.3 The Performance Criteria of an Imaging System .....	37
<b>CHAPTER 3: INSPECTION OF STEEL PLATES VIA ULTRASONIC ACOUSTIC WAVES .....</b>	<b>39</b>
3.1 Calculation of Surface Acoustic Wave Velocity in Steel 1018. ....	39
3.1.1 Experiment Configuration .....	39
3.1.2 Procedure .....	40
3.1.2 Experimental Results .....	40
3.2 Calculation of SAW Attenuation Coefficients in Steel 1018 .....	42
3.2.1 Experiment Configuration .....	42
3.2.2 Procedure .....	43
3.3.3 Experimental Results .....	44
3.3 Estimation of Flaws Position using a Conventional Synthetic Aperture (SA) System .....	45
3.3.1 Experiment Design.....	46
3.3.1 Experiment Configuration .....	48
3.3.1.1 Experimental Procedure.....	49
3.3.2 Experimental Results .....	50
3.4 Chapter Review and Conclusions .....	59
<b>CHAPTER 4: BOLT TENSION ESTIMATION USING SURFACE ACOUSTIC WAVES .....</b>	<b>61</b>
4.1 Conceptual Framework.....	61
4.2 Tension Evaluation of a 1/4in Stainless Steel Bolt.....	65
4.2.1 Experiment Design.....	66

4.2.2 Experiment Configuration .....	69
4.2.2.1 Experimental Procedure.....	71
4.3.3 Experimental Results .....	73
4.3 Tension Evaluation of a 1/2in Stainless Steel Bolt.....	75
4.3.1 Experiment Design.....	76
4.3.2 Experiment Configuration .....	77
4.3.2.1 Experimental Procedure.....	78
4.3.3 Experimental Results .....	80
4.4 Tension Evaluation of a 1/4in Grade 8 Bolt .....	82
4.4.1 Experiment Design.....	83
4.4.2 Experiment Configuration .....	84
4.4.2.1 Experimental Procedure.....	85
4.4.3 Experimental Results .....	87
4.4.4 Error Estimation.....	90
4.4.4.1 Signal to Noise Ratio of the System .....	90
4.4.4.2 Axial Resolution of the System .....	94
4.4.4.3 Conclusions.....	94
CHAPTER 5: CONCLUSIONS AND FUTURE WORK.....	95
5.1 Conclusions.....	95
5.2 Future Work .....	98
LIST OF REFERENCES .....	100
APPENDICES .....	107
Appendix A: Instrumentation Datasheet.....	108
Appendix B: Third Party Permissions .....	110

## LIST OF TABLES

Table 1. Equivalent bolt categorization for standards SAE, ASMT and metric.....	14
Table 2. Real and obtained positions of the machined holes.....	58
Table 3. Error associated with the longitudinal position estimation based in the acoustic images.....	59
Table 4. Parameters employed in the experimental configuration of section 4.2.....	70
Table 5. Parameters employed in the experimental configuration of section 4.3.....	78
Table 6. Parameters employed in the experimental configuration of section 4.4.....	85
Table A1. Instrumentation datasheet .....	108

## LIST OF FIGURES

Figure 1. Piezoelectric transducer radiated sound field .....	8
Figure 2. Angle of divergence of a piezoelectric transducer sound beam. ....	8
Figure 3. Schematic representation of the pressure field distribution of a circular aperture transducer .....	9
Figure 4. Geometrical characteristics of bolts .....	14
Figure 5. Sketch of linear array geometry .....	28
Figure 6. Linear arrays basic operations .....	29
Figure 7. Schematic of linear array focusing. ....	30
Figure 8. Schematic of linear array steering. ....	31
Figure 9. Schematics of 2-D arrays geometries .....	32
Figure 10. Example of an ultrasonic image. ....	33
Figure 11. Schematic operation procedure of the synthetic phased array. ....	36
Figure 12. Schematic of the initial position of the wedge. ....	40
Figure 13. Signal obtained from the reflected SAW generated in the 1018 steel plate. ....	41
Figure 14. Drawing of initial position of wedge. ....	44
Figure 15. Plot of the intensity measurements versus the wedge position .....	45
Figure 16. Photo of the bulk waves experiment configuration. ....	46
Figure 17. Schematic configuration of the bulk wave experiments. ....	48

Figure 18. Longitudinal images of a 1018 steel plate generated by synthetic phased array using bulk waves.....	51
Figure 19. Longitudinal images of a 1018 steel plate showing enlarged details .....	52
Figure 20. Enlarged longitudinal image of the first hole set.....	52
Figure 21. Enlarged longitudinal image of the second hole set.....	53
Figure 22. Enlarged longitudinal image of the third hole set .....	54
Figure 23. Transversal view of the first hole set.....	55
Figure 24. Transversal view of the second hole set. ....	56
Figure 25. Transversal view of the third hole set.....	56
Figure 26. Combination of longitudinal and transversal images of a 1018 steel plate using synthetic phased array imaging technique .....	57
Figure 27. Schematic set up of the proposed methodology. ....	61
Figure 28. Enlarged representation of the real contact surface of the clamped plate and washer .....	62
Figure 29. Schematic representation of change in the RAC due to tension increments. ....	63
Figure 30. Representation of SAW reflection from 4 different boundaries. ....	64
Figure 31. Photo of 1/4 inch stainless steel bolt tension evaluation. ....	66
Figure 32. Sketch of transducer-wedge position with respect to the targeted hole. ....	68
Figure 33. Drawing of the 1018 steel plate used for all SAW experiments in this research .....	71
Figure 34. Generated images of the steel plate at 15dB of dynamic range. ....	73
Figure 35. Averaged 1-D images at 6dB. ....	74
Figure 36. Photo of 1/2 inch stainless steel bolt tension evaluation. ....	75

Figure 37. Schematic of wedge-transducer initial position. ....	79
Figure 38. Generated images of the steel plate at 15dB of dynamic range. ....	80
Figure 39. Averaged 1-D images at 6dB. ....	81
Figure 40. Plot of torque applied versus position of the acoustic wall. ....	82
Figure 41. Photo of 1/4 inch grade 8 bolt tension evaluation. ....	83
Figure 42. Schematic of the wedge initial position.....	86
Figure 43. Images generated at 15dB with the SAW reflections from a 1/4in bolt with a stainless steel washer.....	87
Figure 44. Averaged 1-D images at 6dB. ....	88
Figure 45. Graph of the torque applied versus the position of the acoustic wall.....	89
Figure 46. Signal to noise ratio of the bolt reflections based in original signals.....	91
Figure 47. Signal to noise ratio of the plate edge reflections based in original signals....	92
Figure 48. Averaged signal to noise ratio of the bolt and plate edge reflections based in original signals.....	93
Figure B1. Publication permission NDT Resource Center.....	110

## **ABSTRACT**

The threaded fasteners are one of the most versatile methods for assembly of structural components. For example, in bridges large bolts are used to fix base columns and small bolts are used to support access ladders. Naturally not all bolts are critical for the operation of the structure. Fasteners loaded with small forces and present in large quantities do not receive the same treatment as the critical bolts. Typical maintenance operations such tension measurements, internal stress checking or monitoring of crack development are not practical due to cost and time constraints. Although failure of a single non-critical fastener is not a significant threat to the structure's stability, massive malfunction may cause structural problem such as insufficient stiffness or excessive vibrations.

The health of bolted joints is defined by a single parameter: the clamping force (CF). The CF is the force that holds the elements of the joint together. If the CF is too low, separation and bolt fatigue may occur. On the other hand, excessive CF may produce damages in the structural members such as excessive distortion or breakage. The CF is generated by the superposition of the individual tension of the bolts. The bolt tension, also referred as bolt preload, is the actual force that is stretching the bolt body. Maintaining the appropriate tension in bolts ensures a proper CF and hence a good health of the joint.

In this thesis, a novel methodology for estimating the tension in bolts using surface acoustic waves (SAWs) is investigated. The tension is estimated by using the reflection of SAWs created by the bolt head interference. Increments in the bolt tension raise the points of interaction between the waves and the bolt head (real area of contact), and hence the position of the reflective boundaries. The variations are estimated using the “conventional linear synthetic array” imaging technique. A singular transducer is actuated from predefined positions to produce an array of signals that are subsequently arranged and added to construct an acoustic image.

Three sets of experiment are presented in this research for validating the proposed concept: tension estimation of a ¼ inch stainless steel bolt, a ½ inch stainless steel bolt and ¼ inch grade 8 bolt. Acoustic images of the surface of the clamped plate illustrate a clear trend in the position of the reflective boundary when torque is changed. In all cases, the torque increments increase the real area of contact and therefore the position of the reflective boundary. As expected, the real area of contact grew from the bolt head center to the perimeter, which causes an effect of apparent movement of the boundary. This research proves the potential of the ultrasonic imaging methodology to measure applied tension. The result showed that the system can be used to successfully inspect tension in bolts of ½ and ¼ inches. The methodology investigated in this thesis is the first steps towards the development of bolt tension sensor based on surface acoustic waves.

## CHAPTER 1: INTRODUCTION

### 1.1 Review of Acoustic Waves

#### 1.1.1 Elastic Waves in Solid Media

##### 1.1.1.1 General Principles

The propagation of elastic waves in solid media is typically described by partial differential equations. The Newton's second law is applied to a vibrating particle within a body in order to create the explicit 1-D homogeneous wave equation [1]:

$$C^2 \frac{\partial^2 u}{\partial x^2} = \frac{\partial^2 u}{\partial t^2} \quad (1)$$

where  $u$  is the displacement,  $C$  the wave velocity and  $x$  and  $t$  the position and time respectively.

The “wave velocity” is propagation speed of a disturbance traveling through a specific media. The wave velocity is dependent on material selection, mode and frequency of operation. The mode dependency means that waves propagating in different modes, e.g longitudinal and shear waves have different velocities. The wave velocity is also frequency dependent, different harmonics of Lamb waves have different propagation velocities. Finally the wave velocity is material dependent because every material has specific wave velocities for the different wave modes [2].

The frequency dependency of the elastic waves generates a phenomenon called dispersion. The wave dispersion is observed as pulsed wave i.e. continuous drop in the amplitude of the follow by an increment in the duration (width) of the pulse. This behavior is explained by the Fourier harmonic analysis, which states that all waveforms repeated in time can be created by a sum of sine and cosine waves with different frequencies and phases [3]. Hence all the waves are a superposition of an indeterminate number harmonics with different frequencies and amplitudes. In this sense, the harmonics that travel with different speeds tend to separate from each other, generating the wave shape changes mentioned previously [2].

The existence of several “wave velocities” within a single wave leads to define two additional velocity concepts: the phase velocity ( $C_p$ ) and group velocity ( $C_g$ ). The  $C_p$  is the individual propagation speed of the harmonics in the wave package, while the  $C_g$  is the velocity with which the complete wave package propagates through the media [2]. Additionally a fourth type of velocity is present in harmonic waves: the particle velocity ( $\dot{u}$ ). The particle velocity is the velocity with which material particles move as the wave propagates. The particle velocity is normally much lower than the phase and group velocities [1].

The acoustic impedance ( $Z$ ) is a material property which plays a major role for the acoustic image generation. It denotes the amount of stress that material particles need in order to acquire a specific velocity.  $Z$  is defined as the product of the material density ( $\rho$ ) and the wave velocity ( $C$ ):

$$Z = \rho C \quad (2)$$

The acoustic impedance has especial importance in the transmission of elastic waves: the difference in acoustic impedance of two materials defines the transmission factor of an elastic wave traveling through their interface. The higher the difference in  $Z$ , the lower the transmission factor, therefore most of the energy of the wave is reflected back by the interface. This is the reason for applying matching gels between the transducers and the transmitting media. The ceramic material surrounding the piezoelectric crystal has lower acoustic impedance than the inspected metal, hence without the couplant, all the waves intended to be transmitted into the media are reflected back to the crystal.

The “friction” of the acoustic waves is called attenuation. Ultrasonic waves suffer from energy losses associated with the irreversibility of the propagating system. Scattering due to porosities, grains or even cracks generates losses in the propagating waves. In addition the heat generation caused by the moving constrains of the particles involved in the wave propagation also generates energy losses.

The attenuation is normally defined as an exponential loss in the initial amplitude of the traveling waves [4]:

$$A = A_0 e^{-\alpha z} \quad (3)$$

Where  $A$  is the actual amplitude of the wave at the point of evaluation,  $A_0$  is the initial wave amplitude,  $z$  is the separation distance of propagation and  $\alpha$  is the attenuation coefficient.

### **1.1.1.2 Bulk Waves**

“Bulk waves” is the name of a group of waves that propagates with no boundary intervention. While guided waves such as surface acoustic or Lamb waves need boundaries in order to be created, bulk waves propagate in media with no boundaries (infinite). An infinite media is an object with dimensions much larger than the wavelength [5]. There are two types of bulk waves, pressure waves, a.k.a longitudinal waves, and shear waves, a.k.a transverse waves. The longitudinal waves are characterized by particle motion parallel to the direction of wave propagation while the shear waves have particle motion perpendicular to the direction of the wave propagation [1].

Pressure and shear waves may exist together in an unbounded media, furthermore they do not interact with each other. Bulk waves are non-dispersive, hence longitudinal and shear waves have a unique non-frequency dependent velocity [1]:

$$C_P^2 = \frac{1-\nu}{(1+\nu)(1-2\nu)} \frac{E}{\rho} \quad (4)$$

$$C_S^2 = \frac{1}{2(1+\nu)} \frac{E}{\rho} \quad (5)$$

Where  $C_p$  is the pressure (longitudinal) wave velocity,  $C_s$  is the shear (transversal) wave velocity,  $\nu$  is the poisson's ratio,  $E$  the Young modulus and  $\rho$  is the density.

### 1.1.1.3 Surfaces Acoustic Waves

The simplest type of guided acoustic waves is the Surface Acoustic Waves (SAW). The most notorious characteristic of these waves is the limited penetration of the excitation energy: the particle displacements decay rapidly with material depth. Elliptical particle movement, curved surfaces traveling and high attenuation factors product of interaction with liquid boundaries are important features of these waves [6].

The elliptical movements are created by simultaneous longitudinal and shear displacements. Contrary to other kind guided waves, the SAWs are non-dispersive. The longitudinal and shear displacements travel with the same velocity along the material surface, which creates unique velocity for the entire disturbance as illustrated in eqn. 11. References [6, 7, 8] have developed mathematical models to represent the particle displacement of SAW:

$$u = A(re^{-qz} - 2sqe^{-sz}) \cos k(x - c_R t) \quad (6)$$

$$w = Aq(re^{-qz} - 2e^{-sz}) \sin k(x - c_R t) \quad (7)$$

$$r = 2 - \left(\frac{c_R}{c_P}\right)^2 \quad (8)$$

$$q = \sqrt{1 - \left(\frac{c_R}{c_S}\right)^2} \quad (9)$$

$$s = \sqrt{1 - \left(\frac{c_R}{c_T}\right)^2} \quad (10)$$

$$c_R = \sqrt{\frac{1}{2(1+\nu)} \frac{E}{\rho} \left(\frac{0.87+1.12\nu}{1+\nu}\right)} \quad (11)$$

Where  $c_R$  is the Rayleigh velocity,  $c_S$  and  $c_P$  are transversal and longitudinal wave velocities respectively.  $z$  is the material depth,  $x$  is the propagation coordinate,  $k$  is the

wavenumber ( $f/C_R$ ),  $u$  and  $w$  are the longitudinal and transversal displacements respectively,  $f$  is the wave frequency,  $\nu$  is the poisson's ratio,  $E$  the Young modulus and  $\rho$  is the density.

The equations confirm the strong dependency of longitudinal and shear displacements with the wave penetration  $z$ . From the eqn. 6 and  $w = Aq (re^{-qz} - 2e^{-sz}) \sin k(x - c_R t)$  eqn. 7, the strong reduction of the displacements product of  $z$  increment is observable: after two wavelengths, shear and longitudinal movements are almost inexistent.

The SAW also suffer from attenuation, reflection and refraction. Obstacles created by the propagation materials irregularities such as grain boundaries, point defects or even electrons and photons can generate such phenomena [8]. In addition to the usual causes of attenuation, SAW are also attenuated, refracted and reflected due to interactions with entities in contact to the propagation surface. The attenuation phenomenon generated by solid-liquid interfaces is widely described in [6, 8]. The authors expose how SAW can be strongly attenuated when liquids are in contact with the surface. Compressional waves are transmitted and absorbed by liquid entities in the surface; this effect produces a considerable amount of energy loss.

The attenuation factor due to compressional losses is shown in eqn. 12 [8]. This phenomenon applies to gases and liquids surrounding the propagation material. The low density of gases reduces the attenuation effect considerably, so in the case of air for example, the attenuation is normally so low that it is consider a free boundary problem [8].

$$\alpha_{Rayleigh} = \frac{\rho_{Liquid} V_{Liquid}}{\rho_{Pr.Mat.} V_{Pr.Mat.} \lambda} \quad (12)$$

### ***1.1.2 Radiated Field of Ultrasonic Transducers***

Although PZTs are apparently single acoustic sources, in reality the transducer active surface is a group of individual points vibrating together. This generates a phenomenon called wave diffraction. Szabo (2004) describes the diffraction as “a wave phenomenon in which radiating sources on the scale of wavelengths create a field of mutual interference of waves generated along the source boundary “. In the case of PZT diffraction creates a pressure field commonly called transducer beam or sound field (Figure 1) [9].

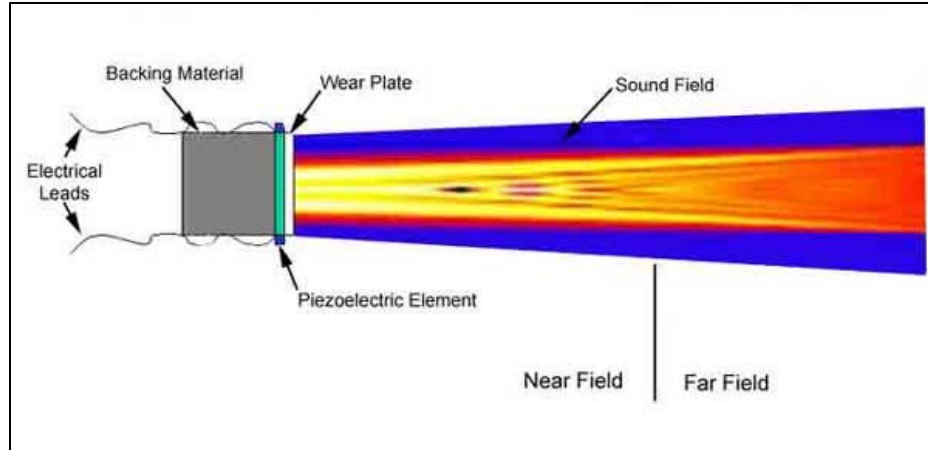


Figure 1. Piezoelectric transducer radiated sound field. Figure taken from NDT resource center, [4].

The representation of the transducer beam is actually a plot of the pressure distribution along the scanned material. Lighter colors stand for higher pressure intensities, while darker color for low pressures. Another common representation uses polar coordinates to indicate the maximum pressure. The plot is valid just for a concrete longitudinal position within the beam (commonly the base), the graph shows the maximum pressure intensity (the radius) for all the direction in which the waves can travel (the angle). This representation is very useful for the localization of side lobes. Reference [10] illustrates some of these figures.

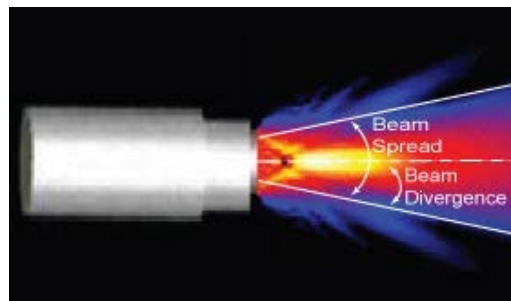


Figure 2. Angle of divergence of a piezoelectric transducer sound beam. Figure taken from NDT resource center, [4].

Sound beams can be focused as light rays. A lens attached to the transducer face can change the transducer natural focal area into a specific point [9]. Frequently the focal area of the transducer is assumed to be the region of the pressure field where the transversal pressure distribution of -6dB (50%) takes the minimum value. The -6dB distribution is a difference of 50% between the maximum and minimum pressure intensities. In Figure 2 another important characteristic of the beam is shown, the beam divergence angle. This angle is an indication of the spreading in the acoustic waves, it is calculated by finding the -6dB pressure intensity drop and measuring the angle just as the figure.

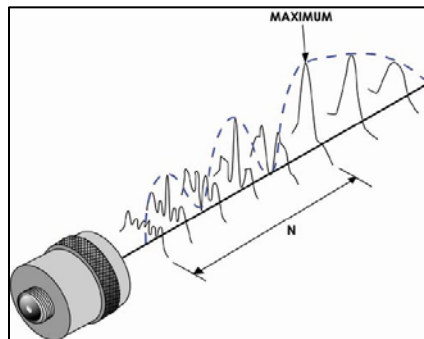


Figure 3. Schematic representation of the pressure field distribution of a circular aperture transducer. Figure taken from NDT resource center, [4].

There are two more regions within the sound field: The far and near field. The far field represents the region where the transversal pressure distribution always find its maximum in the centerline of the beam, in the case of a circular aperture transducer (transducer with circular contact surface) it is the line that pass through the center and is perpendicular to the transducer (Figure 3). On the other hand, the near field is the region where the location of maximum varies with the distance to the source.

The end of the near field is the point of maximum transverse relative intensity within the focal area, also known as the natural focus. The Fresnel approximation of spatial diffraction can be used to calculate the exact pressure distribution of a specific beam. Detailed explanation of the methodology can be found in reference [9]. A common approximation of the length of the near field ( $N$ ) for P-waves generated by circular aperture PZT is the following [10]:

$$N = \frac{D^2 f}{4C_L} \quad (13)$$

Where  $N$  is the length of the near field,  $D$  is the diameter of the circular aperture,  $f$  is the wave frequency and  $C_L$  is the longitudinal wave velocity.

## 1.2 Real Area of Contact

The surface of a solid material can be described as a series of micro scaled peaks and valleys with a specific pattern which determines the rugosity of the surfaces. Usually the heights of those peaks have a random behavior represented by a normal Gaussian distribution [11]. The existence of peaks in rough surfaces implies a very interesting phenomenon: solid materials touch each other only in the discrete areas where the peaks tips collide. The summation of the microareas of contact is known as the “real area of contact” (RAC) [12].

Although the RAC is a parameter related directly to the friction force, it is not commonly employed in practice. This is due to simple fact that it is impractical to measure the RAC. The Amontons-Coulomb law, a.k.a “Dry Friction Law”, uses a simple methodology to calculate the friction force (F). It states that F is directly proportional to the force normal to surfaces in contact (N) and that the proportionally coefficient is the “coefficient of friction” ( $\mu$ ) [13]:

$$F = \mu N \quad (14)$$

One can imply from the dry friction law that the RAC is not involved in the friction force creation, but that is not the case. Indeed, it is in the RAC where all interactions between the solids in contact take place [12]. The formation of friction force in the RAC is explained by the interaction among molecules and the mechanical deformation of the peaks. The molecules build up adhesive forces due to electromechanical relations: Vander Waal forces, ionic, covalent and metallic links. These connections between molecules generate opposition to the relative movement among objects.

In addition to the molecular forces, the friction force is completed by the mechanical resistance of the peak tips. The peaks must suffer plastic and/or elastic deformations before any relative movement can be produced [12].

Several researchers have shown that the RAC is in fact proportional to the normal force when either elastic or plastic deformations are present [11, 12, 13]. The presence of only elastic deformations of the peaks implies the existence of a constant mean micro contact

area ( $\bar{a}$ ). Further increments of RAC during this condition are produced by multiplication of peaks in contact ( $n$ ) [11]:

$$\text{RAC} = \sum_1^n a = n \times \bar{a} \quad (15)$$

### **1.3 Bolted Joints**

The threaded fasteners are one of the most versatile methods for assembly of structural components. In bridges, for example, large bolts are used to fix base columns and small bolts are used to support access ladders. Naturally not all bolts are critical for the structure operation. Fasteners loaded with small forces and present in large quantities do not receive the same treatment as the critical bolts. Typical maintenance operations such as tension measurements, internal stress checking or monitoring of crack development are not practical due to cost and time constraints. Although failure of a single non-critical fastener is not a significant threat to the structure's stability, massive malfunction may cause structural problem such as insufficient stiffness or excessive vibrations.

In the following sections some generalities of bolted joints are presented, definition of relevant parameters such as bolt preload and pitch are explained. The last section is a recompilation of some methodologies used for bolt tension measurement and control.

#### ***1.3.1 Standards and Definitions of Bolted Joints***

##### ***1.3.1.1 The Joint Clamping Force***

The clamping force (CF) is the force that maintains together the elements of the joint. If the CF is too low (loosened bolts), separation and bolt fatigue may occur [14]. On the

other hand, excessive CF may produce damages in the members such as excessive distortion or breakage. More complex phenomena like stress corrosion and hydrogen embrittlement may be caused by excessive CF [14].

### ***1.3.1.2 Loosening Process in Bolts***

The loosening process is explained as a progressive “slip” at the thread-plate and head-plate interfaces [15, 16, 17, 18]. The “slip” is mainly caused by direct and indirect shear loads applied to the joint [19, 20]. The bolt tension also tends to loosen the bolt due to the generation of a loosening moment produced by the helical shape of the thread [19]. Another factor that contributes significantly to the loosening process is the elastic deformation suffered by the clamped members. It causes direct slip in the bolt head and build up the loosening moment in the bolt threads [19].

### ***1.3.1.3 Standard Bolts***

The standards of the threaded fasteners employ specific terminology for the parameters that define the general geometry of bolts. In Figure 4 the most important parameters are illustrated. The pitch is separation between two contiguous threads. The nominal diameter is the largest diameter of the screw thread. The bolt length is measure from the head base. The thread length is the distance from the bolt end to the beginning of the screw thread [21].

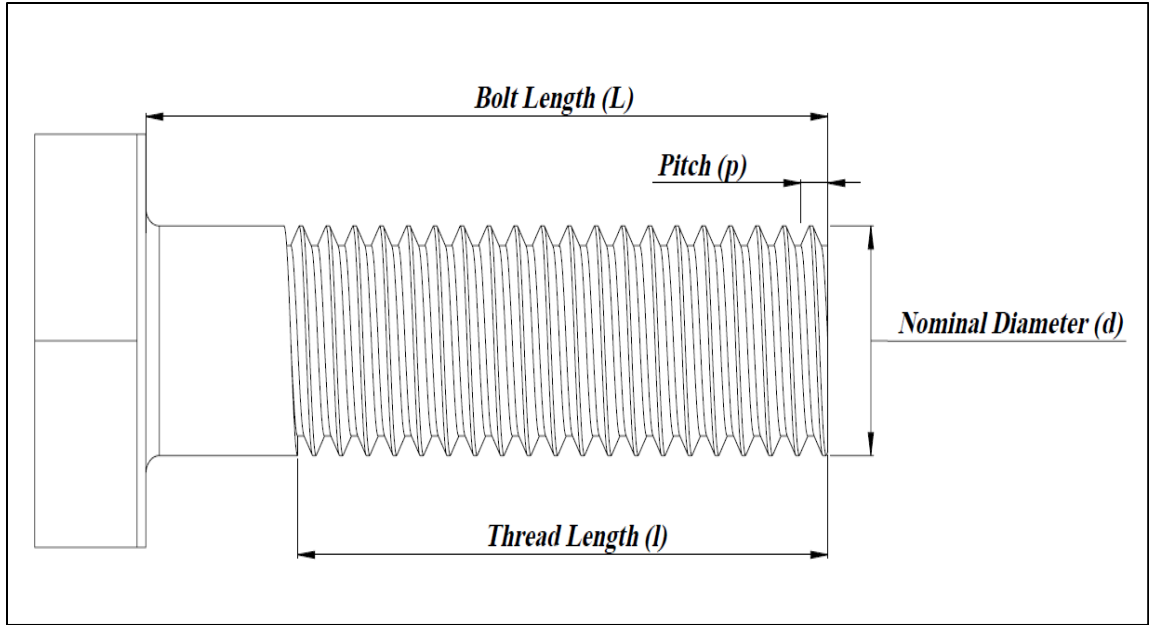


Figure 4. Geometrical characteristics of bolts.

The bolts ultimate and yield strength are standardized by 3 different parties: SAE, ASTM and International Metric. Every one of them catalogues the bolts according to the mechanical strength and the size range. Table 1 presents some examples of the categorization.

Table 1. Equivalent bolt categorization for standards SAE, ASMT and metric.

	Designation	Size Range	Minimum Yield strength
SAE	Grade 8	¼ - 4 in	130 Kpsi
ASTM	A354 grade BD	¼ - 4 in	130 Kpsi
Metric	10.9	M5-M36 (mm)	830MPa

#### ***1.3.1.4 The Bolt Tension***

The CF is generated by the superposition of the individual tension of the bolts present in the joint. The bolt tension, a.k.a bolt preload, is the actual force that is stretching the bolt body. The preload is related to the relative stiffness of the bolt and clamped members. In order to calculate the required bolt tension for generating a specific CF, the interaction between the bolt and the members should be modeled as three springs in series. In reference [21], a complete procedure for finding the CF by the application of a specific bolt tension is presented.

#### ***1.3.2 Measuring and Controlling the Bolt Tension***

There are two different stages in the operation of bolted joints that require tension control: Assembly and regular operation. Geometric characteristics like the stiffness or bolt position usually do not change during the assembly or the regular operation. This is the reason why the accurate tension control is necessary to ensure a correct CF [22]. In the assembly process, the tension is controlled to guarantee a correct preload and therefore the correct CF. On the other hand in the regular operation, the tension is monitored to ensure a safe CF level during the joint life.

##### ***1.3.2.1 Control of Preload in Bolted Joints***

There are 4 basic methodologies used to control preload: Torque Control, Turn-Of-Nut method, Direct Preload Control and Stretch Control.

### 1.3.2.1.1 Torque Control

The torque control is the most used method for controlling bolt tension. Torque wrenches of manual, pneumatic and hydraulic implementation are common in the market. These allow the user to apply a large range of torque values and accuracies [23]. The inherent dependency of this method on uncertain variables such as friction factor, torsion bending and threads plastic deformation, reduces the accuracy of the applied tension to 25%-30% [23, 24].

A common methodology for calculating the torque required for achieving a specific tension in the bolt is presented by [21]. The formulation uses a modified friction factor ( $K$ ) to relate the torque to a specific tension:

$$T = KA_t 0.85S_y d \quad (16)$$

Where  $K$  is the friction factor,  $A_t$  is the tensile stress area,  $S_y$  is the bolt yield strength,  $d$  is the bolt nominal diameter and  $T$  is the torque applied. A usual approximation for  $K$  is 0.2.

### 1.3.2.1.2 Turn-of- Nut Control

This method consists of two stages. In the first phase the bolt is tightened with a conventional torque wrench until it reaches approximately 75% of the material ultimate strength [25]. The second stage involved a turn of 180° after the first tightening. Every turn of the bolt increases the bolt length (and therefore the tension) by an amount close to the bolt pitch. The final turn almost assure a tension levels that surpass the bolt yield point [25].

This 2-step methodology has a tension accuracy of 5%, but can only be used in fasteners with ductile materials and long and well-defined elastic deformation regions [25].

#### *1.3.2.1.3 Direct Preload Control*

This category refers to methodologies that use direct estimators of the tension such as strains, stress or deformations. Strain gages can measure very precisely strain in the bolts or in the clamped elements. Knowledge of the bolt strain leads to tension estimation with accuracy of around 1% [26]. Washers with special designs suffer plastic deformation in the tightening process and show an indicator when a specific tension is reached. These crush washers have accuracy of about 4%-10% [26]. In addition to strain and deformation, rupture is also used to estimate bolt tension. Tension control bolts have special heads that break when a specific preload is achieved. The main issue with these methodologies is the high cost of the individual fasteners; calibration may also be a problem.

#### *1.3.2.1.4 Stretch Control*

The bolt tension can be calculated using the Hook's law of elasticity. The law states that the stress produced in the bolt body by the preload is proportional to the bolt elongation. The stretch control uses measurements of the bolt length changes to estimate stress in the bolt and therefore preload. This approach does not involve any interactions of the bolt with the plate, which erase any uncertainties due to friction. Furthermore the literature availability of very precise elastic properties provides to methodology the accuracy of the instrument used to measure the bolt elongation [26].

Additionally this approach also permits the tension monitoring the by comparing the bolt length. The length obtained during the installation may be as the “correct operation” reference. Length variations associate to irregular surfaces, uneven machinated processes, temperatures changes, plastic deformations and bending displacements introduce error to the length estimation. Micrometers and ultrasonic equipment are used for stretch control [26].

### ***1.3.2.2 Monitoring of Bolt Tension***

The response analysis of induced vibrations may be used to characterize the general state of bolted joints. For instance, in references [27, 28] statistical manipulation is employed to calculate changes in the vibration signals due to bolt preload variation. The response from low frequency vibrations are evaluated using advance signal processing algorithms. Recently, signal processing algorithms based in Empirical Mode Decomposition (EMD) have been used to detect changes in vibration signals produced by impact hammers; the technique was validated empirical and by Finite Element Analysis (FEM) [29].

Vibration can be used to find general problems in a structure such as stability or resistance, but finding the location of the problem may be a difficult task for those methodologies. Some studies take care of this issue using local approaches to find the tension of single fasteners [24, 30, 31, 32]. The deformations on the fastener are measured by [24], using automatic digital image correlation (ADIC). In [32] piezoelectric wafers are installed in fasteners in order to sense changes in the electromechanical impedance of the bolts. Some researchers have used guided ultrasonic waves to measure bolt tension. Modulation in lamb waves generated by the loosened

bolts is used by [30] to calculate a joint damage index. Transformation between the wave modes due to stress is exploited by [31] with the purpose of calculating stress levels, tension and CF in the threaded joints.

## **CHAPTER 2: STRUCTURAL HEALTH MONITORING**

### **2.1 Introduction to Structural Health Monitoring**

A crucial step in the mechanical design components is the prediction of their operative life. Uncertain loads, ambient conditions, material properties or even misuse are some of the cases that a designer has to overcome in order to predict the life of a specific component. Usually, security factors and redundant designs assure structural integrity even in the worst case scenarios. These contingencies generate problems such as increased cost, less efficient designs or over dimensioned structures. Furthermore designs that support human lives, like airplanes or civil structures, have additional constrains.

The necessity to predict the operative life of components, urged the creation of methods that permit the monitoring of the “health” of structures. The methods that are able to do it without damaging the monitored parts are called non-destructive evaluation (NDE). The principal problem associated with NDE is the necessity of off-line evaluation of components. NDE techniques need very controlled conditions during evaluation processes which normally involve disassembly or service leaving of the monitored component. This kind of monitoring is very common in maintenance programs of any kind of machinery or structure [33].

Structural health monitoring (SHM) overcomes this concrete problem: the evaluation of health is done while the component or structure is in operation. There are two types of SHM according to its monitoring approach. The first kind is called passive SHM, it compares the behavior of the structure while is aging with the original or “brand new” behavior [33]. The second uses inspection of the components to find actual problems in the structures, this is called active SHM [33].

### ***2.1.1 Passive Structural Health Monitoring***

A very clever way to establish the general health of a structure is finding changes in specific properties that can be related to explicit problems. For instance, the elevated temperature in a motor output shaft can be caused due to friction problems. Taking a thermography of a shaft with bearing problems and comparing it with one with optimal conditions may show an increased temperature profile. Then the general state of motor bearings can be monitored by a specific program of thermography [34]. Similar results can be achieved by measuring vibration or monitoring stress levels in critical locations. Even some parameters of machines such as current, velocity or torque can indicate misaligns or bearing failure [34].

Static structures can also be monitored. For instance, [35] presented a statistical method to estimate growing rate and size of cracks in metallic structures by using piezoelectric transducers (PZT). The method consists of the calculation of the change in signal parameters such as peak to peak variation, amplitude variance, root mean square, kurtosis, crest factor and k-factor.

### ***2.1.2 Active Structural Health Monitoring***

Non-destructive evaluation (NDE) generally is very meticulous and requires that the part to be inspected stop working. The best way to avoid this problem is integrating the NDE into the structure itself. It permits the evaluation and analysis of the structural health every time it is needed and it does not interrupt the normal operation of the part. This approach is called active structural health monitoring.

The ultrasonic technologies have a bright future in the active SHM due to the capacity of scanning relative large areas with low power consumption, good accuracy and low cost [33]. The piezoelectric wafer transducers (PWT) are small in size and hence they can be easily embedded in the actual structures.

The accuracy of embedded piezoelectric transducers is discussed by [36]. A laser beam is employed to produce Lamb waves in the scanned part while embedded PZT receive the signals. An image generation algorithm is tested for finding flaws three different applications: An elbow pipe joint, a carbon fiber reinforced plastic plate and a stringer-skin joint. In the last application Lee et al. try to detect a stringer-skin disbond [36]. Different wave behaviors are captured with different PZT position. It is concluded that positioning the transducer in the stringer and generating the waves in the skin permits establishing the dimension of the disbond and some additional details such as the “kissed part”. Additional applications of active SHM are presented in references [37-46].

## **2.2 Structural Health Monitoring Methodologies using Piezoelectric Transducers**

Some methodologies for PZT based SHM are presented in this section. The general principles, strengths and weaknesses of every technique are reviewed and applications are discussed. More details and explanation of the methods following presented can be found in the references.

### ***2.2.1. Electromechanical Impedance***

The electromechanical impedance method use PZT to sense the mechanical impedance of the tested structure. Changes in the mechanical impedance are attributed to the mass or stiffness changes, therefore it is a reliable parameter for the inspection of the general health of a structure [37, 38]. This approach is also used in vibration methods such as the frequency response functions [37]. A PZT attached to a vibrating structure reacts by changing its electrical impedance [39]; this phenomenon is known as the electromechanical effect. The real portion of the device impedance is normally used as the leading parameter in SHM [37], authors as Liang et al. (1994) and Bhalla and Soh (2003) developed models that demonstrate the reason for such behavior [40, 41].

The electromechanical impedance has some advantages over other SHM methodologies. Compared to regular vibration methods, this method use much higher frequencies (in the KHz order), which make it much more sensitive. The electromechanical impedance can almost be as sensitive as regular ultrasonic NDT approaches but it requires less complicated equipment and the analysis does not require an expert for interpretation [37]. Compared with other vibration approaches, the electromechanical impedance allows

sensors and actuators with self-diagnostic capabilities and low vibration interference, which permit very accuracy results.

Modeling the relation of electrical impedance of the PZT with the mechanical impedance is required for fully understanding the structural problems. Finding an accurate relationship of the electrical response to mechanical excitation is the principal drawback of this methodology [39]. The common applications of the electromechanical method are small machinery parts with natural frequencies in the KHz order, a good example of this are aircraft turbo-engine blades [39].

### ***2.2.2 Ultrasonic Methodologies: Piezoelectric Transducers***

Analyzing the response of a structure to specific ultrasonic impulses can lead to estimation of structural problems such as inadequate stiffness, mass loss or even crack growing. Following some methodologies that use ultrasonic waves produced by piezoelectric transducers in order to detect such defects is presented.

#### ***2.2.2.1 Pitch and Catch***

The pitch and catch technique refers to the employment of two different transducers to send and receive guided waves. The waves are sent from the transmitting transducer (T) and acquired by the receiving transducer (R) with information about the material present between them. The waves used in the pitch and catch technique are generally guided waves that can be strongly influenced by small variations in the stiffness or thickness of the material [42] . The pristine condition of the part to be evaluated is taken as baseline for variation of the waves. Modifications in amplitude, dispersion, phase or time of flight

are indicative of changes in the structure of the monitored part. Lamb waves of different modes are used commonly with this technique.

The principal strength of the pitch and catch method is its high sensitivity to local structural problems such as cracks, corrosion or disbands [42]. This technique can be used for manual inspection in schedule maintenance activities or as automatic monitoring system. The technique is especially useful in composite structures [42].

Limited space between two transducers is a drawback of this methodology. The waves only provide information from the material in-between the transducers. Filtering the acoustic signal may be a necessity for very detailed analysis. For instance, [43] develops a filtering algorithm for diminishing ringing effects which are common in the imaging generation of concrete structures using pitch and catch techniques.

The pitch and catch technique is commonly used for debonding detection. In reference [43], a pitch and catch application with SAW is used to find structural problems in carbon fiber-reinforced polymers (CFRP) attached to concrete specimens. The research shows the capability of the technology to monitor the structural health of the specimens and explain the effectiveness of the methodology. In reference [30], Lamb wave modulation is used to estimate stiffness problems in a bolted joint. The authors calculate a damage index of the joint based in the wave modulation. In reference [42], additional realized applications for this methodology can be founded.

### ***2.2.2.2 Pulse-Echo***

The principle of operation the pulse-echo method is based in the reflection of acoustic waves. The waves generated in the material are partially reflected by holes, corrosion, debonding and other defects. The reflected waves carry information that is received by the transducer. The time that it takes for the waves to hit and return to the transducer is called time of flight (TOF). The TOF provides the position of the reflective boundary [33]. The amplitude and frequency of the reflected waves may be used to estimate the size and shape of the defects. Pressure waves are normally employed for through-the-thickness pulse-echo scanning and guided waves such as Lamb or SAW are used for longitudinal monitoring [33]. This technique is used in the experiments presented in Chapters 3 and 4.

The simple configuration of the methodology is very advantageous for manual and automated structural monitoring [42]. Regularly only one PZT is used as receiver and transmitter which reduce costs and set up time. This technique is generally employed for imaging generation due to its inherent capacity for defect localization. By mapping the reflection location of all the reflective points, an image with the size and position of all the features in the scanned area can be created. Imaging generation is explained in the final section of this chapter.

The principal limitation associate with this method is the difficulty of differentiating boundaries that are close to each other. Proximate defects tend to create reflections that superpose while traveling through the scanned material. Separating the individual effect

of each one is critical for a good signal analysis [42]. In some cases this procedure cannot be done correctly, which lead to errors in the estimation of size and position of the flaws. Also, the waves employed in the pulse-echo approach generally should be low dispersive in nature such as bulk waves or SAW.

Application of the pulse-echo approach can be found from medical imaging to concrete pipes monitoring. In reference [44] ultrasound based techniques for concrete pipe inspection are presented. The pulse-echo methodology is presented as a viable approach for cracks, fractures and holes detection. Air-coupled pulse-echo is shown in [45], impact hammers generate ultrasound vibration in a concrete plate with artificial generated defects. The waves are then transmitted to the air where a specially insulated microphone receives the signal. The microphone is moved along the plate to create an image based on the frequency changes of the received waves.

### ***2.2.3 Ultrasonic Methodologies: Transducer Arrays***

Instead of creating an acoustic beam with a single PZT, a defined number of transducers are placed in a specific configuration in order to generate a controlled beam [46]. The increased number of waves that are created by the array allows the creation of images at every test location, which is an obvious decrease in the manual scanning times. Arrays may also be used as flaw radars in metal structures, they can be electronically controlled to scan large areas without the necessity of moving parts [47].

The generation of images is based in the reflected waves created by changes of acoustic impedance inside the material, just as the regular pulse-echo approach. Additionally, the

arrays are able to focus and steer the generated and received signals by applying delays and gains in the elements. This enables to suppress the generation and reception of waves that propagate in undesired directions [47]. In the following sections two array geometries are presented: Linear arrays and 2-D arrays. The principal characteristic of the arrays along with beam formation capabilities and applications is explained.

### 2.2.3.1 Linear Arrays

A linear array is defined by 3 important parameters: Pitch, number of elements and element width (Figure 5) [47]. Normally the element width is much smaller than the element length, so it is commonly modeled as semi-infinite plate with undefined length. This characteristic makes the linear arrays insensitive to the longitudinal direction of the element, therefore only plane images can be generated through linear arrays [46].

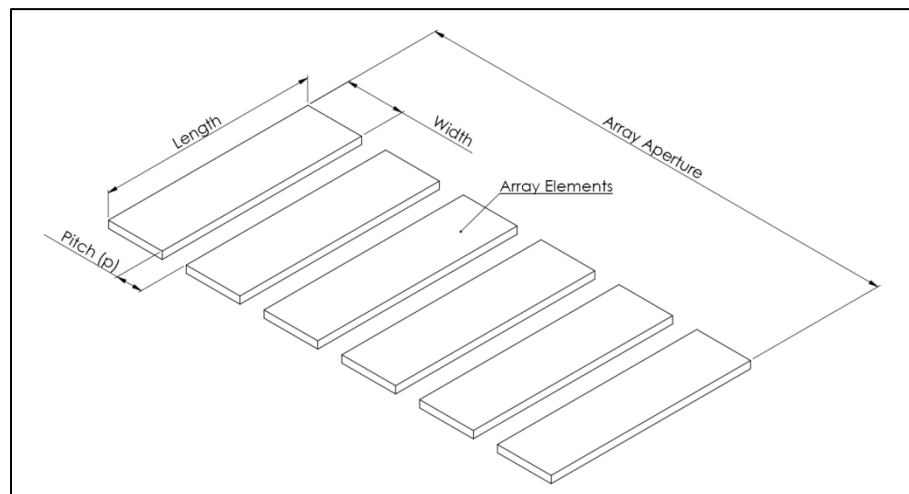


Figure 5. Sketch of linear array geometry

A great advantage of the transducer arrays over the single transducer approach is the capacity to create a common acoustic beam. While a single transducer cannot change its

characteristic beam, the waves generated by several transducers can be combined to create a specific beam pattern. Linear arrays can perform three basic beam operations: control of active aperture, focusing and steering (Figure 6) [46]. The active aperture is the number of elements that are actually vibrating within the array (Figure 6a), hence controlling it provides control over the beam base size. As is explained later in this chapter, the total array length has an important role in the signal to noise ratio and lateral resolution of the system [48].

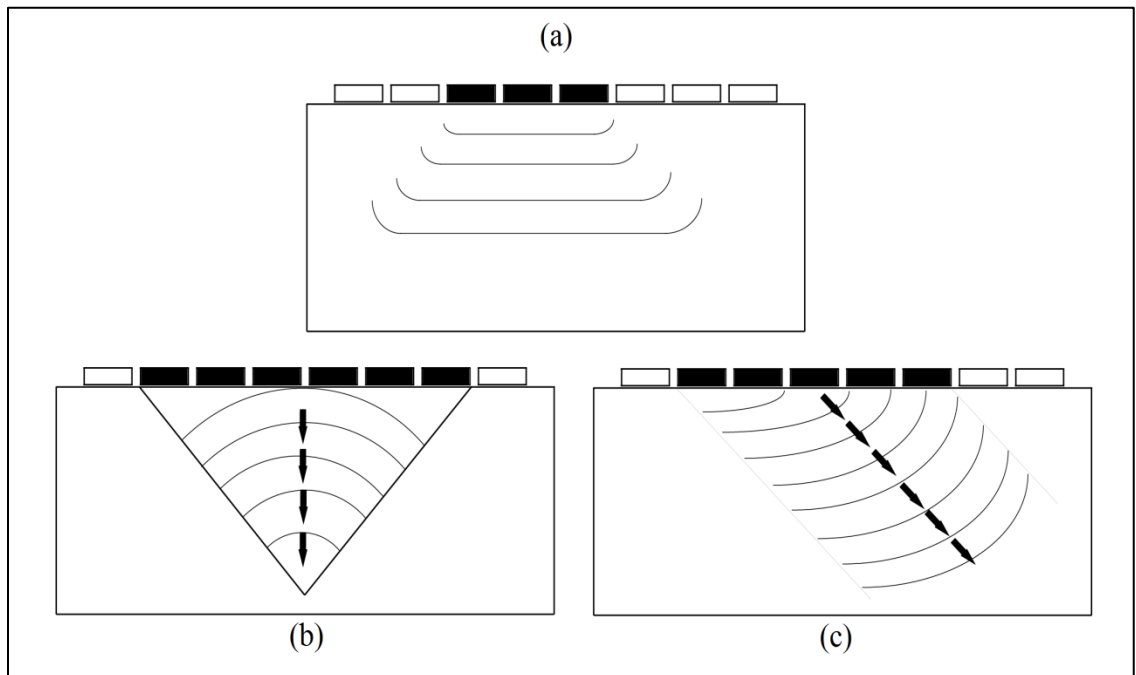


Figure 6. Linear arrays basic operations: (a) is active aperture, (b) focusing and (c) steering.

A PZT linear array can be focused to a specific location by choosing the moment in which some specific elements are activated, this operation is called focusing (Figure 7). The focal point of the array can be selected by applying the appropriate delays ( $\tau_i$ ) to the appropriate transducers. A common wave front is formed by the constructive and

destructive interferences of the waves created by the single elements. The wave front is a new beam focused into a desired location [49]. The following formulation shows the calculation procedure of the delay times [50]:

$$\tau_i = \frac{\sqrt{(x_i - x_f)^2 + (y_i - y_f)^2}}{c} - \frac{R_f}{c} \quad (17)$$

Where  $\tau_i$  is the delay time of the  $i^{\text{th}}$  element,  $x_i$  and  $y_i$  are the coordinates of the  $i^{\text{th}}$  element,  $x_f$  and  $y_f$  are the coordinates of the desired focal point,  $C$  is the speed of sound of the scanned material and  $R_f$  is the distance of the focal point to the array center.

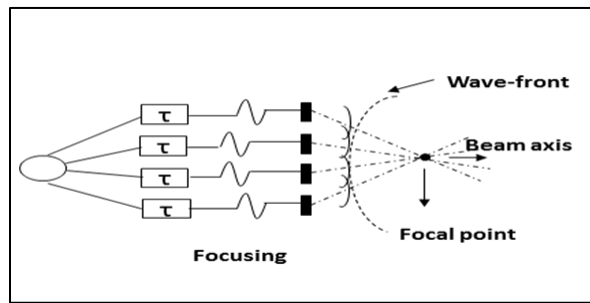


Figure 7. Schematic of linear array focusing.

Beam steering is also achieved by delaying the activation of some elements. The overall beam is rotated a desired angle (Figure 8). This increase the scanning capacity of the array, but it can also create undesired beams known as beam side lobes. The lobes are created by the interaction of out of phase waves generated by the array elements. A common strategy to avoid its creation is reducing the array pitch. In [49] it is explained that for a pitch smaller than  $\lambda/2$  the side lobes disappear.

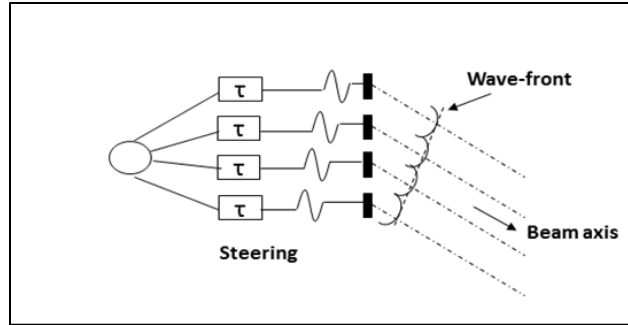


Figure 8. Schematic of linear array steering.

Linear array of PZT are applied from medical imaging to sonars. In reference [47] an application where linear arrays produce Lamb waves in thin plates to detect crack initiation and progression is presented. The array was also tested for imaging generating of fatigue cracks induced by variable loads exerted onto a thin plate. Bulk waves or guided waves can be used with this technique. In medical imaging the most common approach is bulk waves while in SHM, Lamb waves are selected due to its low attenuation and dissipation characteristics. More information about the actual beam models and imaging algorithms can be found in reference [49].

### **2.2.3.2 2-D Arrays**

Two dimensional arrays can be in square, rectangular, circular or cross-shaped shapes, Figure 9 illustrate some examples. The additional array dimension permits the creation of 3-D images of the tested material. Even though each of the array geometries has different capabilities in terms of acoustic beam shape, all of them permit the basic three operations. Furthermore all enable the generation of 3-D images. Additional information related the beam models of every array is found in references [46, 47, 49].

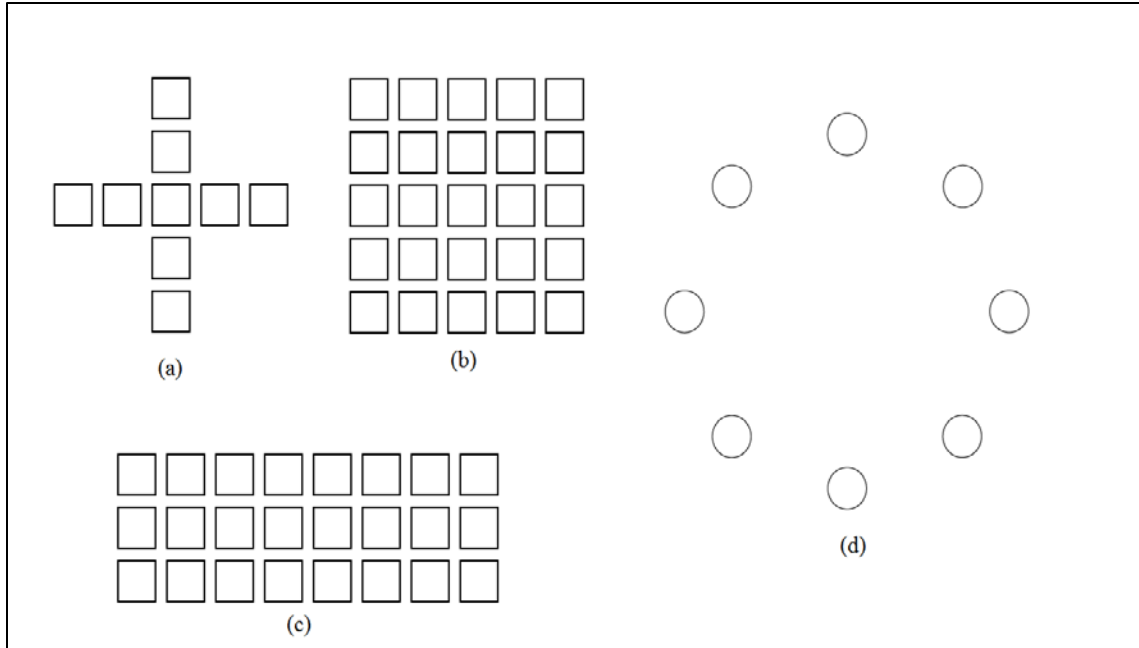


Figure 9. Schematics of 2-D arrays geometries: (a) Cross configuration, (b) Square configuration, (c) Rectangular configuration (a.k.a 1.5-D [46]) and (d) Circular configuration

Application of 2-D arrays can be found in medical imaging, sonars and SHM. In reference [47] several experiments for damage detection using different arrays are presented. The author also presents active aperture algorithms for the design of damage detection radars in thin plates. The main issue with 2-D arrays is the number of independent transmits-receive channels required for operation. The current technology allows up to 256 [46]. The number of channels represents the number of elements that can be active in the scanning process (active aperture), this obviously constrains the 2-D arrays hence they great quantity of element (per unit size) required.

#### **2.2.4 Ultrasonic Image Generation**

Critical structural problems can be detected with ultrasonic imaging. Corrosion, cracks or even missing bolts can be found with ultrasonic images. In this section two

methodologies used for image formation based in PZT arrays are presented. General principles of beam generation and image reconstruction are explained; the quality factors of an image system are defined and described.

An ultrasonic image, as the one illustrated in Figure 10, is a geometrical representation of the waves generated in a scanned object. The nature of the wave (Lamb, pressure, shear, etc.) does not change the way the representation is made: high amplitude waves are presented in a specific color and low amplitude in another. In the case of the Figure 10, white is high intensity and black low amplitude. In most imaging system the representation is based in the reflected waves created by the difference in acoustic impedance of the scanned media; the higher the difference, the higher intensity of the reflected wave.

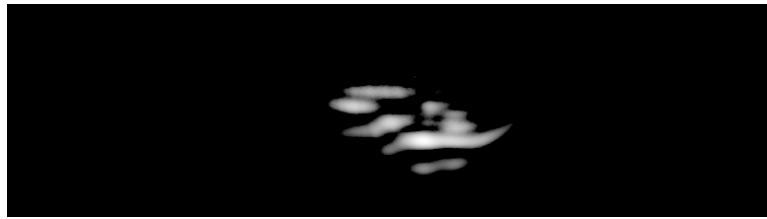


Figure 10. Example of an ultrasonic image.

The wave intensity is received by signal collector as a voltage value, so a strong acoustic impedance change is received by the collector as a bigger voltage peak. In summary, an acoustic image is a geometrical array where different voltage values, collected by PZT,

are displayed in congruent color scale with the goal of showing the differences in acoustic impedance present in the scanned material.

#### ***2.2.4.1 Phased Array Imaging***

This technique uses simultaneously all the array elements as transmitters and receivers. The goal is to produce a focused beam in a desired direction in order to increase the signal to noise ratio and therefore obtain higher resolution images [50, 51]. The main drawback of this approach is the high complexity in electronics, especially in arrays with large number of elements. It is necessary to have a large number of transmit and receive channels active at the same time during the image formation [50]. The successful application of this methodology in the medical field has led the researchers to explore applications in non-destructive testing. Some representative applications are presented in references [62-68].

By applying the appropriate delays to the array elements, the complete array beam is focused into a desired direction. Progressively the array focus direction is changed in order to scan a different line of the scanned area. This is 2-D polar scanning sequence, with the steering angle representing the angular coordinate.

The reflection signals are delayed, focused and added just as the generated signal were. This is not an electronic procedure like the case of generation which consist of delaying the input voltage, but an off line correction of the data that are added together. The same delay time ( $\tau_i$ ) used for focusing is now used to find the data point that correspond to

every specific image point (pixel). The reconstructed signals correspondents to a specific steering angle are calculated using the following expression [50]:

$$r_{\theta}(t) = \sum_{i=1}^N \sum_{j=1}^N w_j w_i s \left( t - \frac{R_f}{c} - \tau_j \right) \quad (18)$$

Where  $w_j$  is a weighting parameter, mostly used for attenuation adjustments,  $s_j(t)$  is the actual signal received by the  $j^{\text{th}}$  transducer,  $R_f$  is the distance from the reconstructed point to the array center,  $C$  is the sound speed velocity of the scanned material,  $\tau_j$  is the time delay correspondent to the  $j^{\text{th}}$  element,  $N$  is the total number of transducers and finally  $r_{\theta}(t)$  is reconstructed signal correspondent to the  $\theta$  angle.

The final step in the image formation is coordinate conversion and interpolation. The polar signal arrangement ( $r_{\theta}$ ) is converted to Cartesian coordinates:

$$r = \sqrt{x^2 + y^2} \quad \& \quad \theta = \arcsin\left(\frac{y}{x}\right) \quad (19)$$

Where  $x$  and  $y$  are the Cartesian coordinates of the desired pixel. In order to increase the number of data point which decrease the pixel size and therefore improve the image resolution, an interpolation is applied to the converted image [50].

#### ***2.2.4.2 Synthetic Phased Array Imaging***

The synthetic phased array reduces the complexity of the phased array by using only 1 element in transmitter-receiver mode. Two approaches can be used with this method: conventional synthetic aperture or synthetic phased array. In the conventional synthetic aperture, 1 transducer is mechanically manipulated in order to create the desired array. The transducer is transmitter and receiver in different positions. The synthetic phased array use a real array of transducer but in a particular time only one transducer acts as

transmitter and receiver. The others elements act as receivers only, this characteristic permit the increment of the image quality while significantly reducing the system complexity [50].

Contrary to the phased array approach, in the synthetic array methodology, the acoustic beam is not focused on a single point or direction. The beam is produced by a single element and therefore the beam focus is the natural focus of the transducer. The beam is expected to generate waves in all the scanned area and the reflection should be detected for the rest array elements. It is shown in Figure 11 that the transmitter-receiver mode is alternated within the elements, hence a complete scan only finish when all the elements have acted as transmitter and receiver [50, 52].

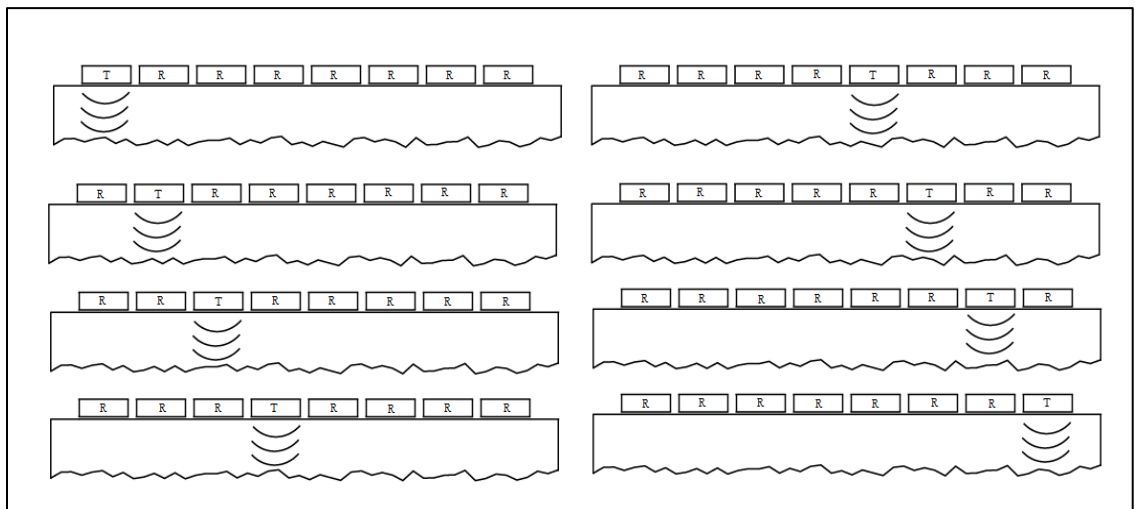


Figure 11. Schematic operation procedure of the synthetic phased array.

The image reconstruction is similar to the phased array approach. The reflection signals are focused with time delays. In this case the reconstructed signal is a 2-D sector image, hence all the transducer create an image of the scanned area when a particular transducer

is actuated. The images are then added in order to form the final picture. The signal can be reconstructed following the following formulation [53]:

$$r(x', y') = \sum_{j=1}^N w_j s_j \left( t_o + \frac{2}{c} \sqrt{(x' - x_j)^2 + y'^2} \right) \quad (20)$$

Where  $w_j$  is a weighting parameter, mostly used for attenuation adjustments,  $s_j(t)$  is the actual signal received by the  $j^{\text{th}}$  transducer,  $t_o$  is the time needed nullify the effects of the electronic devices,  $C$  is the sound speed velocity of the scanned material,  $x_j$  is the transversal position of the  $j^{\text{th}}$  array element,  $N$  is the total number of transducers and finally  $r_{x,y}$  is reconstructed value of the pixel with coordinates  $(x', y')$ . The initial signal  $s(t)$  may be interpolated for increasing the number of pixels in the image and therefore the image resolution.

Due to the inherent advantages of the synthetic aperture focusing, many studies have been performed in order to improve its efficiency and its applicability in strongly attenuative materials. In reference [54, 55, 56] some modified algorithms based in this methodology have shown improvement in the image quality in very difficult materials such as concrete and ferritic-austenitic stainless steel.

#### ***2.2.4.3 The Performance Criteria of an Imaging System***

Four basic parameters define the quality of an acoustic imaging system: Axial resolution, lateral resolution, contrast resolution and signal to noise ratio (SNR). The axial and lateral resolution are related to the capacity of the system to separate reflective boundaries along the longitudinal and transversal beam axis respectively. The axial resolution is improved by the generation of signals with long bandwidth. This is achieved

with high frequency transducer and short pulses. High frequency waves are affected more by the attenuation, so lower scanning penetration can be achieved. The axial resolution can be calculated as follows:

$$\Delta l = C \frac{t_p}{2} \quad (21)$$

Where  $l$  is a longitudinal distance,  $C$  the waves propagation velocity and  $t_p$  is the temporal pulse length.  $\Delta l$  represents the minimum change in longitudinal distance that can be measured by the imaging system.

The lateral resolution depends of the beam width, the wider the beam the less resolution. An image formed close to the beam focus has better resolution than another one formed in the far or near field [10]. Side lobes also reduce the lateral resolution due to of noise introduction to the system. The contrast resolution a.k.a dynamic range, is defined as the smallest change in acoustic impedance that the system is able to measure.

The dynamic range is presented in decibels units (dB). It represents the square logarithmic ratio between the maximum and minimum signal:

$$\Delta I(dB) = 20 \log \left( \frac{P_2}{P_1} \right) \quad (22)$$

The contrast resolution can be improved by reducing the side lobes levels and increasing the axial and lateral resolution [48]. The signal to noise ratio (SNR) is a method to measure the amount of information present in the signal relative to the ambient noise. Low levels of SNR means that the intensity of the reflected waves is comparable to ambient noise which cause low quality images. Alternatives to increase the SNR are the increment in the array element size and averaging the received signal.

## **CHAPTER 3: INSPECTION OF STEEL PLATES VIA ULTRASONIC ACOUSTIC WAVES**

### **3.1 Calculation of Surface Acoustic Wave Velocity in Steel 1018.**

A very important characteristic of the surface acoustic waves (SAW) is the constant wave velocity. The imaging reconstruction techniques take advantage of this fact to estimate the position of reflective boundaries within the scanned material. The application of accurate wave velocity values is necessary for a precise image reconstruction. Although there is an explicit formulation to obtain SAW velocity, the natural variation of the material properties involved in the formulation may potentially cause significant errors. In order to overcome this problem, the estimation of the SAW velocity in a 1018 steel plate is carried out in the following experiment. Additionally, the results are compared with the theoretical velocity founded in the published literature.

#### ***3.1.1 Experiment Configuration***

The SAW velocity is calculated by measuring the time of flight (TOF) of the waves reflected by the plate edge. The generation and reception of the SAW is conducted with a 5MHz and  $\frac{1}{2}$  in diameter transducer attached to a crystal wedge, a pulse generator (Olympus 5072PR) and an oscilloscope (Tektronix TDS 2024B). Detailed characteristics of the device are presented in Appendix A. Figure 12 shows a sketch of the wedge's initial position.

With the assistance of a manual micrometer, the crystal is positioned 3 inches from the edge of the plate. The nature of the system requires setting the pulse generator at a damping of  $50\Omega$  and pulse repetition frequency (PRF) of 200Hz and the received signal amplification to 40dB.

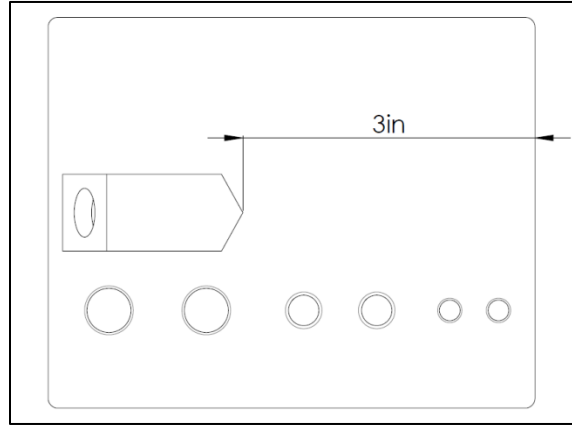


Figure 12. Schematic of the initial position of the wedge.

### **3.1.2 Procedure**

Initially, the wedge with the transducer attached should be positioned at the point illustrated in Figure 12. After the wedge is correctly positioned, the signal acquired is recorded by the oscilloscope. No further data recording is required due to the high accuracy of the oscilloscope. This recorded signal will be used to calculate the SAW velocity.

### **3.1.2 Experimental Results**

Figure 13 illustrates an example of the acquired signal with the experimental setup discussed above. There are three clear signal peaks resulted from the interaction with three different objects. The first peak is caused by the electrical equipment interference.

The second peak represents the reflection from the crystal wedge, which is the first medium excited by the transducer. The third peak is the reflection from the plate edge.

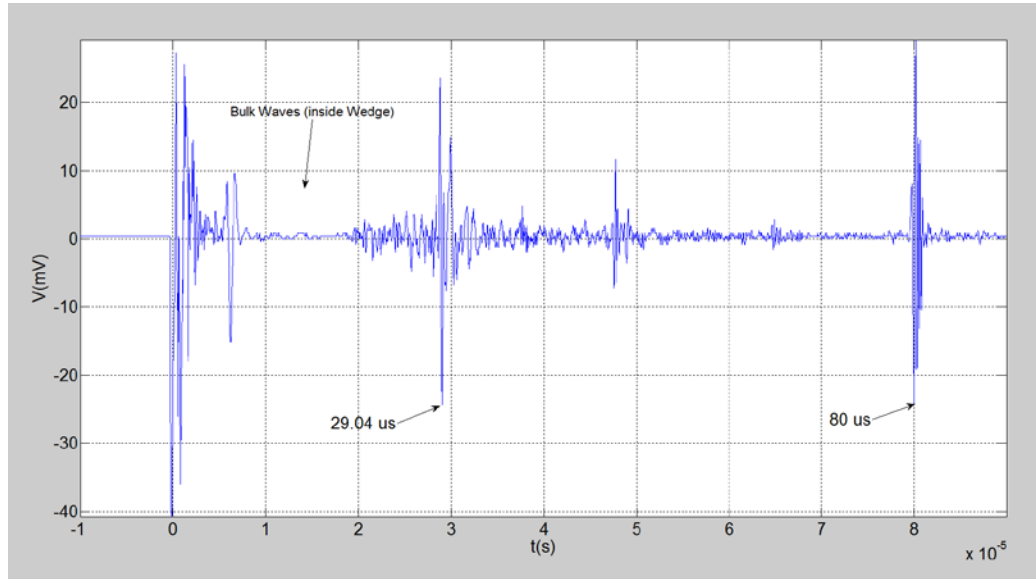


Figure 13. Signal obtained from the reflected SAW generated in the 1018 steel plate.

The time correspondent to the maximum intensities of the second and third peaks should be subtracted in order to find the time used by the SAW to propagate from the wedge, hit the boundary and then propagate back to the transducer. The obtained time information should be divided by two since the SAW travel twice the separation distance:

$$C_R = \frac{l}{2t} \quad (23)$$

$$C_R = \frac{3 \times 2.54 \div 100}{50.96 \mu s \div 2} = 2990.6 \frac{m}{s} \quad (26)$$

$$t = 80 - 29.04 = 50.96 \mu s \quad (24)$$

$$C_{R,T} = 2953 \frac{m}{s} \quad (27)$$

$$l = 3 \text{ inch} \quad (25)$$

$$Error = \frac{C_{R,T} - C_R}{C_{R,T}} \% = 1.2\% \quad (28)$$

Where  $C_R$  represents the surface wave velocity,  $C_{R,T}$  is the theoretical surface wave velocity calculated with the formula illustrated in section 1.1.1.3,  $t$  is the time used by the SAW to go through the plate and go back to the transducer, and  $l$  is the distance from the crystal wedge to the plate edge. The difference of the velocity found with the experiment and the velocity calculated is very small (1.2%), which means that the acoustic properties of the 1018 steel plate agree with values found in the literature [57].

### **3.2 Calculation of SAW Attenuation Coefficients in Steel 1018**

A simple experiment is performed in order to calculate the exponential attenuation coefficient of the propagating SAWs [10, 58]. The attenuation lead to intensity diminution of the received signal, therefore characterization of flaws based in the signal intensity can turn to be difficult if the attenuation is not taken into account. The following experiment shows a method to find the attenuation coefficient of SAW in a 1018 steel plate.

#### ***3.2.1 Experiment Configuration***

Diminution in the signal intensity due to increment of the wave time of flight (TOF) is used to calculate the attenuation coefficient of SAW. The generation SAW is achieved through a 5MHz transducer attached to a crystal wedge and a pulse generator. Additionally the transducer-wedge configuration is connected to a translation stage with the help of specially designed aluminum parts. The SAW are sent in direction of the right plate edge (Figure 14) in order to catch the wave reflections and save its intensity, the TOF is increased by changing the wedge separation from the plate edge. An oscilloscope

is used to calculate the peak-to-peak value of the received signal; all the specific information about the equipment is presented in Appendix A.

### ***3.2.2 Procedure***

The initial position of the wedge is shown in Figure 14. Using the translation stage the wedge should be move 0.1in towards the plate edge. Prior to any further movement the peak-to-peak value of the received signal should be saved. The oscilloscope scale set so that the peak generated by the electrical devices does not influence the peak-to-peak calculation. Failure to do so may results in a peak-to-peak intensity correspondent to the electrical interference. Another important consideration is to maintain the SAW path towards the plate edge free of acoustic coupling, liquids in contact with plate surfaces attenuate the incoming SAW due to losses in form of compressional waves [8], so leaving traces of couplant between the wedge and the plate edge generates attenuation that is independent from the steel plate.

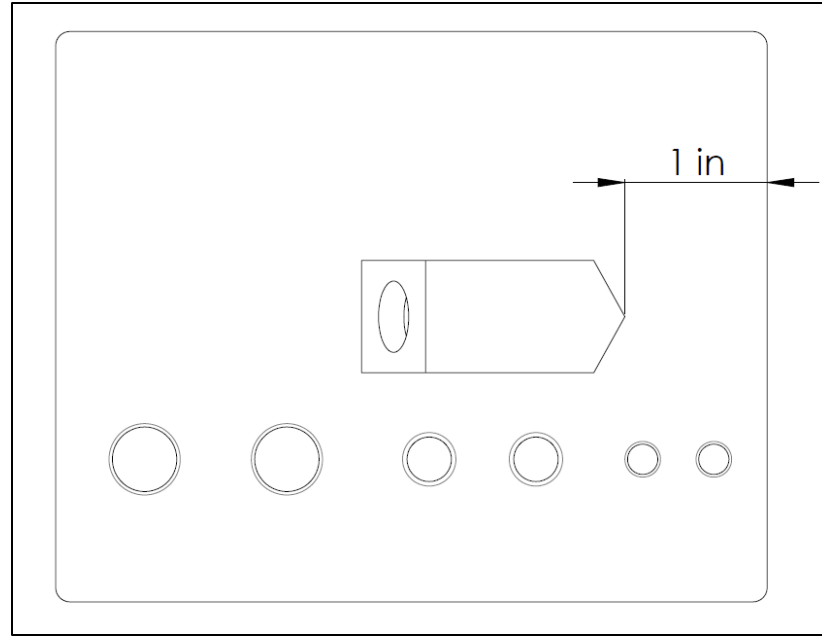


Figure 14. Drawing of initial position of wedge.

### ***3.3.3 Experimental Results***

The peak-to-peak values versus wedge position are plotted in Figure 15. An exponential approximation to the curve is also shown. The Figure 15 presents clearly the exponential behavior of the attenuation factor, it shows an R-squared error of 0.99 for an attenuation value of  $\alpha = -0.548$  Np/in.

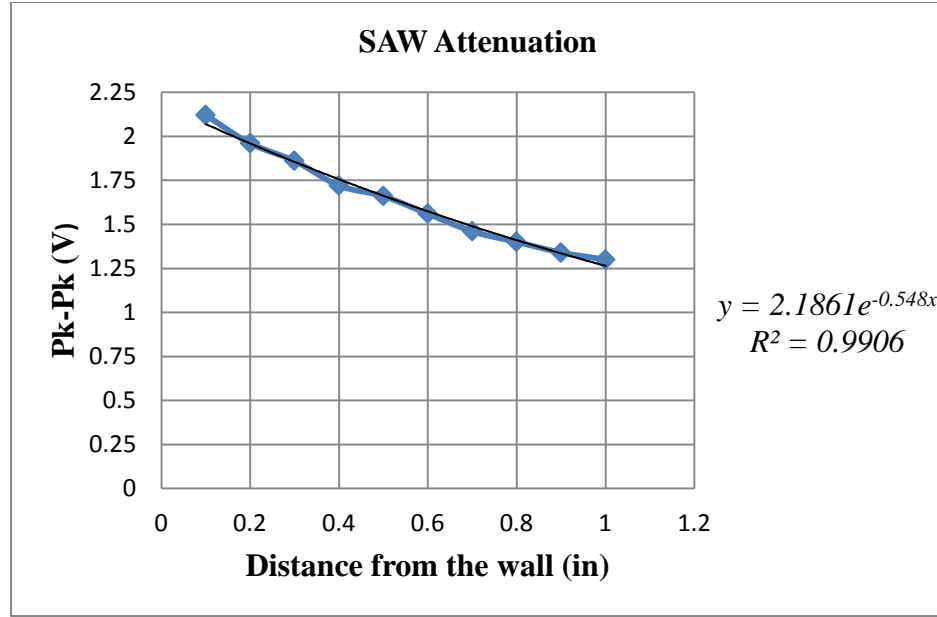


Figure 15. Plot of the intensity measurements versus the wedge position. The trend line of the curve is shown in the right.

The attenuation calculated directly from the chart does not take into account that the signal travel twice the distance plotted, so the attenuation factor should be divided by 2:

$$2z = x \rightarrow y = 2.1861e^{-0.548\frac{z}{2}} \leftrightarrow y = 2.1861e^{-0.274z} \quad (29)$$

$$\alpha_{SAW\ 1018\ steel} = -0.274\ Np/in \quad (30)$$

### 3.3 Estimation of Flaws Position using a Conventional Synthetic Aperture (SA) System

A very powerful strategy used in nondestructive testing is the image generation [59, 45, 44]. In this study, bulk waves are used to create images of a steel plate. Bulk waves induced by piezoelectric transducers (PZT) are created inside a 1018 steel plate with machined holes that act as flaws in the metal (Figure 16). The wave reflections are used to calculate size and position of reflective boundaries in the plate e.g. plate edges and holes. The conventional synthetic phased array imaging technique is employed; it

consists of a virtual manipulation of the signals received and generated by a single transducer actuated from different locations [50]. In this experiment the accuracy of the technique will be tested with the purpose of finding its suitability in further applications. In this research an acoustic couplant that follows the standard ASTM F945 is employed.

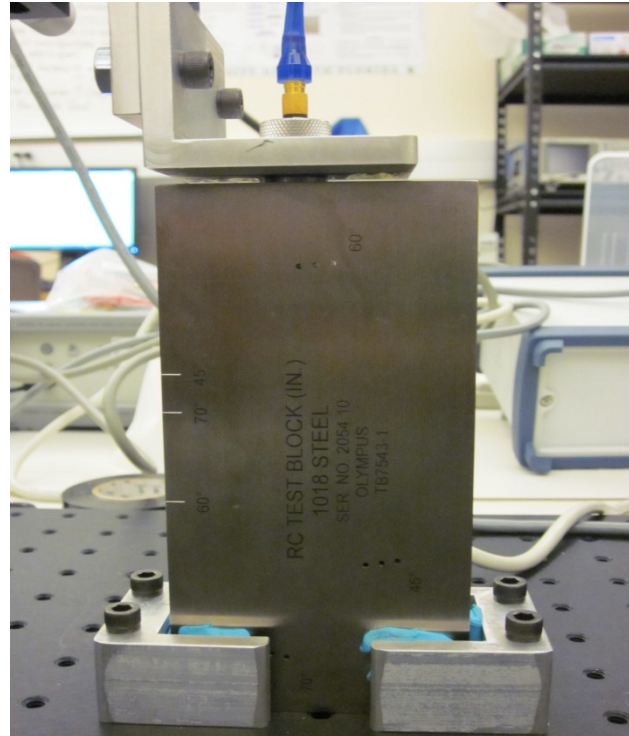


Figure 16. Photo of the bulk waves experiment configuration.

### **3.3.1 Experiment Design**

The synthetic array design consists of two parameters: the number of elements in the array and the distance between the members (pitch). The array pitch is inversely related to the lateral resolution of the imaging system [50], normally it is selected as some specific fraction of the wavelength ( $\lambda$ ), which depends of the bulk wave velocity and the transducer frequency. The wave frequency (transducer central frequency) is also related to the axial resolution of the imaging system [48], hence high resolution images required

high frequency elements and small pitch arrays. Therefore, in this experiment the highest frequency transducer available in the facilities (5MHz) is selected. The array pitch ( $p$ ) is chosen to be  $\lambda/4$ :

$$p = \lambda/4 = \frac{V_{\text{Bulk}}}{4f} = \frac{\sqrt{\frac{E}{\rho} \left( \frac{1+\nu}{1-2\nu} \right)}}{4f} \quad (31)$$

$$p = \frac{\sqrt{\frac{205Gpa}{7870kg/m^2} \left( \frac{1+0.29}{1-2 \times 0.29} \right)}}{4 \times 5MHz} \quad (32)$$

$$p \approx 0.01in \quad (33)$$

Where  $f$  is the transducer center frequency,  $E$ ,  $\nu$ ,  $\rho$  are the elasticity modulus, the Poisson's ratio and the density of the 1018 steel, respectively. Properties were taken from [57].

The number of elements in the array (NE) determines the array aperture (length) which is proportional to the lateral resolution, therefore high number of elements increases the resolution, at a cost of increasing scanning time, so a balance between image quality and experiment duration should be determined. In this study, it was decided to create and array of 55 elements, so the array has an active aperture of 0.55in.

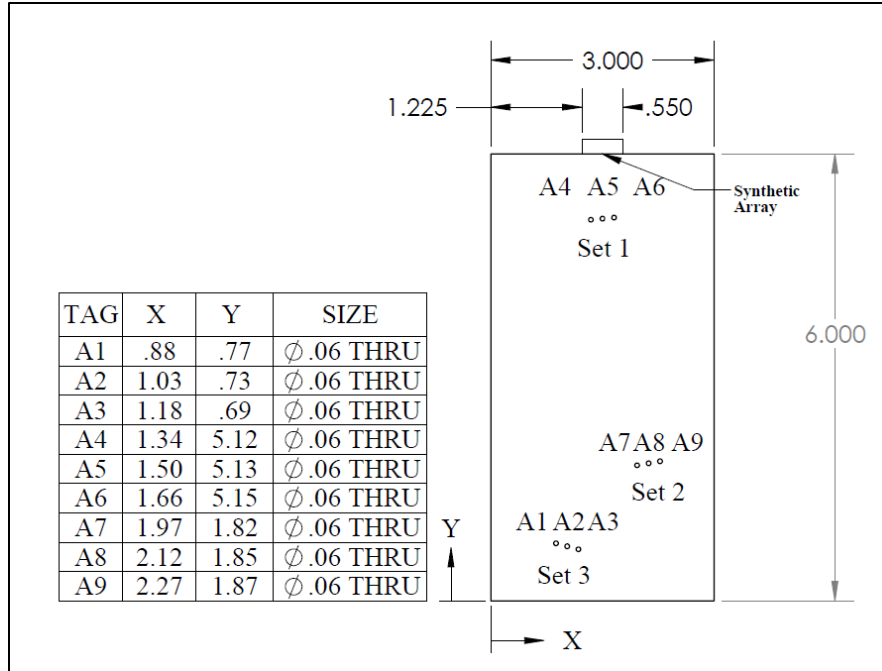


Figure 17. Schematic configuration of the bulk wave experiments. A blueprint of the steel block where the position of the holes, the dimensions and the position of the transducer array is presented. The table shows the diameter and position in X and Y coordinates of the holes in the steel block.

### 3.3.1 Experiment Configuration

A synthetic phased array is created with help of a translator stage (TS). The 1018 steel plate is secured to the workbench using specially design aluminum clamps. A second set of aluminum parts connects the transducer to the translator stage and allows the free movement of both components. In Figure 16 and Figure 17 a real and schematic view of the configuration is shown. Figure 17 also illustrates the exact position of the machinated holes and the area that corresponds to the array. Appendix A contains a datasheet of the devices used in this test.

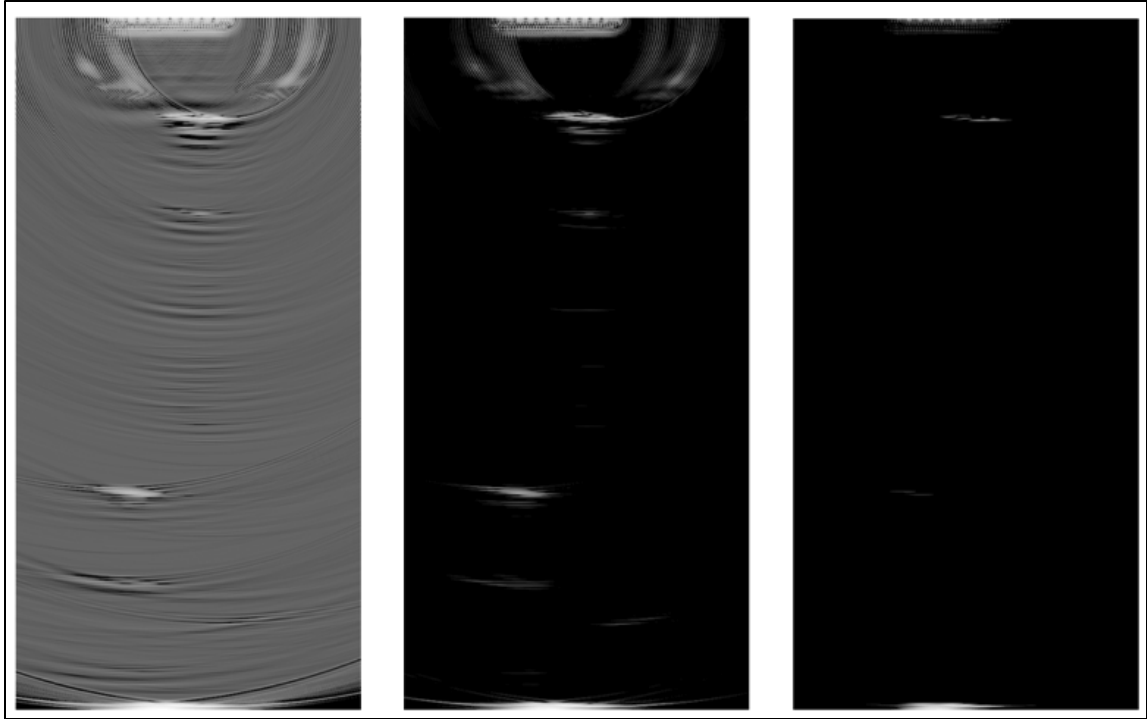
### 3.3.1.1 Experimental Procedure

1. The steel plate should be positioned in a place that allows to the translation stage to reach it. The aluminum clamps should lock the steel plate in the position shown in Figure 16.
2. The wedge-transducer assembly should be secured to the TS with help of the Aluminum L and aluminum plate. The height of this assembly must permit the contact between the transducer base and the plate surface. Acoustic couplant must be applied prior any contact as the acoustic impedance mismatch between the transducer crystal and the steel may prevent the transmission of waves.
3. The TS is employed to position the wedge as is shown in Figure 17 ( $y=6\text{in}$ ,  $x=1.225\text{in}$ ). It is very helpful to use the steel plate edges as reference. The movement span of the TS is only one inch, so the configuration process should take into account that the wedge needs to move 0.55in after initially installed.
4. The oscilloscope and the pulse generator should be turned on. The signal gain must be set around a value in the range of 20's or 30's. The correct configuration of the oscilloscope allows the edge reflection to be observed. The highest peak should be at least half of the oscilloscope scale.

5. In order to start the recording process, the signal should be set to average, this helps to increase the signal to noise ratio of the system. After recording the signal at the initial point, the transducer should be moved 0.01in to the right; prior to recording the second response, the average function should be reset. This procedure is repeated until 55 data points are collected.

### ***3.3.2 Experimental Results***

Longitudinal and transversal images of the steel block are the results of this experiment. Figure 18 shows full longitudinal images (B-scan) of the steel block, the images are presented with three dynamic ranges: 10dB, 20dB, 30dB. Higher decibels include reflections with lower intensity values, which cause images with more details but more prone to the noise. Images with lower decibels reduce the influence of noise information but it reduces the perception of signal with lower intensities, as is the case of the deepest hole set in Figure 18c [50].



(a) 30dB

(b) 20dB

(c) 10dB

Figure 18. Longitudinal images of a 1018 steel plate generated by synthetic phased array using bulk waves. Presentation with dynamic range of: (a) 30dB, (b) 20dB and (c) 10dB.

Figure 19 illustrates the full longitudinal images of the plate and also closer view of the holes for improved details. As expected, the image quality is deteriorated with increased depth. For instance, the first hole set appears sharp and with some details while the third hole set register almost no trace of the original geometry. This deterioration is a result of the low intensity signal received from the deeper holes consequence of the attenuation.

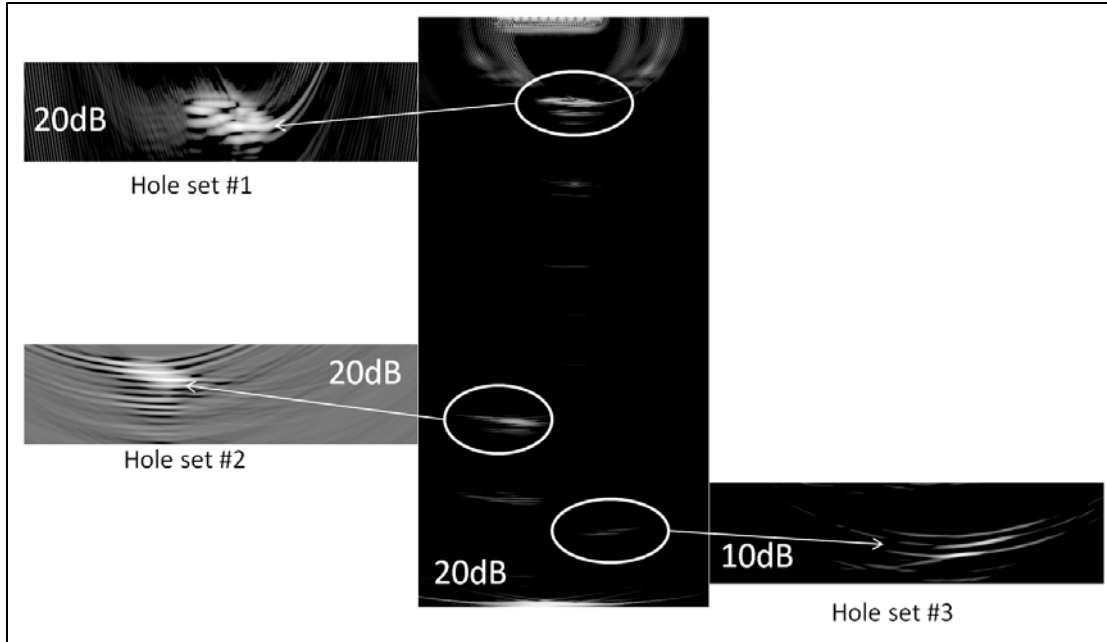


Figure 19. Longitudinal images of a 1018 steel plate showing enlarged details. The images created with the synthetic phased array imaging technique.

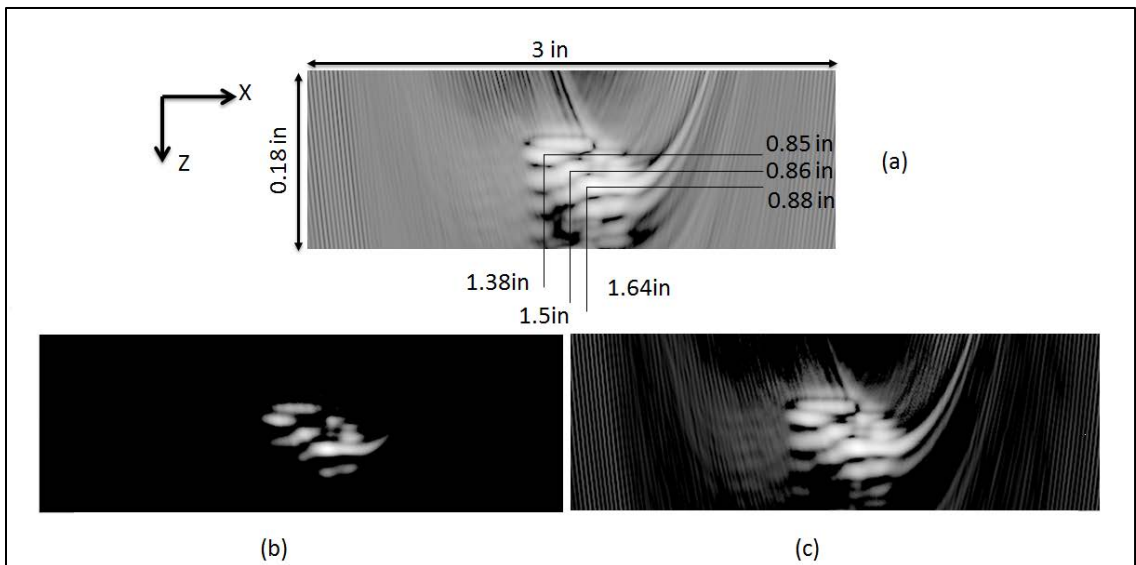


Figure 20. Enlarged longitudinal image of the first hole set. The estimated position of the holes is shown in (a). Dynamic range applied to (a) 30dB, (b) 10dB and (c) 20dB.

The position of the machined holes in the plate can be estimated through the images by finding the points of higher intensity. In Figure 20 the results of the first hole set are

presented. Once more three dynamic ranges are shown: 30dB, 10dB and 20dB. At this depth (0.85 in) the images show the holes with an elliptical shape, this effect is caused by disparities of the axial and lateral resolution (one dimension appears to be larger than the other one).

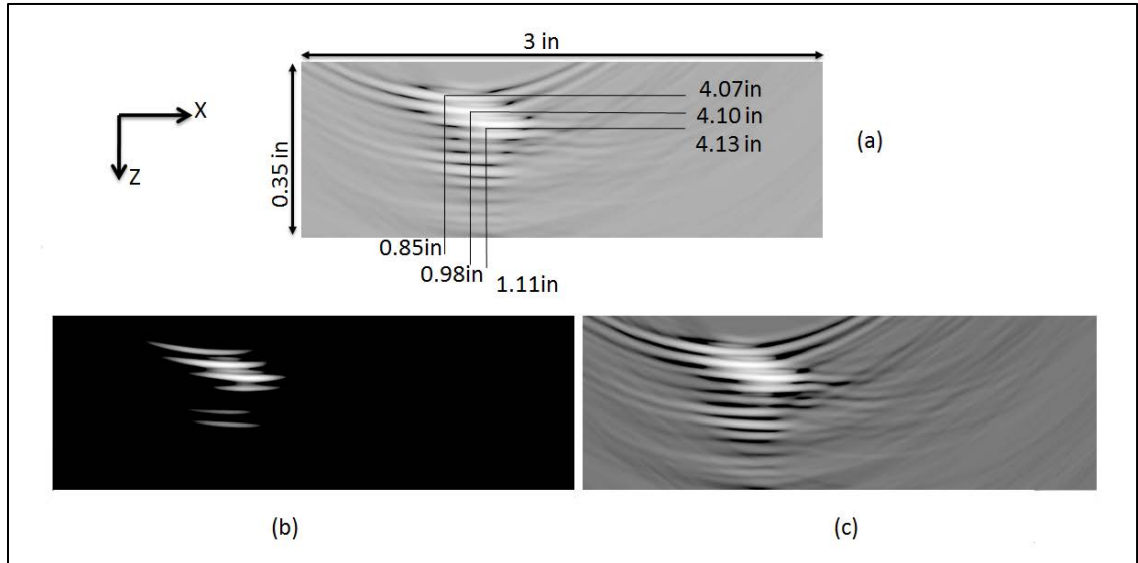


Figure 21. Enlarged longitudinal image of the second hole set. The estimated position of the holes is shown in (a). Dynamic range applied to (a)30dB, (b)10dB and (c) 20dB.

Details of the second hole set are shown in Figure 21, the position of the holes is also extracted from these images. Three different intensity levels are presented: 30dB, 20dB and 10dB. At 4 in depth, the image resolution deterioration is observable. In Figure 21b, no trace of the circular shape of the holes can be inferred. Even though the lateral resolution is very low, the image allows identification of the three holes, hence the axial resolution of the image is still acceptable.

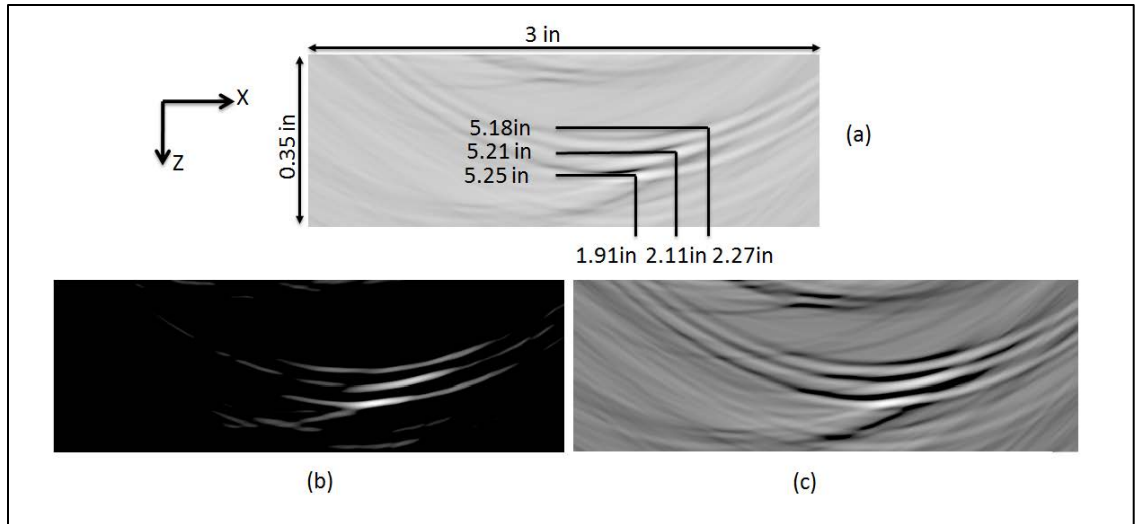


Figure 22. Enlarged longitudinal image of the third hole set. The estimated position of the holes is shown in a). Dynamic range applied to (a) 30dB, (b) 10dB and (c) 20dB.

A closer view of the third hole set is presented in Figure 22, presentations with dynamic range of 30 dB, 10dB and 20dB correspond to Figure 22 a, b and c respectively. The images in this case present characteristics similar to the previous cases. The holes are shown with almost flat boundaries with large size but the existence of three holes can still be detected.

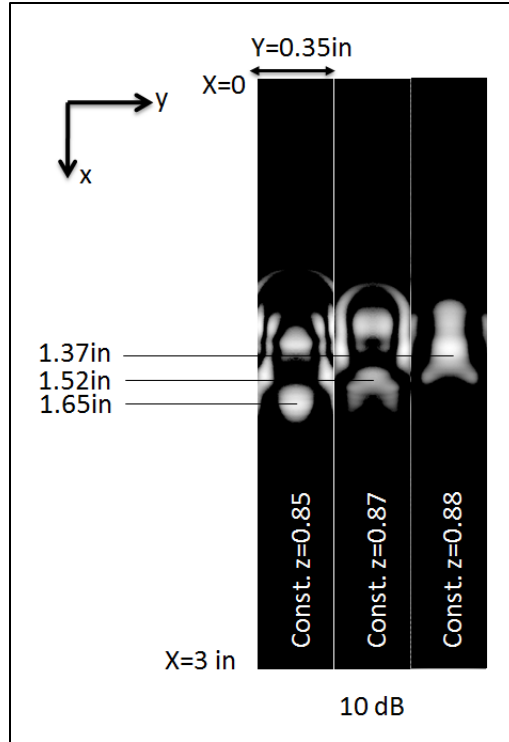


Figure 23. Transversal view of the first hole set. The transversal position ( $x$ ) of every hole is shown.

The circular shape of the transducer allows the reconstruction of transversal images of the steel plate (c-scan). The images are constructed for the holes depths ( $z$ ) estimated in the b-scans. Figure 23, Figure 24, Figure 25 illustrates the c-scan of the first, second and third hole set, respectively. From these images, the real shape of the flaws can be clearly observed, the diameter of the holes is measured from these images using the image pixels as scale.

The resolution variation with the depth of the transversal images is similar to the b-scans resolution, the closer set reconstruction shows a sharp circular shape while the second and third sets show very blurry results. The axial resolution in these images does not play any role because the images are reconstructed at constant depth values.

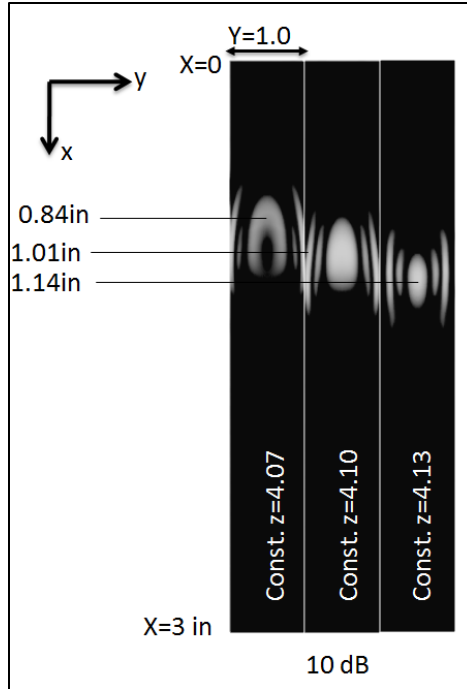


Figure 24. Transversal view of the second hole set. The transversal position (x) of every hole is shown.

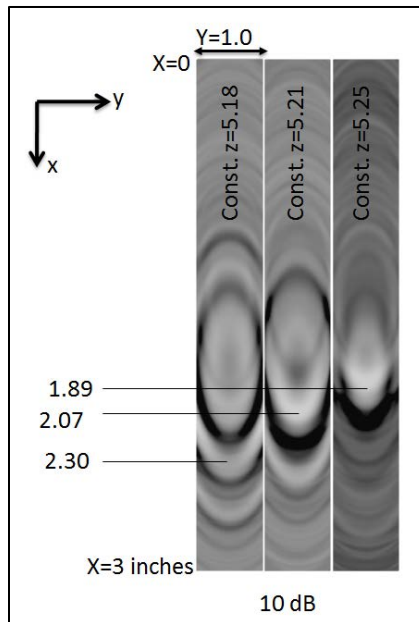


Figure 25. Transversal view of the third hole set. The transversal position (x) of every hole is shown.

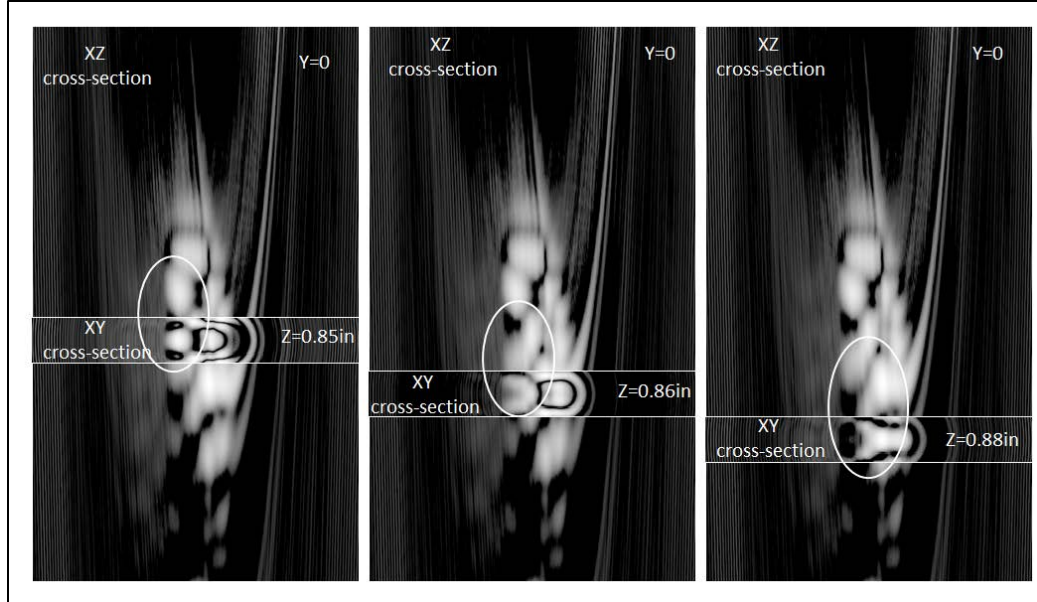


Figure 26. Combination of longitudinal and transversal images of a 1018 steel plate using synthetic phased array imaging technique.

The final image, Figure 26, shows a combination of a b-scan and c-scan for the first hole set. These combination present very precise details of the holes, diameter and position can be clearly identified. A comparison between the position obtained from the images and the real hole position is summarized in Table 2. In general the errors obtained are below 7%, but as expected higher errors are obtained in the transversal position estimation due to the lower lateral resolution. In addition the horizontal position of the holes is calculated relative to the array position, hence some error can be attributed to the initial array positioning.

Table 2. Real and obtained positions of the machined holes.

	X position (in) (Exp/Real)	Y position (in) (Exp/Real)
Hole Set #1	1.38/1.34	0.85/0.85
	1.5/1.55	0.86/0.869
	1.65/1.66	0.88/0.884
Hole Set #2	0.85/0.727	4.07/4.127
	0.98/0.880	4.10/4.154
	1.11/1.035	4.13/4.180
Hole Set #3	1.91/1.823	5.18/5.31
	2.11/1.974	5.21/5.27
	2.27/2.124	5.25/5.23

The error associated with the longitudinal position (y) does not have any influence from the array position. The errors in the longitudinal position error are summarized in Table 3. It is noticeable that the maximum error is only 2.45% within a depth of five inches. At the closer hole locations, the errors are much lower, inaccuracies of 0.02cm and less are found. The second hole set has errors of less than 1.5%, which is less than 0.15cm of disparity, so the imaging system shows a high longitudinal resolution even at big depths.

Table 3. Error associated with the longitudinal position estimation based in the acoustic images.

	y position Error(in)	y position error (cm)	y position Error(%)
Hole Set #1	0	0.00	0.00%
	0.009	0.02	1.03%
	0.004	0.01	0.45%
Hole Set #2	0.057	0.14	1.38%
	0.054	0.14	1.30%
	0.05	0.13	1.20%
Hole Set #3	0.13	0.33	2.45%
	0.06	0.15	1.14%
	0.02	0.05	0.38%

### 3.4 Chapter Review and Conclusions

In section 3.1 an experimental setup for SAW velocity calculation is presented and explained. The waves are created in a 1018 steel plate that is used in future experiments; the estimated velocity is compared with the theoretical value calculated with the classical SAW velocity formulation [60]. The difference in the estimated and calculated velocity is so small (1.2%) that either of those can be used for future experimentation with minimal error. The section 3.2 also presents a methodology for estimation of an important acoustic material property of the 1018 steel plate: the attenuation coefficient. A series of SAW reflections acquired at different positions help to measure the intensity changes of the waves while they propagate through the plate. The experiment results confirm the

exponential behavior of the wave attenuation and deliver the attenuation coefficient, parameter that is used in the experiments presented in chapter 4.

Finally in section 3.3, the conventional synthetic array imaging technique is tested. Estimation of artificial flaws in a 1018 steel plate is performed through a 5MHz transducer with 1/2in of circular aperture and a synthetic array of 55 elements and 0.1in of elementary pitch. While at depths of 0.85in the reconstructed images still show acceptable resolution, at depths superior to 4in the attenuation and diffraction deteriorates the lateral resolution of the images significantly. Although the attenuation also affects the longitudinal resolution, the effect of it is less severe; at depths up to 4in the position error is inferior to 1.5% while at 5in the error increases to around 2.5%. This imaging system has proved to have good accuracy in the estimation of the longitudinal position of small objects at different depths, hence it can be employed in the experiments of Chapter 4

## CHAPTER 4: BOLT TENSION ESTIMATION USING SURFACE ACOUSTIC WAVES

### WAVES

#### 4.1 Conceptual Framework

A novel methodology for detection of tension in bolted joints using surface acoustic waves (SAW) is presented. Surface acoustic waves are used to estimate changes in the area of real contact created in-between the bolt head and the clamped elements. As it was explained in chapter 1, the increment of the bolt tension creates an expansion of the real area of contact (RAC), hence estimation of changes in the RAC lead to assessment of the bolt tension. In Figure 27 a schematic presentation of the method can be observed. A crystal wedge is used to generate SAW in a metal plate towards a previously tensioned 1/4 inch bolt.

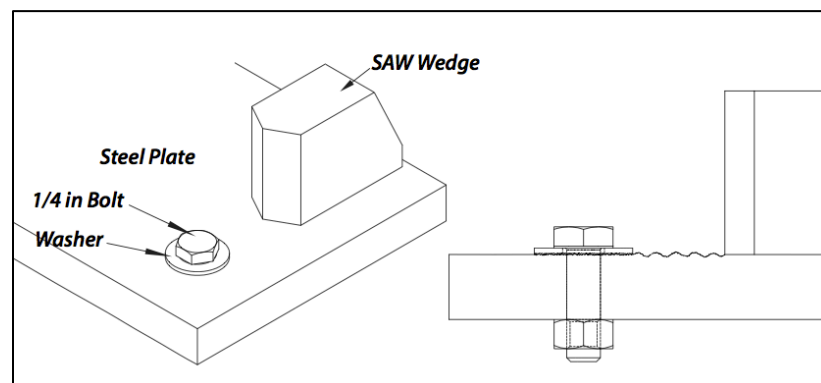


Figure 27. Schematic set up of the proposed methodology.

As it was explained in Section 1.1.1.3, the SAW can interact with elements in the surface of the propagation material (PM). The interaction with a solid, like is the case of the washer, take place in the points where the propagating surface and the external body are directly in contact with each other.

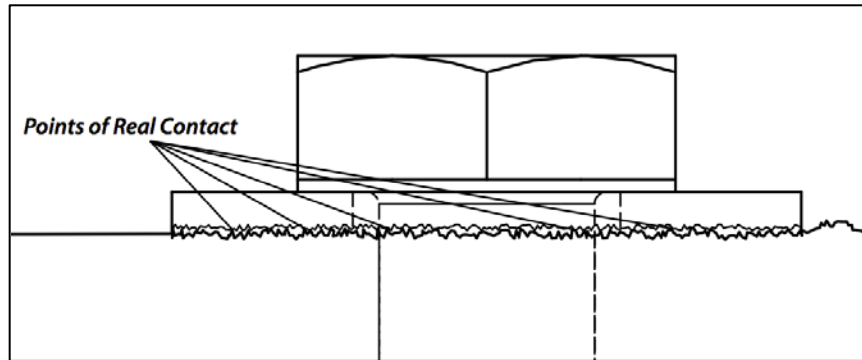


Figure 28. Enlarged representation of the real contact surface of the clamped plate and washer.

As illustrated in the Figure 28, the points of real contact correspond to small areas where the tips of the surface peaks in both materials makes direct contact with each other. The sum of these areas is known as the RAC. The existence of discrete points of contact between two rough surfaces means that incident SAWs propagating below a solid object will interact with an undefined number solid-solid and solid-gas (air) boundaries.

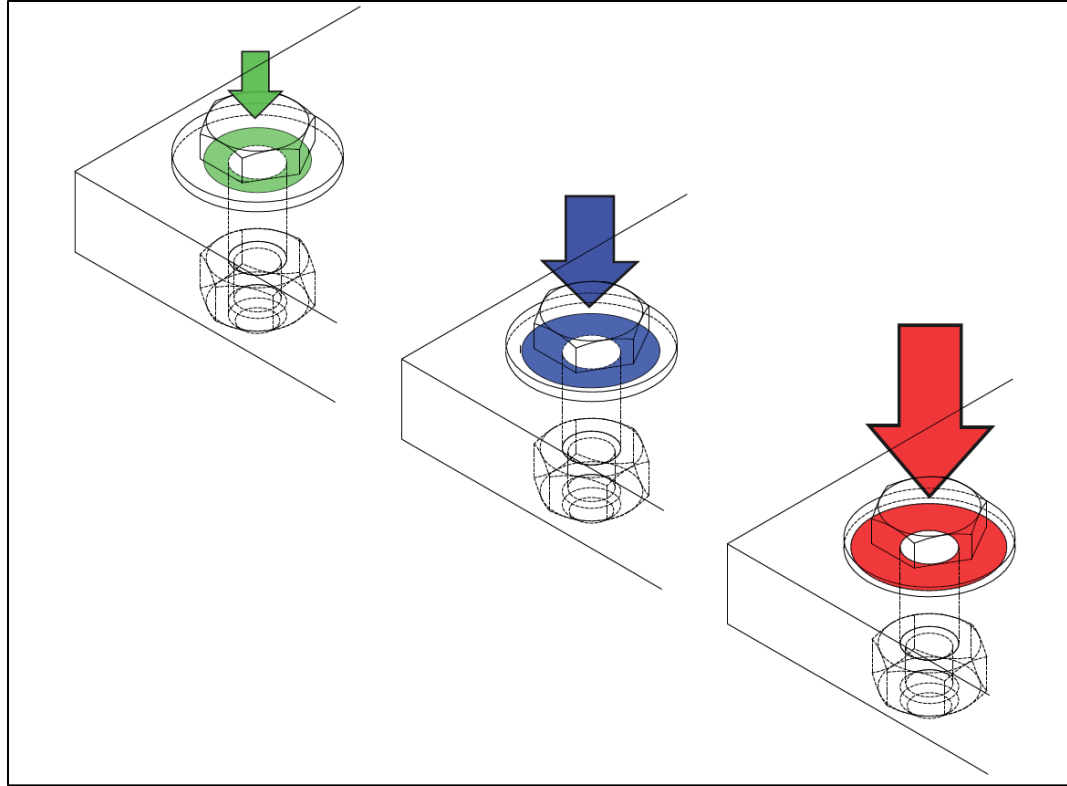


Figure 29. Schematic representation of change in the RAC due to tension increments.

Increasing the tension in the bolt raises the number and the size of reflection points (points of contact). Figure 29 illustrates a schematic representation of the RAC growth due to increments in bolt tension. The RAC is different from the apparent area of contact, but at high tension levels the difference between those is minimal [61]. The saturation of the RAC at some preload level establishes the maximum tension level that can be measured with the investigated concept.

The way in which the RAC expands is of special interest for tension estimation. The RAC grows from the washer center to the washer perimeter, as illustrated in Figure 29. This behavior can be explained by analyzing the way in which the tension is applied to the bolt head: the preload transforms into a pulling force exerted in the head center, hence

the surface peaks closer to it are expected to be more affected than the ones in the perimeter and therefore a radial expansion of the RAC can be predicted. This growth trend means that SAW face an acoustic wall that approaches to wedge as the preload is increased.

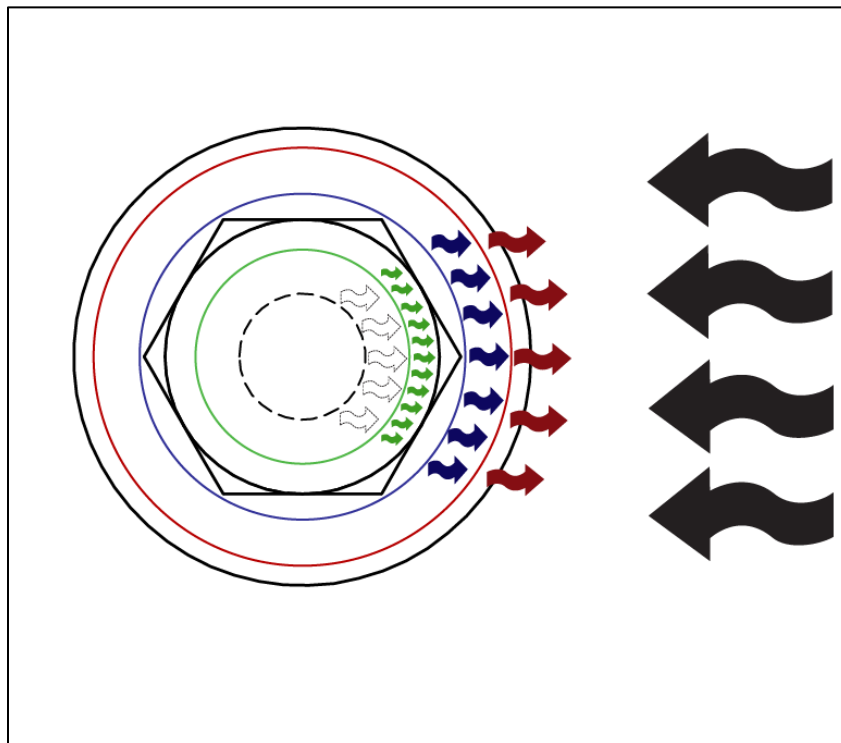


Figure 30. Representation of SAW reflection from 4 different boundaries. White arrows represent no load, green arrows low load, blue arrows medium load and red arrows high load. The black arrows represent the incoming SAW.

The change in position of the acoustic wall denotes a change in the tension applied to the bolt head. An acoustic wall is a series of the points where free movement of the waves is constrained e.g. the contact points of two solid objects. Material discontinuities, holes and object edges also behave as acoustic walls. In Figure 30 a schematic representation of the SAW reflection from different acoustics barriers is illustrated. The colored arrows denote the main reflection of the incoming SAW (black arrows). The RAC find its minimum

value when the bolt has no tension, in this case the main reflections come from the plate hole (white arrows). As the load is increased and the RAC grows, the main reflections move from the hole boundary and get closer to the washer perimeter. Figure 30 illustrates the reflection of 4 different states, no load (white), low load (green), medium load (blue) and high load (red). The changes in position of the acoustic wall are represented by a delay in the received wave, which means that every preload value has a related wall position represented by a specific time of flight (TOF) of the reflected waves. A relationship TOF vs. bolt tension can be generated.

In the following experiments the explained concept is tested. A plate of steel is used as the propagating material, bolts of 1/4in and 1/2 in are tensioned with different torque levels and the changes in the RAC are monitored. The RAC changes are inspected with the conventional synthetic phased array imaging technique. The images permit to establish the exact position of the acoustic wall created by the contact of the bolt head and the plate surface.

#### **4.2 Tension Evaluation of a 1/4in Stainless Steel Bolt**

In this study the proposed methodology is tested with a stainless steel bolt of 1/4in diameter installed in a 1018 steel plate. As the RAC growth affects the position of the SAW main reflections, it is necessary to establish very precisely where those reflections take place. In chapter 3 a synthetic phased array imaging method is used to find the location of very small holes in a steel plate. The reconstructed images presented very good longitudinal resolution, consequently the same imaging system is used in the experiments of this chapter.

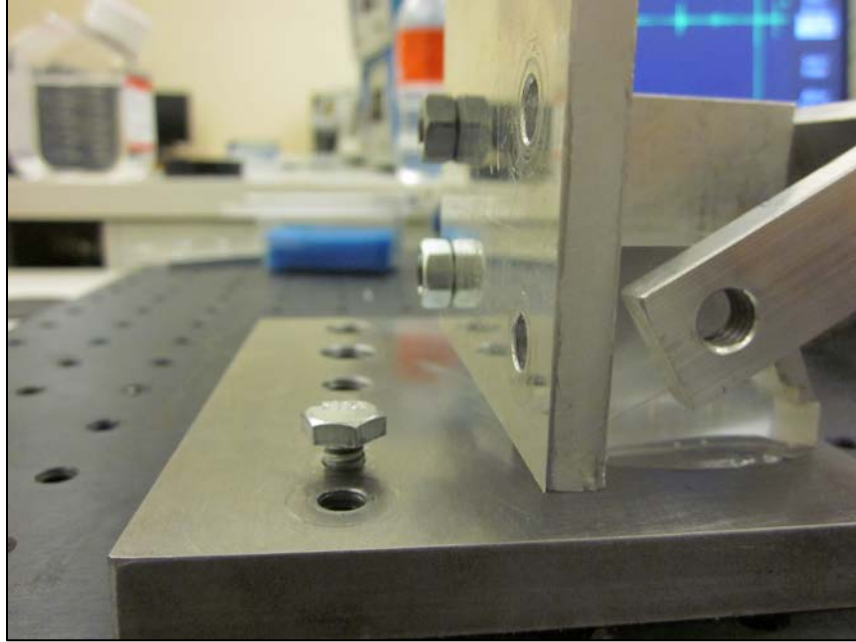


Figure 31. Photo of 1/4 inch stainless steel bolt tension evaluation.

#### 4.2.1 Experiment Design

A synthetic phased array (SPA) is employed in the following experiments. A transducer with central frequency of 5MHz, diameter of 0.5in and an array pitch ( $p$ ) of approximately  $\frac{1}{4}$  of the wave length ( $\lambda/4$ ) is selected aiming for high longitudinal resolution. The longitudinal position of the acoustic wall is used to characterize the RAC changes, necessitating high longitudinal resolution. The elementary pitch is calculated as follows:

$$p = \lambda/4 = \frac{V_{SAW}}{4f} = \frac{\sqrt{\frac{G}{\rho} \left( \frac{0.87+1.12\nu}{1+\nu} \right)}}{4f} \quad (34)$$

$$p = \frac{\sqrt{\frac{80Gpa}{7870kg/m^2} \left( \frac{0.87+1.12 \times 0.29}{1+0.29} \right)}}{4 \times 5MHz} \quad (35)$$

$$p \approx 0.01in \quad (36)$$

Where  $f$  is the transducer center frequency,  $G$ ,  $\nu$ ,  $\rho$  are respectively the shear modulus, the Poisson's ratio and the density of the 1018 steel. Properties were taken from [57].

The number of elements in the array (NE) determines the array aperture (length) which is proportional to the lateral resolution. Therefore high number of elements increases the resolution, at a cost of increasing scanning time, so a balance between image quality and experiment duration should be determined. In this study, it was decided to create and array of 50 elements, so the array has an active aperture of 0.5in.

In addition to the array aperture, the distance to the target also affects the image lateral resolution. The best resolution is achieved with a separation equal to the transducer natural focus (NF). As discussed in section 1.1.2, the NF is the point of maximum transverse relative intensity within the focal area. The NF position (N) is calculated with the formulation presented in section 1.1.2, but due to the presence of the wedge, the distance to the target (AP) is founded by subtracting the space inside the wedge (1.7in):

$$AP = N - 1.7in = \frac{D^2f}{4c} - 1.7in \quad (37)$$

$$AP = \frac{0.5in^2 \times 5MHz}{4 \times 2953m/s} - 1.7in \quad (38)$$

$$AP = 1.0in \quad (39)$$

Where D is the transducer diameter, f the transducer's center frequency, c is the SAW speed in 1018 steel, NF is the transducer's natural focus and AP the array position with respect to the bolt. Figure 32 illustrates a sketch of the final configuration.

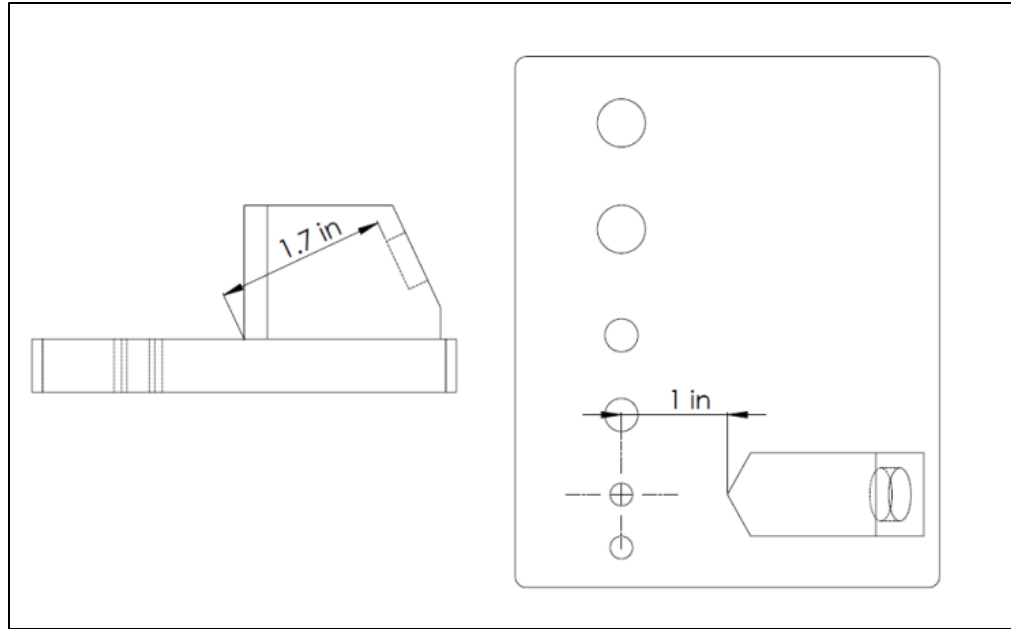


Figure 32. Sketch of transducer-wedge position with respect to the targeted hole.

Stretching the bolt increases the bolt tension and hence increasing the RAC between the bolt head and the steel plate. It discussed previously the RAC and the normal force are proportional [61]. The bolt tension is equivalent to the normal force in this application: The elongation of the bolt body creates a pulling force at the bolt head, but is also the deformation in the bolt body which creates the tension force. In this sense, the tension force pulls the bolt head against the plate in the same as the normal force would push it.

In this experiment the bolt tension is not directly controlled but the torque applied to the bolt is controlled. In chapter 1 it was explained that torque and tension are related by the bolt diameter and a friction factor which is a function of screw type and the materials in contact. From this perspective, for a particular bolt installed in a specific plate, the torque and tension are proportional in nature. As a result, the torque and RAC values are also proportional:

$$T \propto F_N \wedge RAC \propto F_N$$

Then

$$RAC \propto T \quad (41)$$

Where  $T$  is the torque applied to the bolt,  $F_N$  is the normal force and RAC is the real area of contact.

One can infer from this equation that the RAC can be adjusted by controlling the specific amount of torque applied to the bolt. In this first set of experiment conducted, three torque levels are applied: no torque, medium torque and maximum torque.

#### ***4.2.2 Experiment Configuration***

There are three key components in the experiment setup: precise position controlling system, SAW generation system and the bolted joint. The position control of the transducer-wedge attachment is achieved through a manual translator stage with resolution of 0.001in and maximum displacement span of 1in. The transducer and the wedge are adapted to the translator stage (Thorlabs PT3) by specially designed aluminum parts.

The electronic signals are generated and received by a pulse generator (Olympus 5072PR) and an oscilloscope (Tektronix TDS 2024B). A 5MHz piezoelectric transducer (PZT) with circular aperture of 1/2in is driven by the pulse generator. A crystal wedge is attached to the PZT for creating SAW in the steel plate. The configuration of the devices is presented in Table 4.

Table 4. Parameters employed in the experimental configuration of section 4.2.

Pulse generator Damping	50Ω	Transducer Frequency	5 MHz
Pulse generator PRF	200 Hz	Transducer Diameter	0.5 in
Amplification	45dB	Array Pitch (in)	0.01 in
Pulse generator LPF (1MHz)	ON	Number of Elements	50
Pulse Generator HPF (10MHz)	ON	Target Distance	2.7 in
SAW velocity	2590 m/s	Bolt Diameter	0.5in

The bolted joint employ in this test is formed by a 1018 steel plate and a ¼ in 20UNC bolt. Neither nut nor washer is used in this test. The bolt is tightened with help of the threaded holes present in the work bench (Figure 31). In Figure 33 dimension and characteristics of the machined holes are illustrated. It is important to notice that all the holes in the plate have a coarse thread. This characteristic facilitates the installation of the tested bolts. Additionally, no lubricant is used in the joint. The surface conditions of the threads are good enough to permit proper bolt tightening. The plate can be attached to the work bench by C-clamps when is so required. Additional information about the devices employed is presented in Appendix A.

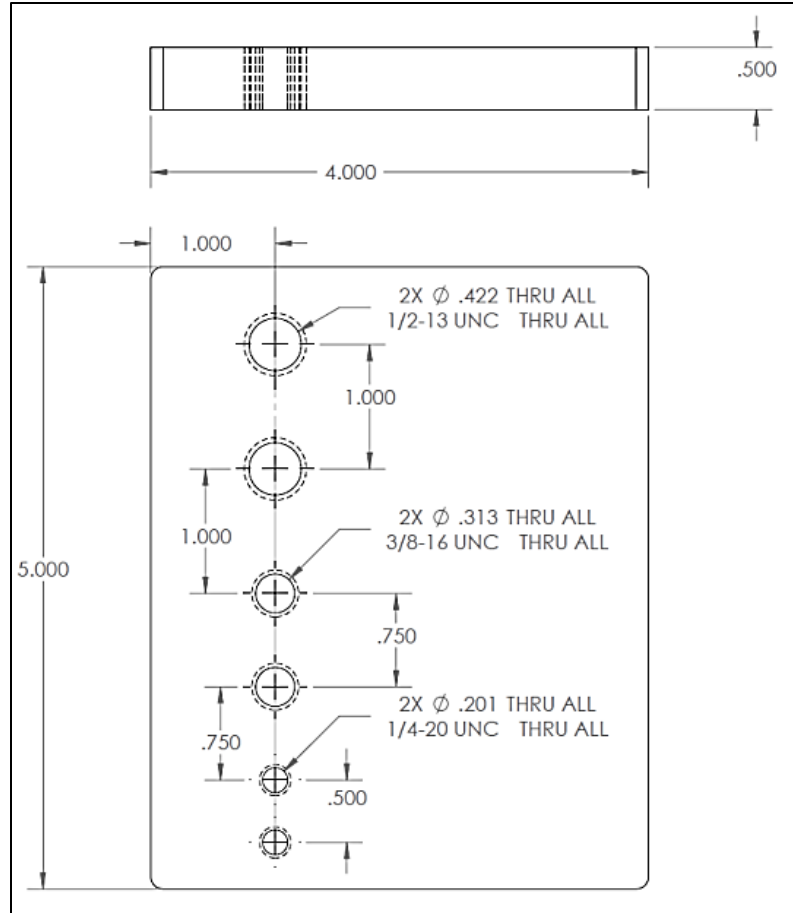


Figure 33. Drawing of the 1018 steel plate used for all SAW experiments in this research.

#### 4.2.2.1 Experimental Procedure

The procedure is creation of a synthetic phased array by the mechanical movement of a single transducer. All the signals should be averaged before acquiring to increase the signal to noise ratio of the system. The experimental procedure is as follows:

1. The steel plate should be locked with the help of C clamps. The rotation of the plate must be constrained during the tightening process.

2. The wedge-transducer assembly should be secured to the TS with help of the aluminum L and aluminum plate. The height of this assembly must permit the contact between the transducer base and the plate surface. Acoustic couplant must be applied prior any contact as the acoustic impedance mismatch between the transducer crystal and the steel may prevent the transmission of waves.
3. The TS is employed to position the wedge as is shown in Figure 32. It is very helpful to use the steel plate edges as reference. The movement span of the TS is only one inch, so the positioning process should take into account that the wedge needs to move 0.5in after initially positioned.
4. The oscilloscope and the pulse generator should be turned on. The signal gain must be set around a value in the range of 30's or 40's. The correct configuration of the oscilloscope allows the edge reflection to be observed. The highest peak should be at least half of the oscilloscope scale.
5. In order to start the recording process, the signal recording mode should be set to average; this helps to increase the signal to noise ratio of the system. After recording the signal at the initial point, the transducer should be moved 0.01in to the right; prior to recording the second response, the average function should be reset. This procedure is repeated until 50 data are collected.

6. After the first 50 data are collected, the bolt should be installed and tightened with a wrench until a medium torque value is achieved. This is the starting point for a new set of 50 data. Before the third data set is recorded the bolt should be tightened up again.

### ***4.3.3 Experimental Results***

The imaging reconstruction generates three images correspondent to the applied torque levels. Figure 34 illustrates the results as 15dB of dynamic range. The array is located at the left of the image. In the center of the images, the reflections from the bolt head are clearly distinguishable.

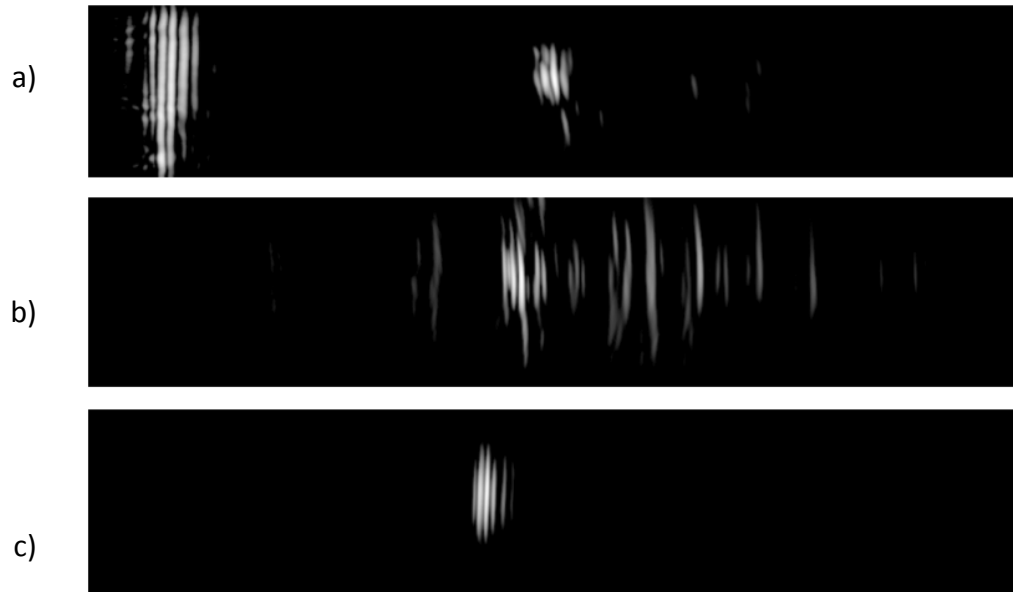


Figure 34. Generated images of the steel plate at 15dB of dynamic range. Applied torque a) none, b) medium and c) maximum.

The position of the bolt reflection has clearly an influence from the applied torque. As expected, at higher torque levels the reflections move gradually closer to the array (to the left), furthermore the image appears to be sharper in the extreme cases of maximum and minimum torque.

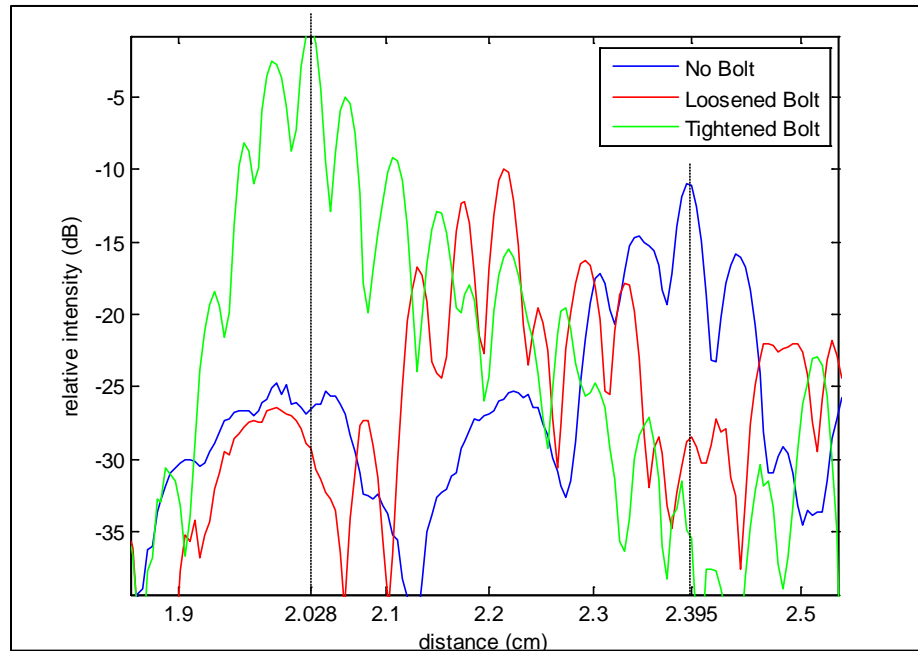


Figure 35. Averaged 1-D images at 6dB.

An averaged 1-D images are illustrated in Figure 35. The plot is a portion of the complete 6dB image averaged transversally. This figure allows easier calculation of the position of the main objects in the 2-D images. In Figure 35 the positions of the bolt head reflections are presented and compared. The position difference with respect to the no bolt case is:

$$\text{Tightened Bolt} = 2.395 - 2.028 = 0.367 \text{ cm}$$

$$\text{Loosened Bolt} = 2.395 - 2.2 = 0.195 \text{ cm}$$

### 4.3 Tension Evaluation of a 1/2in Stainless Steel Bolt

This experiment tests the proposed concept with a 1/2inch 13UNC stainless steel bolt. The larger bolt allows the application of higher tension levels, it also increases the geometric area of contact, and hence larger changes in the RAC are expected. Additionally this bolt size is more representative of a civil structure, which is the possible future application of the methodology.

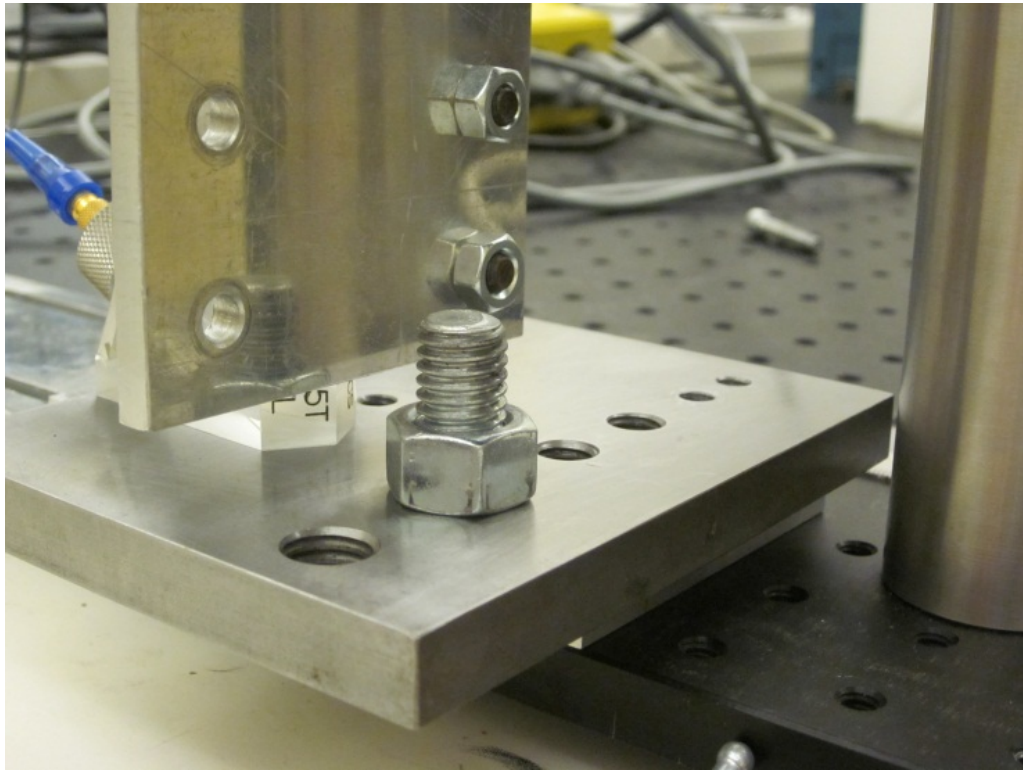


Figure 36. Photo of 1/2 inch stainless steel bolt tension evaluation.

### 4.3.1 Experiment Design

The parameters required in this experiment are array pitch, number of elements in the array, distance to the target and the torque applied. The array pitch (0.01in) is maintained because the same transducer is used in this study (transducer with 5MHz of central frequency and 1/2in of circular aperture). Additionally the target distance is also kept constant.

The array aperture is increased due to the target size. It is necessary to have a fixed boundary that works as framework to clearly establish the movement of the reflective boundary. The plate edge is used for this purpose. Then the array aperture is selected to be larger than the target. An aperture of 0.75in is designated and therefore 75 array elements are needed.

The methodology proposed by [21] is used to calculate the maximum applicable torque for the 1/2in UNC13 stainless steel bolt. It is assume a friction value of 0.2 as suggest by [21].

$$T = KA_t 0.85S_y d = 0.20 \times 9.154824 \times 10^{-5} m^2 \times 0.85 \times 35ksi \times 1/2in \quad (42)$$

$$T_{max} = 35.6Nm \quad (43)$$

Where K is the friction factor,  $A_t$  is the tensile stress area,  $S_y$  is the bolt yield strength,  $d$  is the bolt nominal diameter and  $T$  is the torque applied.

The analysis of the experiments in this thesis is performed using the changes of the parameters of interest: tension, torque and boundary position. Therefore the uncertainties in the tension applied to the bolt, which depends of the friction and may vary up to 50% [62], do not affect the result analysis. As explained in section 4.2.1 that RAC, tension and torque are proportional in nature, hence the proportionality coefficients, like the friction in the case of torque-tension, influence the value of the parameters but not the changes produced by them.

The maximum torque is higher than the supported by the torque wrench, so the maximum torque supported by the wrench is chosen. Additionally due to the high number of array elements, the torque states were decided to be three.

$$T_{max} = 29.03Nm \quad (44)$$

$$T_{increments} = \frac{T_{max}}{3} \approx 15.48Nm \quad (45)$$

#### ***4.3.2 Experiment Configuration***

The position controlling system, SAW generation system are the same as the ones discussed in the prior section. The translator stage (Thorlabs PT3), the pulse generator (Olympus 5072PR) and the oscilloscope (Tektronix TDS 2024B) are also employed in this experiment. The 1018 steel plate is also kept but the 1/2in threaded hole is used this time. The tested bolt is a 1/2in 13UNC stainless steel bolt. In this experiment the workbench cannot be used to tighten the bolt due to the size difference, hence a ½ inch stainless steel nut is employed for this purpose. It is not necessary to apply lubrication in this case neither. The configuration of all the devices is presented in Table 5.

Table 5. Parameters employed in the experimental configuration of section 4.3.

Pulse generator	50Ω	Number of Elements	75
Damping		Target Distance	2.7 in
Pulse generator PRF	200 Hz	Bolt Diameter	0.5in
Amplification	45dB	Bolt Yield Strength	35 ksi
Pulser LPF & HPF	ON	Friction Factor	0.20
SAW velocity	2590 m/s	Tensile Stress Area	9.154824x 10 <sup>-5</sup> m <sup>2</sup>
Transducer Frequency	5 MHz	Maximum Torque	29.03 Nm
Transducer Diameter	0.5 in	Torque Increments	15.48Nm
Array Pitch (in)	0.01 in		

#### 4.3.2.1 Experimental Procedure

1. The steel plate should be locked with help of C clamps. The rotation of the plate must be constrained during the tightening process.
2. The wedge-transducer assembly should be secured to the TS with help of the Aluminum L and aluminum plate. The height of this assembly must permit the contact between the transducer base and the plate surface. Acoustic couplant must be applied prior any contact as the acoustic impedance mismatch between the transducer crystal and the steel may prevent the transmission of waves.

- The TS is employed to position the wedge as is shown in Figure 37. It is very helpful to use the steel plate edges as reference. The movement span of the TS is only one inch, so the positioning process should take into account that the wedge needs to move 0.75in after initially positioned.

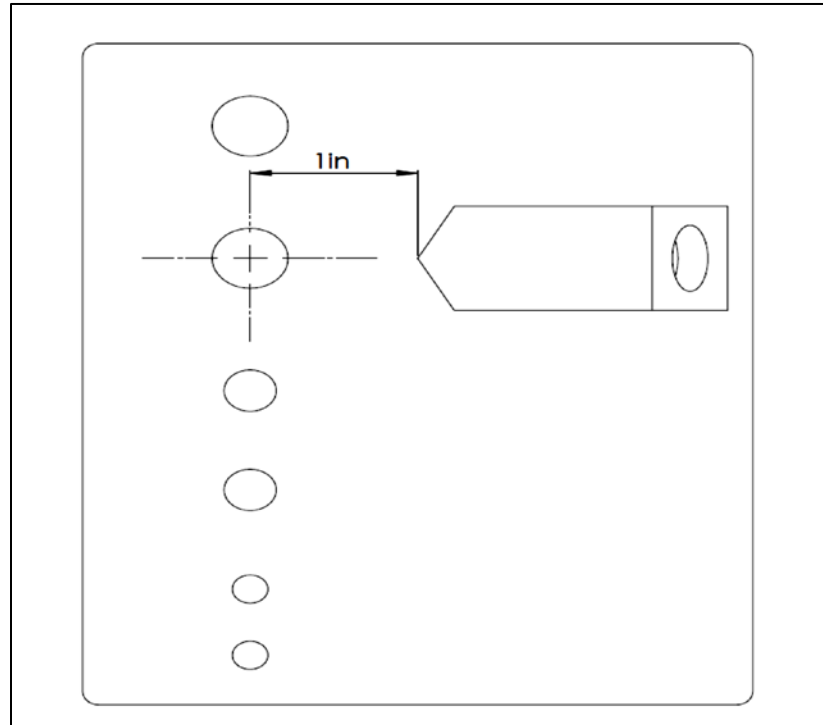


Figure 37. Schematic of wedge-transducer initial position.

- The oscilloscope and the pulse generator should be turned on. The signal gain must be set around a value in the range of 30's or 40's. The correct configuration of the oscilloscope allows the edge reflection to be observed. The highest peak should be at least half of the oscilloscope scale.
- In order to start the recording process, the signal should be set to average, this helps to increase the signal to noise ratio of the system. After recording the

signal at the initial point, the transducer should be moved 0.01in to the right; prior to recording the second response, the average function should be reset. This procedure is repeated until 75 data are collected.

6. After the first 75 data are collected the bolt should be tightened with the torque wrench until 15.48 Nm are reached. This is the starting point for a new set of 75 data. Following the torque should be increased up to the maximum value supported by the wrench (29.03Nm).

#### ***4.3.3 Experimental Results***

One image at every torque value is constructed. In Figure 38 the results are presented at 15dB of dynamic range. In the images the clear reflection from the hole and the nut can be observed, but the position variation in not clear.

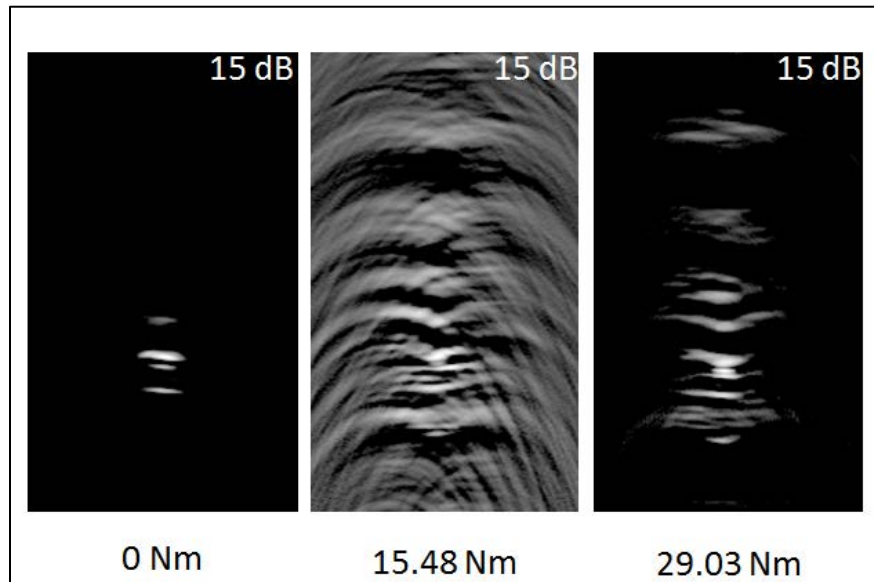


Figure 38. Generated images of the steel plate at 15dB of dynamic range.

Figure 39 illustrates the average signal intensity of the reflected waves. With this figure the change in the acoustic wall can be observed. The position change is 0.06cm which is very small compared with the nut diameter (1.88cm).

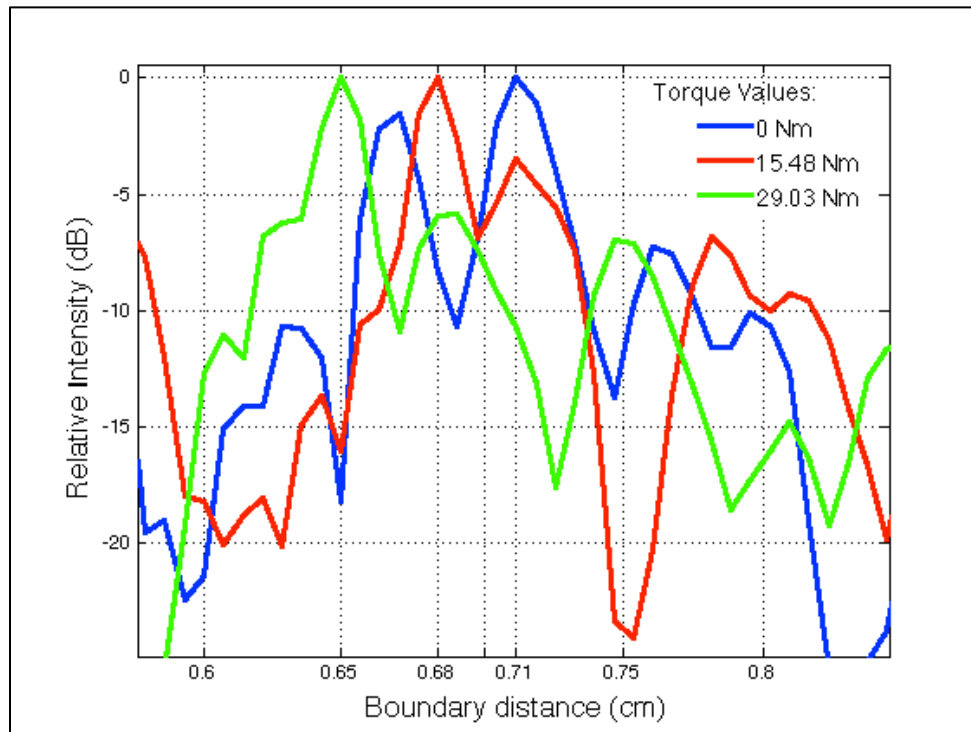


Figure 39. Averaged 1-D images at 6dB.

In Figure 40 a plot of the boundary position against the torque is presented. The parameters are inversely proportional as expected. The small change in the boundary position may be caused by lower force per unit area (pressure), but it is necessary to perform additional tests before constructively determining the cause of this behavior.

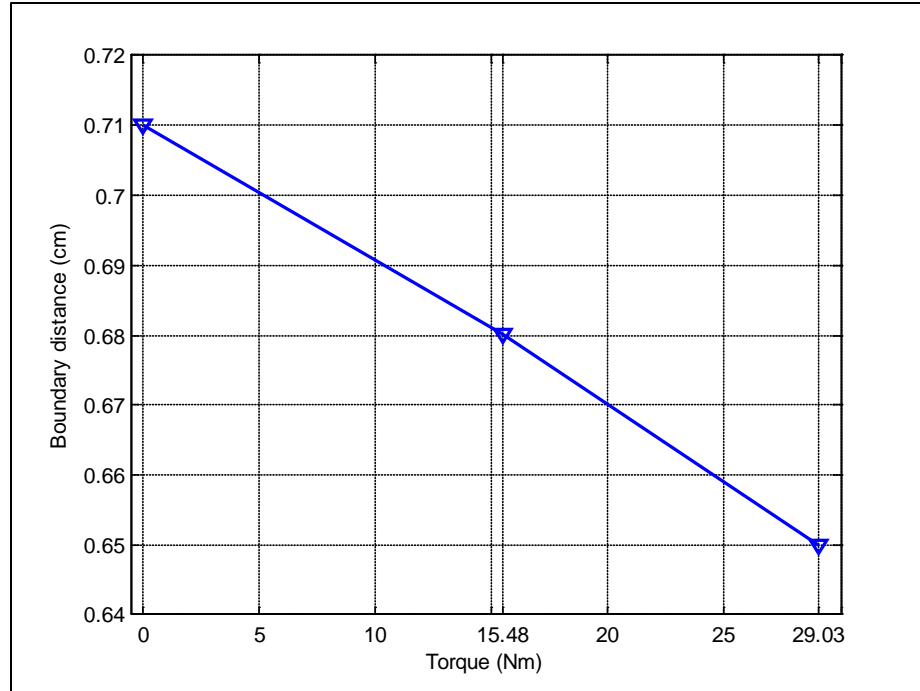


Figure 40. Plot of torque applied versus position of the acoustic wall.

#### 4.4 Tension Evaluation of a 1/4in Grade 8 Bolt

In this experiment higher tension levels are tested. In the set of experiment of section 4.2 the mechanical resistance of the stainless steel bolt prevents further increments of the torque levels therefore in this occasion a 1/4in grade 8 bolt is employed. Grade 8 bolts have yield strength almost 3 times higher than stainless steel bolts [57]. Additionally a stainless steel washer is fixed to the bolt in order to increase the expansion capability of the RAC (Figure 41).

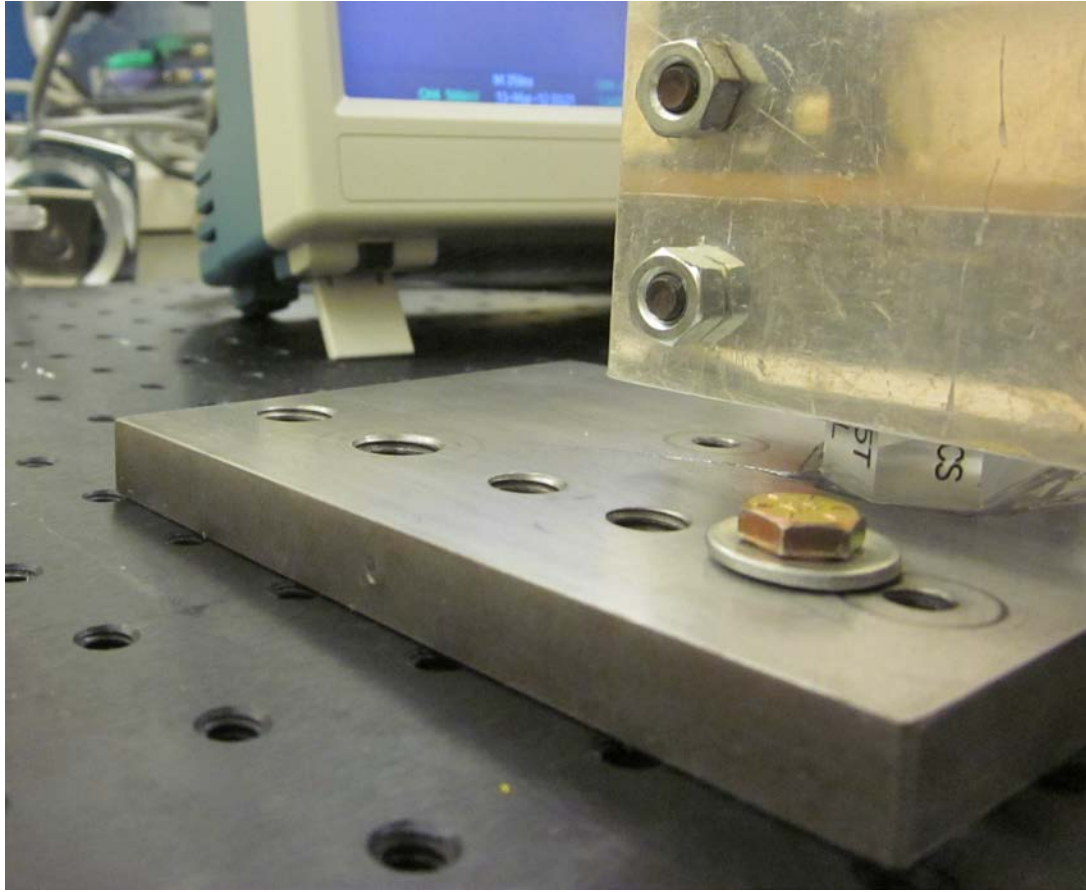


Figure 41. Photo of 1/4 inch grade 8 bolt tension evaluation.

#### ***4.4.1 Experiment Design***

This experiment holds the array parameters of the experiment in section 4.2: pitch of 0.01in and 50 array elements. In section 4.2.1 the procedure to calculate these factors is explained. On the other hand the torque applied to the fastener is in this occasion increased. The same methodology employed in section 4.3.1 is employed.

The diameter, tensile area and yield strength are modified for a 1/4in UNC20 grade 8 bolt. In addition, general purpose oil is used during the experiment to help in the tightening process, so a reduction in 10% in the friction factor is required to assure no bolt rupture. In order to create an accurate trend of the TOF with respect to torque

changes, the number states are increased to 5. The yield strength of a grade 8 bolt is around 130ksi [21], so the maximum torque and the increments applied are calculated as follows:

$$T = KA_t 0.85S_y d = 0.18 \times 20.516mm^2 \times 0.85 \times 130ksi \times 1/4in \quad (46)$$

$$T_{max} = 13.78Nm \quad (47)$$

$$T_{increments} = \frac{T_{max}}{4} \approx 3.61Nm \quad (48)$$

Where  $K$  is the friction factor,  $A_t$  is the tensile stress area,  $S_y$  is the bolt yield strength,  $d$  is the bolt nominal diameter and  $T$  is the torque applied.

#### ***4.4.2 Experiment Configuration***

The position controlling system and the SAW generation system are the same as the ones discussed in the prior section. The translator stage (Thorlabs PT3), the pulse generator (Olympus 5072PR) and the oscilloscope (Tektronix TDS 2024B) are also employed in this experiment. The 1018 steel plate is also maintained. The tested bolt is a 1/4 20UNC grade 8 bolt that is tightened using the work bench. As is illustrated in Figure 41, a 3/4 inch stainless steel washer is used. The rate in which the RAC grows may change for different materials hence keeping the same material surfaces in contact of the previous experiments permits a direct comparison of the results. The required configuration of all these devices is presented in Table 6.

Table 6. Parameters employed in the experimental configuration of section 4.4.

Pulse generator		Transducer Diameter	0.5 in
Damping	50Ω	Array Pitch (in)	0.01 in
Pulse generator PRF	200 Hz	Number of Elements	50
Amplification	45dB	Target Distance	2.7 in
Pulse generator LPF (1MHz)	ON	Bolt Diameter	0.25 in
Pulse Generator HPF (10MHz)	ON	Bolt Yield Strength	130 ksi
SAW velocity	2590 m/s	Friction Factor	0.18
Transducer Frequency	5 MHz	Tensile Stress Area	20.516 mm <sup>2</sup>
		Maximum Torque	17.86 Nm
		Torque Increments	3.61Nm

#### 4.4.2.1 Experimental Procedure

1. The steel plate should be locked with help of C clamps. The rotation of the plate must be constrained during the tightening process.
2. The wedge-transducer assembly should be secured to the TS with help of the Aluminum L and aluminum plate. The height of this assembly must permit the contact between the transducer base and the plate surface. Acoustic couplant must be applied prior any contact as the acoustic impedance mismatch between the transducer crystal and the steel may prevent the transmission of waves.

3. The TS is employed to position the wedge as is shown in Figure 42 It is very helpful to use the steel plate edges as reference. The movement span of the TS is only one inch, so the positioning process should take into account that the wedge needs to move 0.5in after initially positioned.

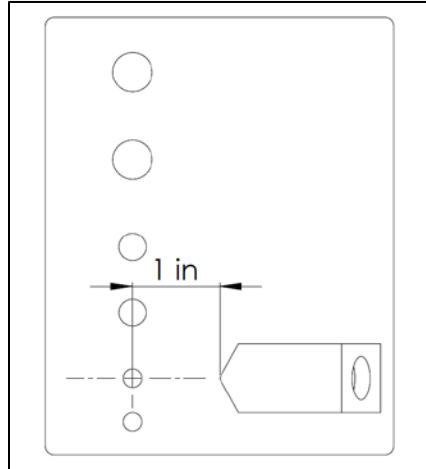


Figure 42. Schematic of the wedge initial position.

4. The oscilloscope and the pulse generator should be turned on. The signal gain must be set around a value in the range of 30's or 40's. The correct configuration of the oscilloscope allows the edge reflection to be observed. The highest peak should be at least half of the oscilloscope scale.
5. In order to start the recording process, the signal should be set to average, this helps to increase the signal to noise ratio of the system. After recording the signal at the initial point, the transducer should be moved 0.01in to the right; prior to recording the second response, the average function should be reset. This procedure is repeated until 50 data are collected.

6. After the first 50 data are collected the bolt should be tightened with the torque wrench until 3.61Nm are reached. This is the starting point for a new set of 50 data. The torque should be increased in intervals of 3.61Nm up to the maximum decided value is achieved (17.17Nm). Five sets of 50 data should be saved before the experiment is finished.

#### 4.4.3 Experimental Results

The results are obtained for six different torque levels. As expected the increments of 3.61Nm allow observing a clear trend in the reflection position, at higher torque values the boundary is closer to the array.

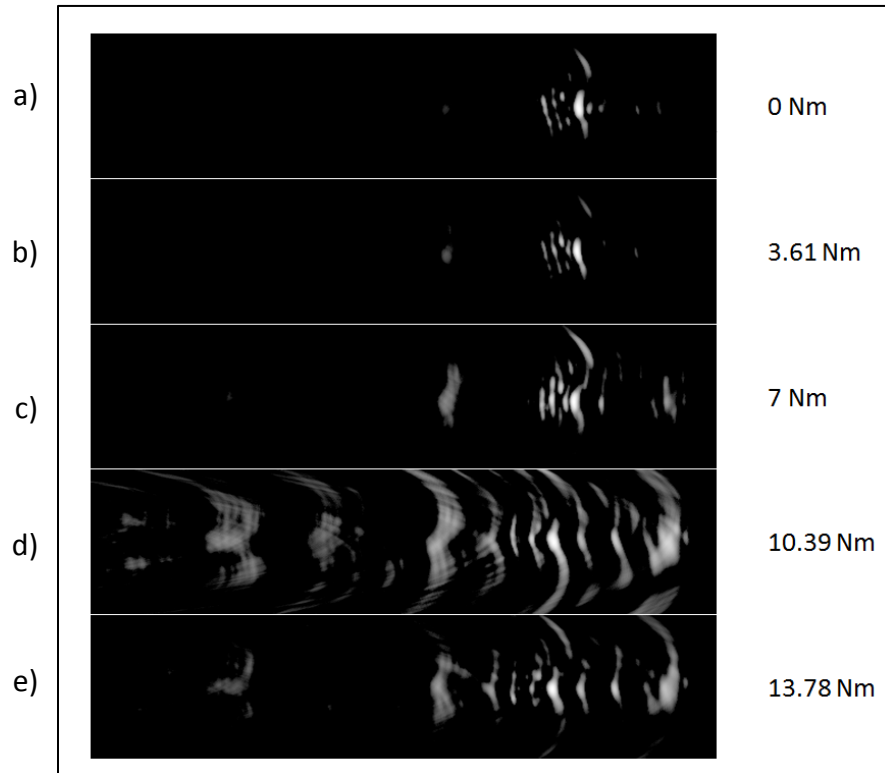


Figure 43. Images generated at 15dB with the SAW reflections from a 1/4in bolt with a stainless steel washer. Images for six different torque values were generated.

In Figure 43 the six reconstructed images are presented. In the case of no torque a clear reflection from the plate hole is observed. The case with torque of 3.61Nm also presents a small movement of the reflective boundary to the left side of the image. The following cases resulted in images with more noise but with the same trend: the point of higher reflection has a little delay with respect to the previous case and therefore to reflection in the image is shown slightly to the left side.

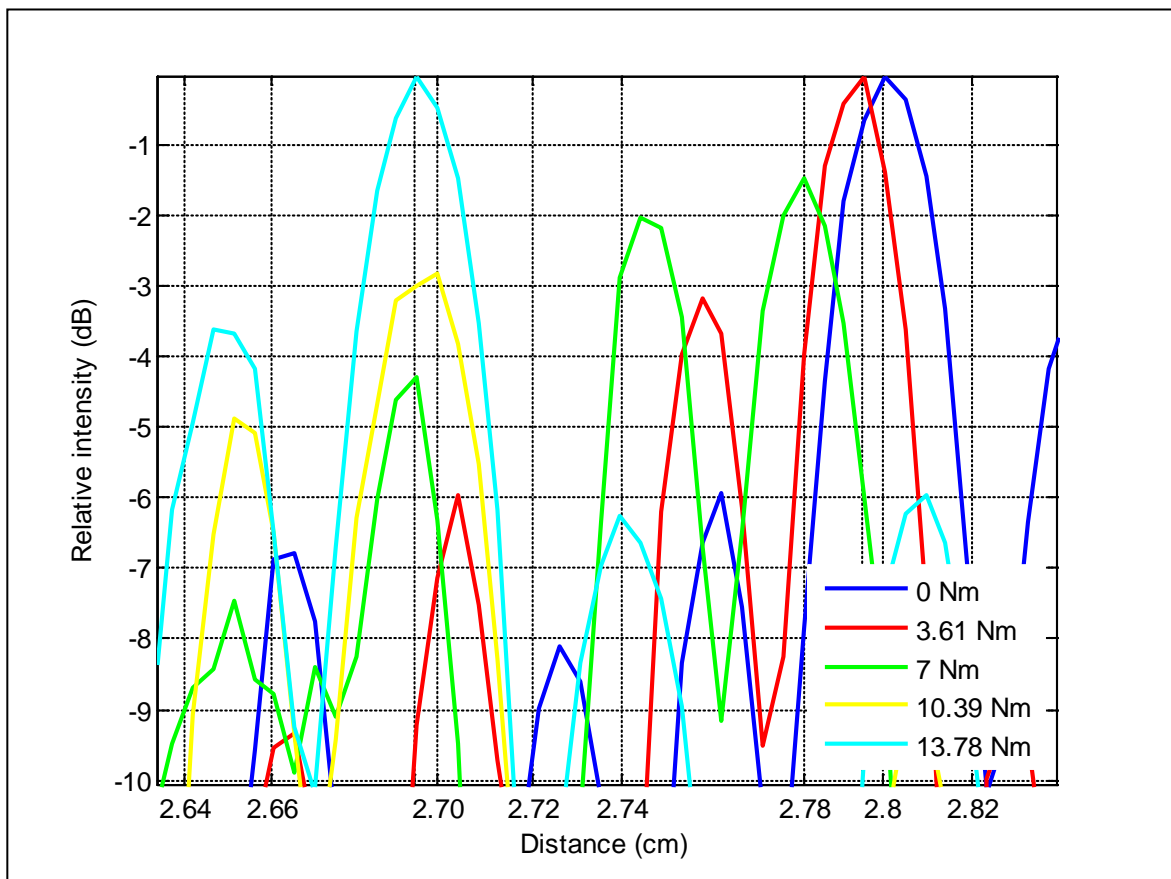


Figure 44. Averaged 1-D images at 6dB.

The change in the position of the main reflection is exposed clearly in Figure 44. The maximum points of maximum average signal intensity are plotted against its position in the images. It can be easily observed that the maximum intensity point of the blue signal (0 Nm) is separated from the peak of the light blue signal (13.78 Nm) approximately by 0.1cm. The remaining signal peaks are located between these extreme values.

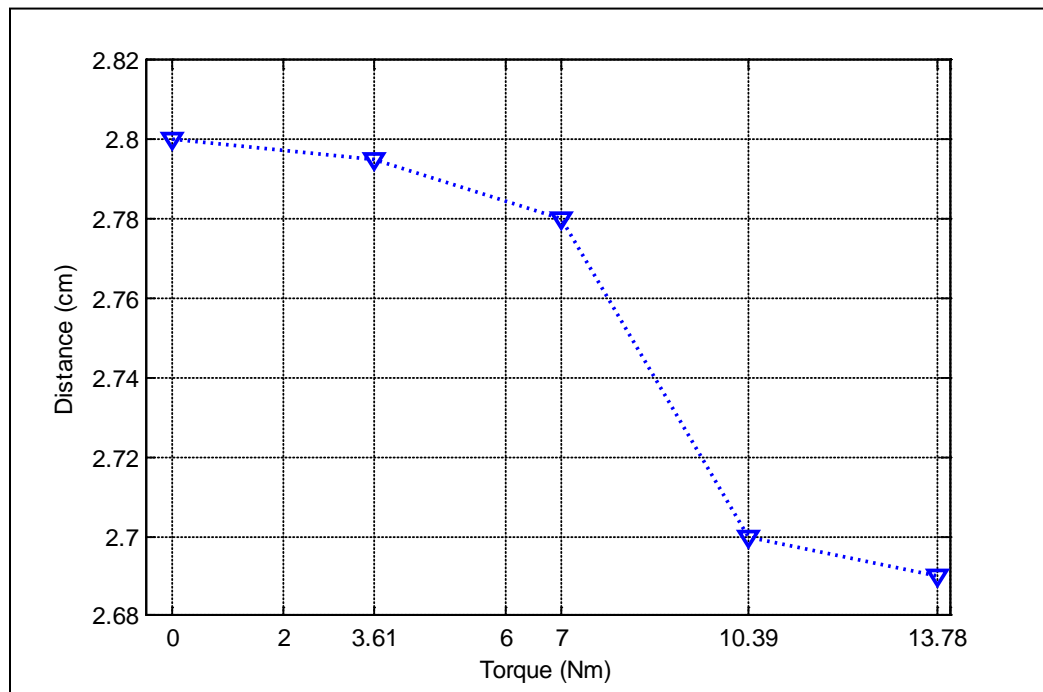


Figure 45. Graph of the torque applied versus the position of the acoustic wall.

The Figure 45 illustrates the change in distance product of torque variation. A reduction of 0.11cm in the boundary separation is founded as the torque is increased from 0 to 13.78 Nm. The position changes do not correspond linearly to the torque increments, as can be observed in Figure 45. This behavior can be explained by the fact that the RAC is not directly measured, only the size of the characteristic length may be estimated with the image. Then the boundary distance and the torque are not expected to be linear.

Another important characteristic of the plot is the apparent RAC saturation taking place at 10.39 Nm. The saturation phenomenon is explained in detail section 4.1. Apparently, the maximum RAC is achieved at a boundary position of around 2.7cm, but the washer edge is located at 3.335cm (The washer radius is 0.635cm). This behavior can be explained by the bending suffered by the washer, which influences the growth of the RAC.

#### ***4.4.4 Error Estimation***

##### *4.4.4.1 Signal to Noise Ratio of the System*

In order to analyze the error associated with the generated images, it is necessary to measure the signal to noise ratio (SNR) of the received signals(a-scans). In

Figure 46 the SNRs of the signals reflected by the bolt are presented. The graph illustrates the SNR levels for the 50 signals correspondent to every position of the transducer. As expected the SNR increase in the center signals due to the reflection from the washer (or the hole). It can also be noticed that the average SNR decreases as the torque level is increased, which means that the quality of the images produced at the higher torque levels is lower than in the lower torque states. Lower image quality lead to unacuarate estimation and greater error. The minimum dynamic range that can be applied to the images is determined by the averaged SNR.

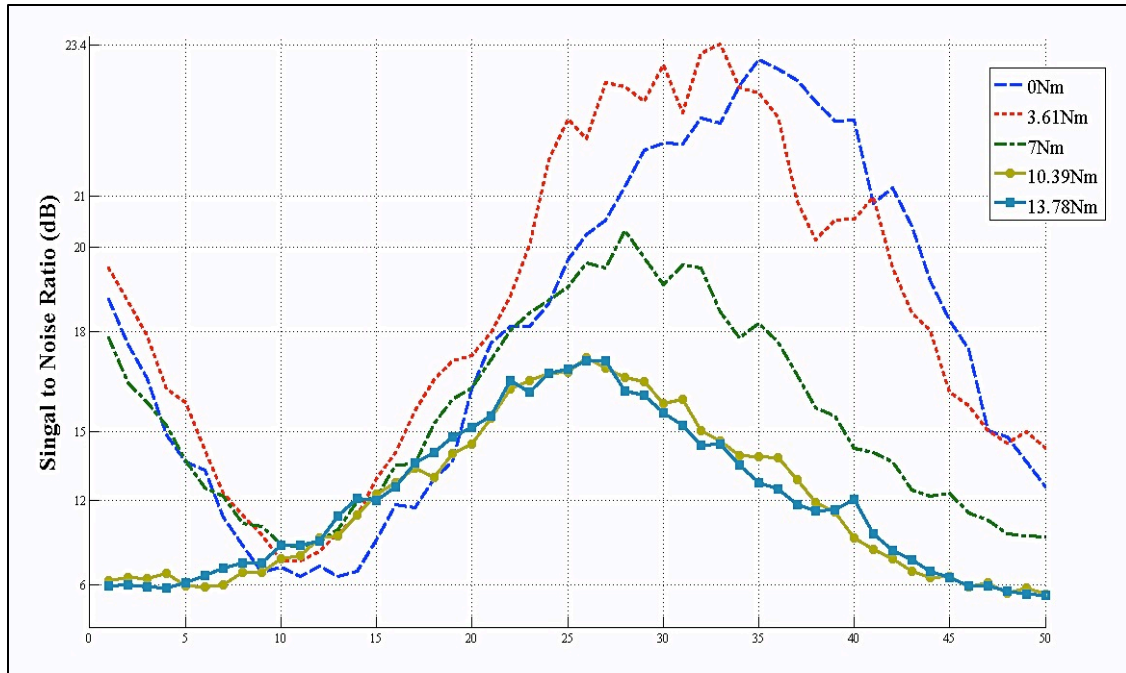


Figure 46. Signal to noise ratio of the bolt reflections based in original signals.

The reflective boundary position is calculated using the 1-D averaged plot based in the location of the signal peak. Consequently the peak SNR of Figure 47 at every torque level corresponds to peaks in Figure 44. The minimum peak SNR of the system is founded at 13.78Nm and it is equal to around 17dB, as shown in Figure 46. Although this is not a desired SNR level, it is good enough to differentiate the signal from the ambient noise.

The reduction of the SNR of the system around the bolt reflections may be attributed to some attenuation due to the bolt interference. Hence the SNR of the plate edge is studied and compared with the previous calculation. In Figure 47 the results are presented. As expected the maximum SNR are presented in the signals of the array sides, while the minimum SNR are in the center, exactly opposite to the previous case.

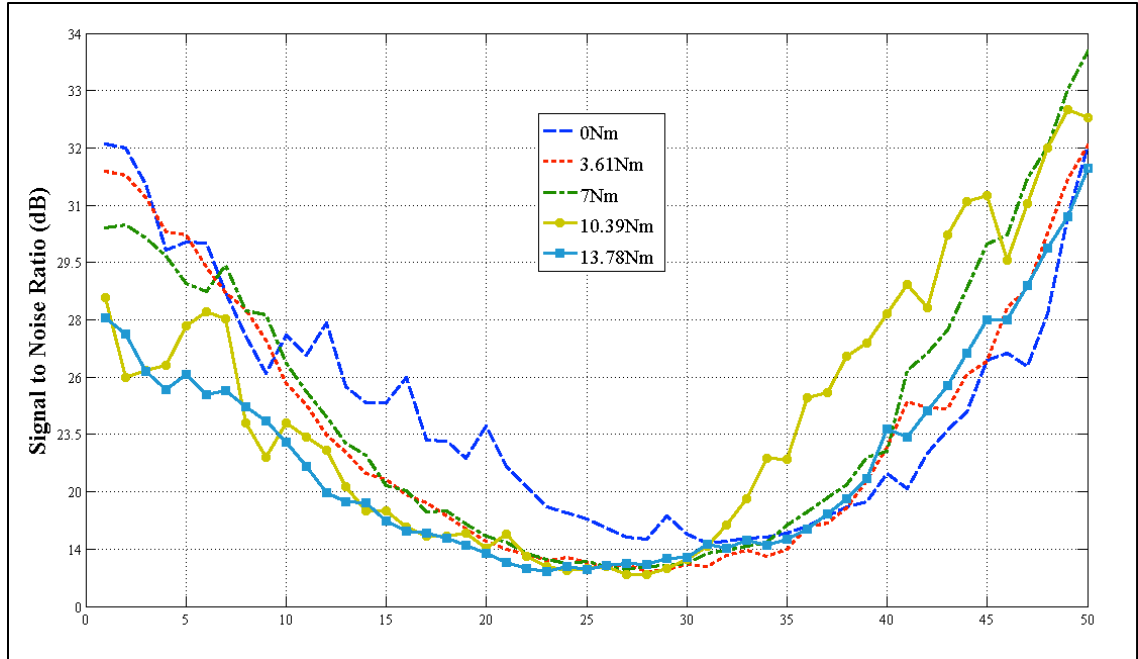


Figure 47. Signal to noise ratio of the plate edge reflections based in original signals

In the case of the plate edge, the behavior of the SNR peaks is not as clear as in the case of the bolt reflections. With the intention of comparing them, a graph of the averaged SNR for both cases is presented in Figure 48. Even though the signal loss tends to reduce the SNR for both cases as the torque is increased, there is an abrupt SNR drop in the bolt case. It is especially notorious when the torque is increased from 3.61Nm to 10.39Nm and the SNR decrease from 18dB to 12dB.

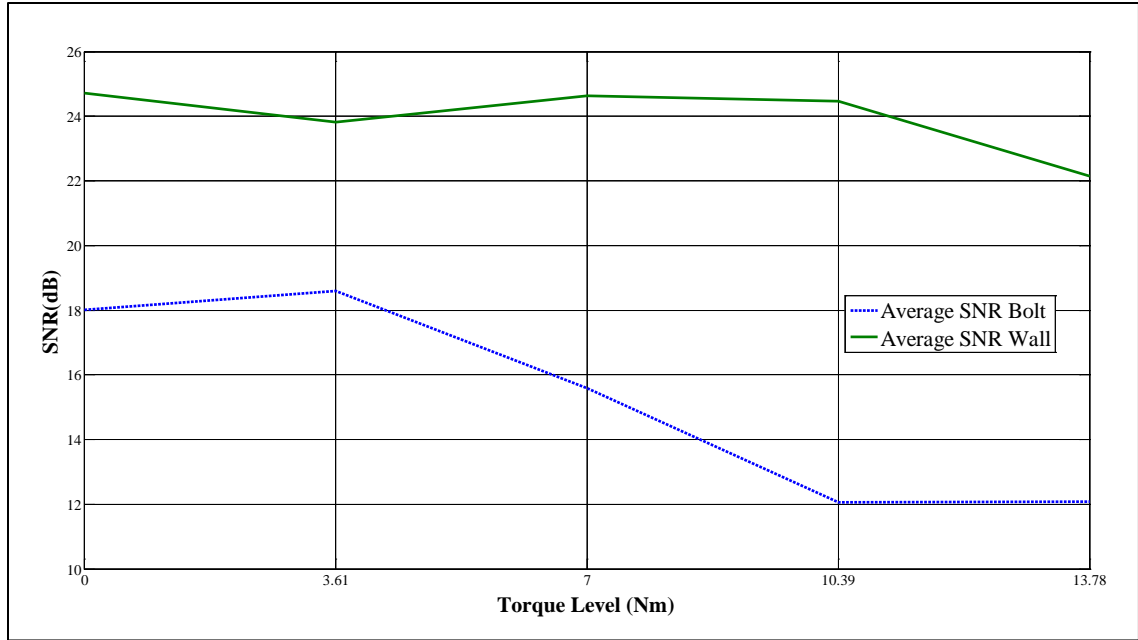


Figure 48. Averaged signal to noise ratio of the bolt and plate edge reflections based in original signals.

This analysis permits to identify the existence of error sources that generate signal losses, which finally reduce the SNR of the system. For instance, the acoustic couplant can be inducing signal loss as the experiment is performed. The necessity to move the transducer with the couplant may be causing that traces of gel interfere with the wave propagation. Additionally the movement in the set up caused by the tightening process may cause signal reduction.

As it was previously mentioned, there is more SNR reduction in the bolt surroundings than in the plate edge when the torque is increased. This phenomenon is caused either by sources of signal loss that only act in around the bolt or by signal attenuation due to the increased tension. Additional experimentation should be performed in order to clarify this behavior.

#### 4.4.4.2 Axial Resolution of the System

The axial resolution of the system permits to establish the accuracy of the system to estimate the movement of the reflective boundary. In section 2.2.4.3 the axial resolution was defined in equation 21. The frequency response and temporal pulse length of the system are founded with a network analyzer. The resulted axial resolution of the system is:

$$\Delta l = C \frac{t_p}{2} = 2593m/s \frac{5.55 \times 10^{-7}s}{2} = 0.072cm \quad (49)$$

The axial resolution is close to half of the total change in the boundary position (0.1cm), which means that the imaging system employed has the capability to measure the boundary position changes with enough accuracy. Although the axial resolution is sufficient, a system with smaller axial resolution can achieve more accurate results that permit better analysis of the tension-boundary position relation.

#### 4.4.4.3 Conclusions

The imaging system employed has the correct SNR and enough axial resolution for the investigation of RAC changes due to bolt tension in a ¼ inch bolt. A minimum SNR peak of 17 dB is founded at the maximum torque level, while a boundary movement of 0.1cm is measured with an axial resolution of 0.07cm. Both cases shows that the accuracy of the system is enough but not ideal for the analysis. In order to increase the precision of the system higher frequency and higher damped transducers can be employed. Additionally a phased array can increase considerably the SNR and it may limit the interferences of acoustic couplant caused by the mechanical movement of the transducer.

## **CHAPTER 5: CONCLUSIONS AND FUTURE WORK**

### **5.1 Conclusions**

In this thesis a novel methodology for measuring bolt tension based in surface acoustic waves (SAWs) is presented. A linear transducer array is employed for creating a variable acoustic beam. The methodology has potential for local or remote inspection of bolted joints. Additionally the direction variability of the acoustic beam enables monitoring of several bolted joints simultaneously.

The tension is estimated using the reflection of SAWs created by the bolt head interference. Increments in the bolt tension rise the points of interaction between the waves the bolt head (real area of contact) and therefore the position of reflective boundaries. The variations are estimated using the “conventional linear synthetic array” imaging technique. A singular transducer is actuated from predefined positions in order to produce an array of signals that are subsequently arranged and added to construct an acoustic image.

Three sets of experiments are presented in this research for validating the proposed concept: tension estimation of a ¼” stainless steel bolt, a ½” stainless steel bolt and ¼” grade 8 bolt. The tension is not directly measured nor applied to the bolt; instead controlled torque is used to generate the changes in the real area of contact. The torque and bolt tension produce equivalent effects in the real area of contact. Three figures summarize the experimental results: 2-D image of the reflective objects in the scanned surface, 1-D averaged plot of the images and plot of the torque applied versus position of the reflective boundary.

The 2-D image is a representation of the signals received by the transducer. The lighter colors represent reflection with higher intensity while darker with lower intensity. The images allow visualization of the position where the highest reflections take place. In the experiments, the reconstructed images illustrate a clear trend in the position of the reflective boundary when the applied torque is changed. In all cases the torque increments increase the real area of contact and therefore the position of the reflective boundary. As expected, the real area of contact grew from the bolt head center to the perimeter, which causes an effect of apparent movement of the boundary. The SAWs reflections only interact with the outer boundary of the real area of contact and as it grows, the position in which the interaction takes place moves towards the array location.

The 1-D average plot is a simplification of the 2-D image. Taking the average of lateral dimension of the 2-D image the graph is created. The 1-D plot allows establishing the exact position of the maximum intensity point of the 2-D image. The position of this

point is used to estimate the actual distance change of the reflective boundary. In all the experiment, this plot illustrates the same trend found in the 2-D image: The boundary moves towards the array as the torque is increased. The averaged 1-D plot also allows relating the torque level to the actual boundary position, which is a way to measure the bolt tension using this methodology.

The final outcome are plots of the boundary position versus the torque applied to the bolt. The graphs illustrate the actual change in position produced by the variation in the torque. The test performed to the 1/2in bolt presents an almost linear variation of the boundary position with the torque. In the 1/4in grade 8 bolt the results indicate two regions within the graph. The first region presents a non-linear behavior, while the second one is a saturation region. The saturation region (presented at the highest torque values) is characterized by slight changes in the boundary position due to torque increments.

The study proves the potential of the methodology for performing measurements of the applied tension. It is concluded that the actual shape of the real area of contact is not yet determined. While in the 1/2in bolt experiment, the relation torque-boundary position is linear, in the 1/2in grade 8 bolt it is not. The shape of the real area of contact is different for every experiment. The relation is expected to be a second grade polynomial. The area changes are estimated with variations of a “characteristic length” therefore a square value of the length should represent better the area changes. Finally, the saturation region founded in the last experiment shows the frontiers of the sensing capacity of the system.

The presented experiments are the first steps towards the development of bolt tension sensor based in surface acoustic waves. The results showed that the system has the potential to inspect tension in bolts of ½ and ¼ inches. Further experimentation is needed in order to better understand the behavior real area of contact and its interaction with the SAWs.

## **5.2 Future Work**

In order to increase the accuracy of the system, an array of transducers should be used for the imaging generation. With the array configuration, the image quality will be improved and the experimental time will be considerably reduced. Shorter experimental time will allow the experimentation with more tension states and different kind of materials. A real array of transducer will help to generate the images from different angles, which will provide more information about the real area of contact.

Although the tension and torque levels presented in a specific bolt are expected to be equivalent, the uncertainties associate with the friction may induce error in the tension estimation. In order to reduce this drawback, a direct tension estimation methodology can be employed. Load cells installed between the bolt head and the clamped plate can be used to measure the tension applied to the bolt, which then can be compared with the boundary position, just as it was done with the torque levels in this thesis.

The principal application of the methodology is the estimation of tension in threaded fasteners, but the real area of contact can also be studied with this approach. The generation of better quality images may provide important information of the interaction of SAWs with the objects in the surface through the real area of contact. The additional information can be useful for estimation of growth rates and shape of the real area of contact between surfaces.

## LIST OF REFERENCES

- [1] V. Giurgiutiu, "Elastic waves in solids and structures," in *Structural health monitoring with piezoelectric wafer active sensors*, Burlington, Elsevier Inc., 2008, pp. 129-182.
- [2] J. L. Rose, "Dispersion principles," in *Ultrasonic waves in solid media*, New York, Cambridge University Press, 1999, pp. 5-21.
- [3] T. L. Szabo, "Overview," in *Diagnostic ultrasound imaging*, Burlington, Elsevier Inc., 2004, pp. 29-45.
- [4] Iowa State University, "NDT Resource center," 2011. [Online]. Available: <http://www.ndt-ed.org/EducationResources/CommunityCollege/Ultrasonics>. [Accessed 02 2012].
- [5] J. L. Rose, "Unbounded isotropic and anisotropic media," in *Ultrasonic waves in solid media*, New York, Cambridge University Press, 1999, pp. 24-37.
- [6] H. Uberall, "Surface waves in acoustics," in *Physical acoustics principles and methods*, vol. X, New York, Academic Press, Inc., 1973, pp. 1-57.
- [7] J. L. Rose, "Surface and subsurface waves," in *Ultrasonic waves in solid media*, New York, Cambridge University Press, 1999, pp. 90-99.
- [8] J. D. N. Cheeke, "Rayleigh waves," in *Fundamentals and applications of ultrasonic waves*, Boca Raton, CRC, 2002, pp. 171-186.
- [9] T. L. Szabo, "Beamforming," in *Diagnostic ultrasound imaging*, Burlington, Elsevier Inc., 2004, pp. 137-168.
- [10] J. L. Rose, "Ultrasonic nondestructive testing principles, analysis and display technology," in *Ultrasonic Waves in solid media*, New York, Cambridge University Press, 1999, pp. 335-357.
- [11] K. L. Johnson, "Rough Surfaces," in *Contact mechanics*, New York, NY: Cambridge University Press, 1985, pp. 397-423.

- [12] H. Czichos, "Tribological processes," in *Tribology a systems approach to the science and technology of friction, lubrication and wear*, vol. I, New York, Elsevier Scientific Publishing Company, 1978, pp. 45-176.
- [13] A. C. Fischer-Cripps, "Introduction to contact mechanics," in *Surfaces forces, adhesion and friction*, New York, Springer-Verlag New York, Inc., 2000, pp. 179-188.
- [14] J. Bickford, "Materials," in *Design and behavior of bolted joints: non-gasketed joints*, Boca Raton, CRC Press, 2008, pp. 11-35.
- [15] D. P. Hess, "Vibration and shock-induced loosening," in *Handbook of bolts and bolted joints*, New York, Marcel Dekker, 1988, pp. 757-824.
- [16] J. Bickford, "Self-Loosening," in *Introduction to design and behavior of bolted joints: non-gasketed joints*, Boca Raton, CRC Press, 2008, pp. 303-325.
- [17] J. N. Goodier, "Loosening by vibration of threaded fastenings," *Mechanical Engineering*, no. 67, pp. 798-802, 1945.
- [18] J. A. Sauer, D. C. Lemmon and E. K. Lynn, "Bolts: how to prevent their loosening," *Machine design*, no. 22, pp. 133-139, 1950.
- [19] N. G. Pai and D. P. Hess, "Experimental study of loosening of threaded fasteners due to dynamic shear loads," *Journal of Sound and Vibration*, vol. 3, no. 253, pp. 585-602, 2002.
- [20] N. G. Pai and D. P. Hess, "Influence of fasteners placements and vibration-induced loosening," *Journal of Sound and Vibration*, no. 268, pp. 617-626, 2003.
- [21] R. G. Budynas and K. Nisbett, "Screw,fasteners, and the design of nonpermanent joints," in *Shigley's mechanical engineering desing*, 8th ed., Burlington, MA: The McGraw-Hill companies,Inc., 2006, pp. 396-425.
- [22] J. Bickford, "Basic concepts," in *Introduction to the design and behavior of bolted joints: non-gasketed joints*, Boca Raton, CRC Press, 2008, pp. 1-8.
- [23] J. Bickford, "Torque control of preload," in *Introduction to the design and behavior of bolted joints: non-gasketed joints*, Boca Raton, FL: CRC Press, 2008, pp. 137-169.
- [24] Y. H. Huang, L. Liu and Y. Y. Hung, "Real-time monitoring of clamping force of a bolted joint by use of automatic digital image correlation.," *Optics & Laser Techonology*, no. 41, pp. 408-414, 2009.

- [25] J. Bickford, "Torque and turn control," in *Introduction to the design and behavior of bolted joints: non-gasketed joints*, Boca Raton, FL: CRC Press, 2008, pp. 173-194.
- [26] J. Bickford, "Other ways to control Preload," in *Introduction to the design and behavior of bolted joints: non-gasketed joints*, Boca Raton, FL: CRC Press, 2008, pp. 197-216.
- [27] N. Tanner, J. Wait, C. Farrar and H. Sohn, "Structural health monitoring using modular wireless sensors," *Journal of Intelligent materials systems and structures*, vol. 14, 2003.
- [28] I. Milanese, P. Marzocca, J. M. Nichols, M. Seaver and S. T. Trickey, "Modeling and detection of joint loosening using output-only broad-band vibration data," *Structural Health Monitoring*, 24 November 2008.
- [29] R. Esmael, J. Briand and F. Taheri, "Computational simulation and experimental verification of new vibration-based structural health monitoring approach using piezoelectric sensors," *Structural Health Monitoring*, 12 September 2011.
- [30] F. Amerini and M. Meo, "Structural health monitoring of bolted joints using linear and nonlinear acoustic/ultrasound methods," *Structural Health Monitoring*, pp. 1-14, 31 January 2011.
- [31] N. Kim and M. Hong, "Measurement of axial stress using mode-converted ultrasound," *NDT&E International*, no. 42, pp. 164-169, 2009.
- [32] D. Mascarenas, G. Park, K. Farinholt, M. Todd and C. Farrar, "A low-powered wireless sensing device for remote inspection of bolted joints," in *Proceedings of the Institution of Mechanical Engineers*, Los Alamos, 2008.
- [33] V. Giurgiutiu, "Introduction to structural health monitoring," in *Structural health monitoring with piezoelectric wafer active sensors*, Burlington, Elsevier Inc., 2008, pp. 1-10.
- [34] K. R. Mobley, "Vibration monitoring and analysis," in *An introduction to predictive maintenance*, Woburn, Elsevier Science, 2002, pp. 114-171.
- [35] X. Zhu, P. Rizzo, A. Marzani and J. Bruck, "Ultrasonic guided waves for nondestructive evaluation/structural health monitoring of trusses," *Measurement science and technology*, no. 21, pp. 1-12, 2010.
- [36] J.-R. Lee, J. Takatsubo, N. Toyama and D.-H. Kang, "Health monitoring of complex curved structures using an ultrasonic wavefield propagation imaging system," *Measurement science and technology*, no. 18, pp. 1-10, 2007.

- [37] G. Park and D. J. Inman, "Structural health monitoring using piezoelectric impedance measurements," *Philosophical Transaction of the Royal Society*, no. 365, pp. 373-392, 2007.
- [38] P. Seunghee, L. Jong-Jae, Y. Chung-Bang and D. J. Inman, "Electro-mechanical impedance-based wireless structural health monitoring using PCA-data compression and k-means clustering algorithms," *Journal of Intelligent Materials Systems and Structures*, vol. 19, pp. 509-520, 2008.
- [39] V. Giurgiutiu, "High-frequency vibration SHM with PWAS modal sensors-the electromechanical impedance method," in *Structural health monitoring with piezoelectric wafer active sensors*, Burlington, Elsevier Inc., 2008, pp. 363-433.
- [40] S. Bhalla and C. K. Soh, "Structural impedance-based damage diagnosis by piezo-transducer," *Journal of Earthquake Engineering*, no. 32, pp. 1897-1916, 2003.
- [41] C. Liang, F. P. Sun and C. A. Rogers, "Coupled electro-mechanical analysis of adaptative material systems-determination of the actuator power consumption and system energy," *Journal of Intelligent Material and Structures*, no. 5, pp. 12-20, 1994.
- [42] V. Giurgiutiu, "Wave propagation SHM with PWAS," in *Structural health monitoring with piezoelectric wafer active sensors*, Burlington, Elsevier Inc., 2008, pp. 435-501.
- [43] L. Quifeng, L. Yin, Z. Min, W. Qiong and D. Aimin, "Study on improving time-domain resolution on detecting concrete structures," in *International Conference on Measuring Technology and Mechatronics Automation*, Shanghai, 2011.
- [44] S. Lyer, S. K. Sinha, M. k. Pedrick and B. R. Tittman, "Evaluation of ultrasonic inspection and imaging systems for concrete pipes," *Automation in construction*, 2011.
- [45] J. Zhu and J. S. Popovics, "Imaging Concrete structures using air-coupled impact-echo," *Journal of engineering mechanics ASCE*, vol. 133, no. 3, 2007.
- [46] B. W. Drinkwater and P. D. Wilcox, "Ultrasonic arrays for non-destructive evaluation: a review," *NDT&E International*, no. 39, pp. 525-541, 2006.
- [47] V. Giurgiutiu, "In-situ phased arrays with piezoelectric wafer active sensors," in *Structural health monitoring with piezoelectric wafer active sensors*, Burlington, Elsevier Inc., 2008, pp. 503-587.
- [48] C. Tekes, "Ring Array Processing for Forward-Looking Intravascular and Intracardiac Ultrasonic Imaging," Isik University, Istanbul, Turkey, 2010.

- [49] T. L. Szabo, "Array beamforming," in *Diagnostic ultrasound imaging*, Burlington, Elsevier Inc., 2004, pp. 171-209.
- [50] A. Sisman, "Solid-state arrays and beamformers for side-looking intravascular ultrasonic imaging," Işık University, Istanbul, Turkey, 2010.
- [51] G. Gunarathne, "Real-time ultrasonic imaging and advancements in non-conventional methods," in *International Instrumentation and Measurement Technology Conference*, Vancouver, 2008.
- [52] M. Vogt, J. Opretzka and H. Ermet, "Synthetic aperture focusing technique for high-resolution imaging of surface structures with high-frequency ultrasound," in *International Ultrasonics Symposium Proceedings*, Rome, 2009.
- [53] M. Schickert, M. Krause and W. Muller, "Ultrasonic imaging of concrete elements using reconstruction by synthetic aperture technique," *Materials in Civil Engineering*, vol. 15, no. 3, 2003.
- [54] E. G. Bazulin, "Obtaining flaw images that take the effect of multiple ultrasonic pulse reflections from the boundaries of a test object into account," *Russian Journal of Nondestructive Testing*, vol. 46, no. 10, pp. 735-753, 2010.
- [55] M. Spies and H. Rieder, "Synthetic aperture focusing of ultrasonic inspection data to enhance the probability of detection of defects in strongly attenuating materials," *NDT&E International*, no. 43, pp. 425-431, 2010.
- [56] L. Qiufeng, J. Xinhong, Z. Min, S. Lihua and S. Zhixue, "Simulation on improving resolution of SAFT," in *International Conference on Measuring Technology and Mechatronics Automation*, Zhangjiajie, China, 2009.
- [57] Automation Creations, "Matweb," [Online]. Available: <http://www.matweb.com/search/DataSheet.aspx?MatGUID=3a9cc570fbb24d119f08db22a53e2421&ckck=1>. [Accessed 02 2012].
- [58] T. L. Szabo, "Attenuation," in *Diagnostic Ultrasound Imaging: Inside out*, Burlington, MA: Elsevier Inc., 2004, pp. 71-95.
- [59] A. Mahmoud, H. Ammar, O. Mukdadi, I. Ray, F. Imani, A. Chen and J. Davalos, "Non-destructive ultrasonic evaluation of CFRO-concrete specimens subjected to accelerated aging conditions," *NDT&E International*, vol. 43, pp. 635-641, 2010.
- [60] V. Giurgiutiu, "Guided Waves," in *Structural health monitoring with piezoelectric wafer active sensors*, Burlington, MA: Elsevier Inc., 2008, pp. 185-238.

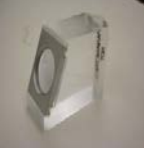
- [61] H. Czichos, "Tribology a systems approach to the science and technology of friction, lubrication and wear," vol. I, Elsevier Scientific Publishing Company, 1978, pp. 45-176.
- [62] Y. H. Huang, L. Liu and Y. Y. Hung, "Real-time monitoring of clamping force of a bolted joint by use of automatic digital image correlation.," *Optics & Laser Technology*, no. 41, pp. 408-414, 2009.
- [63] N. Portzgen, D. Gisolf and D. J. Verschuur, "Wave equation-based imaging of mode converted waves in ultrasonic NDI, with suppressed leakage from nonmode converted waves," *Transactions on Ultrasonics, Ferroelectrics and Frequency Control*, vol. 55, no. 8, pp. 1768-1780, 2008.
- [64] P. D. Wilcox, H. Caroline and B. W. Drinkwater, "Advanced reflector characterization with ultrasonic phased arrays in NDE applications," *Transactions on Ultrasonics, Ferroelectrics and Frequency Control*, vol. 54, no. 8, pp. 1541-1550, 2007.
- [65] Y. Pio-Liang and L. Pei-Ling, "Imaging of internal cracks in concrete structures using surface rendering technique," *NDT&E International*, vol. 42, pp. 181-187, 2009.
- [66] C. Holmes, B. W. Drinkwater and P. D. Wilcox, "Advanced post-processing for scanned ultrasonic arrays: application to defect detection and classification in non-destructive evaluation," *Ultrasonics*, vol. 48, pp. 636-642, 2008.
- [67] J. Zhang, B. W. Drinkwater, P. D. Wilcox and A. J. Hunter, "Defect detection using ultrasonic arrays: the multi-mode total focusing method," *NDT&E International*, vol. 43, pp. 123-133, 2010.
- [68] T. E. Michaels, J. E. Michaels and M. Ruzzene, "Frequency-wavenumber domain analysis of guided wavefields," *Ultrasonics*, vol. 51, pp. 452-466, 2011.
- [69] F. G. Mitri, J. F. Greenleaf and M. Fatemi, "Comparison of continuous-wave(CW) and tone-burst(TB) excitation modes in vibro-acoustography: application for non-destructive imaging of flaws," *Applied Acoustics*, vol. 70, pp. 333-336, 2009.
- [70] J. Yiang and I. C. Ume, "Thermomechanical reliability study of flip-chip solder bumps: using laser ultrasound technique and finite element methods," in *Electronic Components and Technology Conference*, 2008.
- [71] C. Silva, B. Rocha and A. Suleman, "A structural health monitoring approach based on a PZT network using a tuned wave propagation method," in *Structures, Structural Dynamics and Materials Conference*, Palm Springs, 2009.

- [72] V. Giurgiutiu, A. Zagrai and J. Bao, "Embedded active sensors for in-situ structural health monitoring of thin-wall structures," *Journal of Pressure Vessel Technology*, vol. 124, pp. 293-302, 2002.
- [73] D. G. Aggelis, T. Shiotani and M. Terazawa, "Assessment of construction joint effect in full-scale concrete beams by acoustic emission activity," *Journal of Engineering Mechanics*, pp. 906-912, 2010.
- [74] A. A. Shah and S. Hirose, "nonlinear ultrasonic investigation of concrete damaged under uniaxial compression step loading," *Journal of Materials in Civil Engineering*, pp. 476-484, 2010.
- [75] M. Meo, U. Polimeo and G. Zumpano, "Detecting damage in composite material using nonlinear elastic wave spectroscopy methods," *Applied Composite Materials*, vol. 15, pp. 115-126, 2008.
- [76] A. Ledeczi, P. Volgyesi, E. Barth, A. Nadas, A. Pedchenko, T. Hay and S. Jayaraman, "Self-sustaining wireless acoustic emission sensors system for bridge monitoring," Springer-Verlag, Berlin, 2011.
- [77] S. Chaki and G. Bourse, "Guided ultrasonic waves for non-destructive monitoring of the stress levels in prestressed steel strands," *Ultrasonics*, vol. 49, pp. 162-171, 2009.
- [78] J. Yu, P. Ziehl, B. Zarate and J. Caicedo, "Prediction of fatigue crack growth in steel bridge components using acoustic emission," *Journal of Constructional Steel Research*, no. 67, pp. 1254-1260, 2011.
- [79] L. Satyarnarayan, J. Chandrasekaran, B. Maxfield and K. Balasubramaniam, "Circumferential higher order guided wave modes for the detection and sizing of cracks and pinholes in pipe support regions," *NDT&E International*, no. 41, pp. 32-43, 2008.
- [80] I. Bartoli, S. Salamone, R. Phillips, F. Lanza di Scalea and C. S. Sikorsky, "Use of interwire ultrasonic leakage to quantify loss of prestress in multiwire tendons," *Journal of Engineering Mechanics*, pp. 324-333, 2011.

## APPENDICES

**Appendix A: Instrumentation Datasheet**

Table A1. Instrumentation datasheet

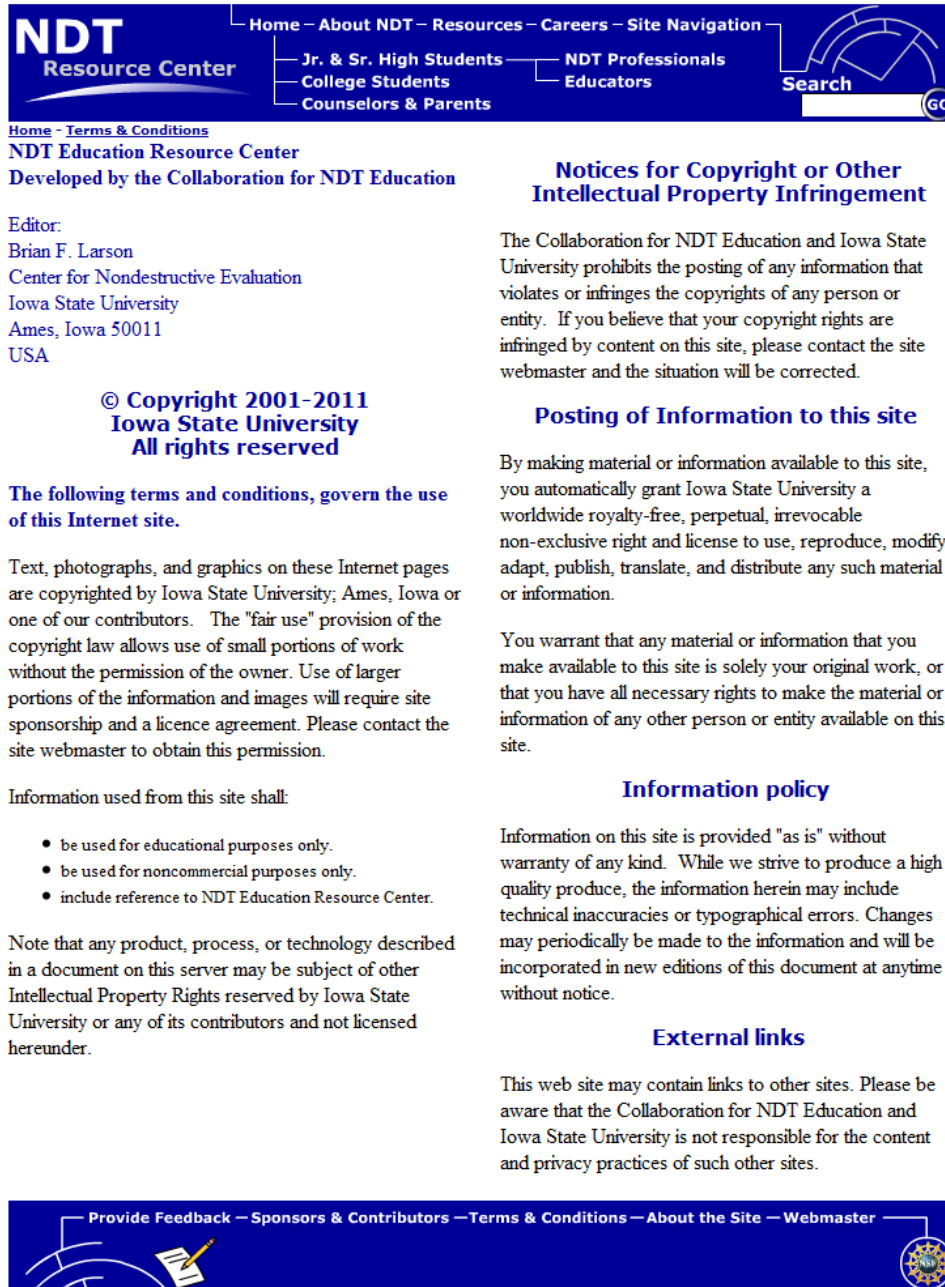
Device	Make & Model	Specifications	Photo
Linear Translation Stage	Thorlabs PT3	Travel : 1in	
		Resolution: 0.001in	
		XYZ Orientations	
Torque Wrench	Craftsman Microtork®	25-250 inch-pounds	
C-clamps	Husky	1 inch length	
Tested Plate	-	Material: 1018 Steel Plate	
		See Figure 33 for dimension details	
Crystal Wedge	Olympus ABWMI 5T	Incident angle: 90 degrees steel	
Transducer	Olympus C541	Central frequency: 5MHz	
		Diameter: 0.5in	

*Appendix A(continued)*

Table A1(continued).

Pulser/Receiver	Olympus 5072PR	Amplificator range :	
		50dB	
		High Pass Filter: 1MHz	
		Low Pass Filter: 10MHz	
Oscilloscope	Tektronix TDS 2024B	Analog Bandwidth:	
		20MHz	
		Sample Rate: 2GS/s	
		Analog Channels: 4	

## Appendix B: Third Party Permissions



**NDT Resource Center**

Home – About NDT – Resources – Careers – Site Navigation

Jr. & Sr. High Students  
College Students  
Counselors & Parents

NDT Professionals Educators

Search  GO

Home - Terms & Conditions  
NDT Education Resource Center  
Developed by the Collaboration for NDT Education

### Notices for Copyright or Other Intellectual Property Infringement

The Collaboration for NDT Education and Iowa State University prohibits the posting of any information that violates or infringes the copyrights of any person or entity. If you believe that your copyright rights are infringed by content on this site, please contact the site webmaster and the situation will be corrected.

### Posting of Information to this site

By making material or information available to this site, you automatically grant Iowa State University a worldwide royalty-free, perpetual, irrevocable non-exclusive right and license to use, reproduce, modify, adapt, publish, translate, and distribute any such material or information.

You warrant that any material or information that you make available to this site is solely your original work, or that you have all necessary rights to make the material or information of any other person or entity available on this site.

### Information policy

Information on this site is provided "as is" without warranty of any kind. While we strive to produce a high quality produce, the information herein may include technical inaccuracies or typographical errors. Changes may periodically be made to the information and will be incorporated in new editions of this document at anytime without notice.

### External links

This web site may contain links to other sites. Please be aware that the Collaboration for NDT Education and Iowa State University is not responsible for the content and privacy practices of such other sites.

Editor:  
Brian F. Larson  
Center for Nondestructive Evaluation  
Iowa State University  
Ames, Iowa 50011  
USA

© Copyright 2001–2011  
Iowa State University  
All rights reserved

The following terms and conditions, govern the use of this Internet site.

Text, photographs, and graphics on these Internet pages are copyrighted by Iowa State University; Ames, Iowa or one of our contributors. The "fair use" provision of the copyright law allows use of small portions of work without the permission of the owner. Use of larger portions of the information and images will require site sponsorship and a licence agreement. Please contact the site webmaster to obtain this permission.

Information used from this site shall:

- be used for educational purposes only.
- be used for noncommercial purposes only.
- include reference to NDT Education Resource Center.

Note that any product, process, or technology described in a document on this server may be subject of other Intellectual Property Rights reserved by Iowa State University or any of its contributors and not licensed hereunder.

Provide Feedback – Sponsors & Contributors – Terms & Conditions – About the Site – Webmaster

Figure B1. Publication permission NDT Resource Center.